2016

Investigation Of Wide Bandgap Semiconductor Devices For Radiation Detection Applications

Rahmi Orhon Pak
University of South Carolina

Recommended Citation

Pak, R. O.(2016). *Investigation Of Wide Bandgap Semiconductor Devices For Radiation Detection Applications.* (Doctoral dissertation). Retrieved from http://scholarcommons.sc.edu/etd/3930

INVESTIGATION OF WIDE BANDGAP SEMICONDUCTOR DEVICES FOR RADIATION DETECTION APPLICATIONS

by

Rahmi Orhon Pak

Bachelor of Science
University of South Carolina, 2013

Submitted in Partial Fulfillment of the Requirements

For the Degree of Doctor of Philosophy in

Electrical Engineering

College of Engineering and Computing

University of South Carolina

2016

Accepted by:

Krishna C. Mandal, Major Professor

Guoan Wang, Committee Member

Xiaofeng Wang, Committee Member

Fanglin (Frank) Chen, Committee Member

Cheryl L. Addy, Vice Provost and Dean of the Graduate School

DEDICATION

I would like to dedicate this work to my dear family and friends who have encouraged and supported me tirelessly in this endeavor. I am very thankful to all of you.

ACKNOWLEDGEMENTS

Above all, I am greatly thankful to my graduate advisor, Dr. Krishna C. Mandal, for his continued guidance and thorough support on this research. Within his group, I have developed my skillset from that of an university student to a practicing researcher - for which I am very grateful. I would also like to thank my committee members, Dr. Guoan Wang, Dr. Xiaofeng Wang, and Dr. Fanglin (Frank) Chen for taking the time to oversee my research and their support of my work.

I would also like to thank the following people for their contributions to the research performed in this work:

- Dr. Ramesh M. Krishna and Dr. Sandip Das, who assisted me heavily to design and build the electronics and software for the entirety of the crystal growth furnaces, zone-refiner, annealing furnaces, and the mechanical construction and design of the carbon coating systems.
- Dr. Peter Muzykov, who was instrumental for doing TSC spectroscopy on CZT and SiC. Dr. Muzykov also assisted in the EBIC characterization of CZT and SiC.
- The staff of the Electron Microscopy Center, for their assistance with SEM and EDAX studies.
- Dr. Sandeep K. Chaudhuri and Kelvin Zavalla, for their assistance in updating the digital correction scheme used to correct the CZT and SiC detector's pulse height spectra.

- Prof. Arnold Burger and Michael Groza from Fisk University for their assistance with fabrication of the a-Se and CZT detectors.
- Ms. Ashley Burt, Mr. David London, Ms. Nat Paterson and many other staffs of the Department of Electrical Engineering, for their technical and administrative assistance as I went through graduate school.
- My fellow lab members, Mr. Abhinav Mehta, Dr. M. A. Mannan, Mr. Cihan Oner, Mr. Towhid A. Chowdhury, and Mr. Haseeb Nazir, for their support and friendship throughout this process.

I would like to acknowledge the financial support from the Department of Energy (DOE), Nuclear Energy University Program (NEUP), Grant No. DE-AC07-051D14517; Los Alamos National Laboratory/DOE, Grant No. 143479; Advanced Support for Innovative Research Excellence –I (ASPIRE-I) of the University of South Carolina, Columbia, Grant Nos. 15530-E404 and 15530-A401.

Finally, I would like to thank my friends, family, and all those who have not been mentioned here. Without them this work would have been impossible.

ABSTRACT

Radioactive materials, as they decay, generate different high-frequency electromagnetic radiation such as alpha particles, beta particles, x-rays, gamma-rays, and neutrons. Nuclear detectors could stop these high-energy ionizing radiations, collect and transport the charges generated to an external circuit, and produce an electrical signal which is amplified by readout electronics to measure the energy of nuclear interaction. Thus, nuclear detectors are important tools for accounting of radioactive materials and have widespread applications in nuclear power plants, nuclear waste management, in national security, in medical imaging such as x-ray mammography, digital chest radiography, CT scan, and in high energy astronomy for NASA space exploration.

In this dissertation three different types of wide bandgap (WBG) radiation detectors were studied: (1) amorphous selenium (a-Se), (2) cadmium zinc telluride (CZT), and (3) silicon carbide (SiC). All three semiconductors have attractive electrical properties such as wide bandgap (≥ 1.5 eV) facilitating room temperature operation, high resistivity ($\geq 10^{10}$ Ω-cm) contributing to low thermal noise for high-resolution, and high charge carrier mobility-lifetime product offering high charge collection efficiency.

However, these semiconductors have distinct characteristics that set them apart from one another. For example, high Z (atomic numbers of constituent elements, Cd=48, Zn=30, Te=52) and high density of CZT offering high stopping power to absorb high energy x- and gamma-rays so CZT could be used for x- and gamma ray spectrometers at

room temperature. On the other hand, SiC has low Z value (Si = 14, C = 6) appropriate for detection of alpha particles and low energy x-rays and gamma rays (<60 keV) regime. Furthermore, high bandgap energy (~3.27 eV at 300 K) of 4H-SiC allows detector operation well above room temperature (~773 K) as required for nuclear fuel processing environment in nuclear power plants. Amorphous Se alloy with enriched boron (^{10}B) has high thermal neutron cross-section (3840 barns, 10^{-24} cm^2) due to boron and high radiation tolerance due to its amorphous structure, making it a favorable candidate for solid-state thermal neutron detectors.

In this study, semiconductors were grown from in-house zone-refined ultra-pure precursor materials using specialized growth furnaces, which were modified, re-coded and optimized to obtain high quality detector materials. Different metal-semiconductor contacts with metals of various work functions and metal-semiconductor-metal (MSM) devices with planar, guard-ring, and large area thin-film structures have been studied to ensure good charge transport properties and opto-electronic device performances. A series of characterization were carried out including scanning electron microscopy (SEM), x-ray diffraction (XRD), glow discharge mass spectroscopy (GDMS), optical absorption study, thermally stimulated current (TSC), deep-level transient spectroscopy (DLTS), and current-voltage (I-V) measurements. These extensive characterizations provided information on stoichiometry, morphology, purity, bandgap energy, resistivity, leakage current and presence of any performance-limiting electrical defect levels. Finally, to determine detection specificity, sensitivity and energy resolution, fabricated detector devices were evaluated with radiation sources, such as ^{241}Am (5.5 MeV) for alpha, ^{137}Cs (662 keV) for gamma, and ^{252}Cf for moderated thermal neutron source.

High quality boron (^{10}B) doped a-Se (As, Cl) alloys were synthesized in a specially designed alloying reactor. Alloy films were deposited using thermal evaporation, a low-cost technique which can be scaled up for large area detector production. The films used for detector fabrication had smooth, defect-free amorphous structure as determined by SEM and XRD. The bandgap and resistivity of ^{10}B-doped a-Se (As, Cl) alloy was determined to be 2.21 eV and $\geq 10^{12}$ Ω-cm, respectively, at 300K. Single layer planer MSM (4″ x 4″) detectors were fabricated on ITO glass and oxidized aluminum substrates. Current-voltage (I-V) characteristics showed very low leakage (~-10 nA at -1000V); by using Al_2O_3 as blocking layer, leakage current was reduced to pA to a fraction of nA at -1000V. Nuclear testing with high energy alpha particles (^{241}Am) and neutron (^{252}Cf) sources showed specific signature of thermal neutron detection. The data confirms that ^{10}B-doped a-Se (As, Cl) alloy films can be used to construct high performance compact neutron detectors.

The CZT crystals were grown at a stoichiometry of $Cd_{0.9}Zn_{0.1}Te$ from zone refined ultra-pure precursor materials with 50% excess Te using modified multi-pass vertical furnace. The bandgap energy was determined to be 1.56 eV. The electrical resistivity was estimated to be ~ 6×10^{10} Ω-cm, which is high enough to fabricate a functional CZT radiation detector. The CZT detectors showed very low leakage current at a high bias (below 5 nA at –1000V) due to their high resistivity, which are beneficial for high resolution detectors. The drift mobility and mobility-lifetime product of electrons were estimated to be 1186 $cm^2/V.s$ and 5.9×10^{-3} cm^2/V, respectively. An energy resolution of 6.2% was obtained for CZT planar detector when irradiated with 60 keV low-energy gamma radiations (^{241}Am). The peaks were sharper and better resolution was observed for the CZT detector with guard ring geometry. An energy resolution of 2.6% was observed for detector with guard-ring structure irradiated with high energy 662 keV gamma radiations using ^{137}Cs radiation source.

Schottky barrier detectors in planar configuration have been fabricated on 50 μm n-type 4H-SiC epitaxial layers grown on 360 μm SiC substrates by depositing ~10 nm nickel (Ni) Schottky contact. Current-voltage (I-V), capacitance-voltage (C-V), and alpha ray spectroscopic measurements were carried out to evaluate the Schottky barrier detector properties. Room temperature I-V measurement revealed a very low leakage current of ~ 0.78 nA at 250 V reverse bias. The barrier height for Ni/4H-SiC Schottky contact was found to be ~1.4 eV and the diode ideality factor was measured to be 1.4, which is slightly higher than unity showing the presence of deep levels as traps and/or recombination centers. Capacitance mode deep level transient spectroscopy (DLTS) revealed the presence of the deep levels along with two shallow level defects related to titanium impurities (Ti(h) and Ti(c)) and an unidentified deep electron trap located at 2.42 eV below the conduction band minimum which is being reported for the first time. The concentration of the lifetime killer $Z_{1/2}$ defects was found to be 1.6×10^{13} cm^{-3}. The detectors' performances were evaluated for alpha particle detection using a ^{241}Am alpha source. An energy resolution of ~ 2.58 % was obtained with a reverse bias of 100 V for 5.48 MeV alpha particles. The measured charge collection efficiency (CCE) was seen to vary as a function of bias voltage. With increased reverse bias, the detector active volume increases with the increase in depletion layer width accommodating more number threading type dislocations at the epilayer/substrate interface resulting in higher FWHM values as observed experimentally.

TABLE OF CONTENTS

LIST OF TABLES

LIST OF FIGURES

LIST OF ABBREVIATIONS

a-Se	Amorphous Selenium
at%	Atomic Percentage
CdTe	Cadmium Telluride
CT	Computer Tomography
C-V	Capacitance-Voltage
CVD	Chemical Vapor Deposition
CZT	Cadmium Zinc Telluride
D.I.	De-Ionized
DLTS	Deep Level Transient Spectroscopy
EBIC	Electron Beam Induced Current
EDAX	Energy Dispersive X-ray Spectroscopy
EM	Electromagnetic
FWHM	Full Width at Half Maxima
GDMS	Glow Discharge Mass Spectroscopy
ITO	Indium Tin Oxide
I-V	Current-Voltage

keV	Kilo Electron Volt
MeV	Mega Electron Volt
MCA	Multi-Channel Analyzer
PET	Positron Emission Tomography
PHS	Pulse Height Spectra
RT	Room Temperature
SEM	Scanning Electron Microscopy
SI	Semi-insulating
SiC	Silicon Carbide
SIMPA	Simultaneous Multiple Peak Analysis
SNM	Special Nuclear Material
THM	Travelling Heater Method
TIR	Transmittance –Infrared
TSC	Thermally Stimulated Current
$\mu\tau$	Mobility-Lifetime Product
XPS	X-ray Photoelectron Spectroscopy
XRD	X-Ray Diffraction
ZR	Zone Refined

CHAPTER 1: GENERAL INTRODUCTION

1.1 DISSERTATION INTRODUCTION

Higher frequency electromagnetic (EM) radiation such as alpha particles, x-rays, gamma-rays, and neutrons are known as ionizing radiation. These radiations contain sufficient quantum energy so that when interacting with matter they could knock out an electron from the orbit of an atom producing positively charged ions. A common source of ionizing radiation is radioactive materials such as uranium (U), as it decays. Radiation detectors are devices that detect and quantitatively measure the intensity of the ionization caused by different nuclear radiations. To measure the radiation, the primary ionization must be preserved; created ions must be collected and not be lost through recombination; the electrical signals produced must be amplified to measure the energy of nuclear interaction. Therefore, detector materials and electronic instrumentation play critical roles in fabricating better nuclear detectors.

Nuclear radiations affect various aspects of our lives. Nuclear energy has become an important component of nations' sustainable energy portfolio. With expansion of nuclear enrichment, there are also growing concerns about the nuclear terrorism risk, a major issue for the national security. Nuclear radiation such as x- and gamma-ray are being used in medical imaging (for example x-ray imaging, CT scan, PET brain imaging machines) to provide valuable diagnostic information. Radionuclides are used to directly treat illnesses, such as radioactive iodine to treat hyperthyroidism and radioactive tracers such as technetium-99 to map heart and surrounding arteries for diminished blood flow. Nuclear radioactive materials are also proliferated to construct nuclear warheads with intention to cause mass destruction.

For nuclear (radioactive) material classification, accounting and safeguards, for measuring the dosage of exposure, for preventing and detecting theft or diversion of special nuclear materials (SNMs), for verification non-proliferation treaty, there is a need for compact, high performance radiation detectors that can accurately identify the type, state, and location of the nuclear materials. When evaluating radiation detectors, the most important criteria are: (i) sensitivity of the detector – what type of radiation (alpha, neutron, gamma or x-ray) the detector will detect, (ii) energy resolution of the detector – how precisely the detector will distinguish between two isotopic radiations, (iii) time resolution of the detector – how high a counting rate will be measured without error/noise, (iv) detector efficiency – the percentage of ionization that will be accurately captured and amplified. As the need for better sensitivity, resolution, and efficiency increases, so does the complexity of the detector structures and its operation, but not one detector available today that could satisfy all the above requirements.

In this dissertation three different types of wide bandgap (WBG) radiation detectors were studied and compared: (1) amorphous selenium (a-Se), (2) cadmium zinc telluride (CZT), and (3) silicon carbide (SiC). All three materials have attractive electrical properties such as wide bandgap energy ($\geq$ 1.5 eV) facilitating room temperature operation, high resistivity ($\geq 10^{10}$ Ω-cm) contributing to low leakage current and thereby low thermal noise for high resolution, and high charge carrier mobility-lifetime product offering high charge collection efficiency.

However, these semiconductors have distinct characteristics that set them apart from one another. For example, high Z (atomic numbers of constituent elements, Cd=48, Zn=30, Te=52) and high density of CZT offering high stopping power to absorb high energy x-rays and gamma-rays so CZT could be used for x- and gamma ray spectrometer at room temperature. On the other hand, SiC has low Z value (Si=14, C=6) appropriate for detection of alpha particles and low energy x-rays (<10 keV) regime. Furthermore, high bandgap energy (~3.27 eV at 300 K) of 4H-SiC allows detector operation well above room temperature (~773 K) as required for nuclear fuel processing environment in nuclear power plants. Amorphous Se alloy with enriched boron (^{10}B) has high thermal neutron cross-section (3840 barns, 10^{-24} cm^2) due to boron and high radiation tolerance due to its amorphous structure, making it a favorable candidate for solid-state neutron detectors.

Therefore, in this dissertation experiments were carried out to study: (1) amorphous selenium (a-Se) based x-ray detectors for medical imaging devices or solid-state thermal neutron detectors for nuclear power plant; (2) cadmium zinc telluride (CZT) based high-energy x-ray and gamma ray detectors for nuclear material accounting and safeguards; and (3) silicon carbide (SiC) based low-energy x-ray and gamma ray detectors that can operate in harsh radioactive environments such as in nuclear weapon complexes and space applications useful for NASA and DOD explorations.

1.2 CURRENTLY AVAILABLE SEMICONDUCTORS FOR RADIATION DETECTOR

The most common radiation detector is the gas proportional counter or Geiger-Muller counter. It uses a gas-filled tube with a central wire at high voltage to collect the ionization produced by incident radiation. It can detect alpha, beta, and gamma radiation although it cannot distinguish between them. Gas detectors can be made rugged but they require high pressures, have timing speed limitations, and long term stability problems. Because of these limitations, it is best used for demonstrations or for radiation environments where only a rough estimate of the amount of radioactivity is needed. [1]

Currently high-purity germanium (HP Ge) detectors are most widely used for gamma-ray spectroscopy; other materials include NaI(TI), mercuric iodide (HgI_2), and CdTe [1, 2]. Germanium (Ge) has a high atomic number, can be produced in large volumes (> 10 cm^3), and has excellent energy resolution of 0.2% using a benchmark 662 keV gamma-ray irradiation [3] at low temperature. Such detectors have applications in environmental radiation and trace element measurements. However, due to its low band gap of 0.67 eV at 300 K, germanium detectors require cryogenic cooling to function properly (<110 K) [4]. This makes the system bulky and increases power consumption to the level where the field applications are complicated. Consequently, there has been an enormous effort to develop room temperature (RT) alternative to Ge.

Scintillator based detectors such as NaI(TI) give off light when radiation interacts with them. The light is detected with an optical detector, most commonly a photomultiplier tube (PMT) or avalanche photodiodes (APD), and then converted to electrical pulses with readout electronics. Response speeds can be quite fast with some scintillators, but main drawbacks are low energy resolution, poor temperature stability, and strong background [5]. Moreover, scintillation detectors have proven difficult to pixelate economically. Such system may be more suitable for large-area standoff imaging system, as used in portal applications [2]. In general, solid-state “direct read-out” semiconductor detectors have proven to be very versatile. In such semiconductors, only a few eV are necessary to create an electron-hole pair (compared to 50 eV or more of energy in scintillators); thus a much greater signal is generated for a given amount of energy deposited.

Mercuric iodide (HgI_2) has a high stopping power due to high atomic numbers (Hg = 80 and I = 53) and wide band-gap (2.13 eV at 300 K) for possibility of room temperature operation with low leakage current [6]. Nevertheless HgI_2 demonstrates very poor charge transport properties due to low mobilities of both electron and hole limiting charge collection efficiency. Mercuric iodide also requires encasement, since it is hygroscopic and a soft material [7]. This restricts its widespread use as a high energy gamma-ray detector.

Cadmium telluride (CdTe) is a good choice for nuclear detection due to its good charge transport properties, however the bandgap of CdTe cannot be tuned above 1.5 eV, and it has a resistivity of $\sim 10^8 - 10^9$ Ω-cm, which is less than ideal for noise performance reasons [8]. However, inclusion of Zn in CdTe increased the bandgap energy to a range of 1.50 – 1.90 eV resulting in higher resistivity of 10^{11} Ω-cm [9]. CdZnTe (CZT) demonstrated capability of room temperature operation and an energy resolution of ≤ 2% resolution at 662 keV with up to 1.5 cm crystal length [10]. In Table 1.1**,** properties of various commercially available and prospective semiconductors are compared with the ideal detector materials.

Table 1.1. Properties of commercial (bold) and prospective (italic) semiconductors for direct read-out radiation detectors

Semi-conductor	**Energy bandgap at 300 K E_g (eV)**	**Growth T_{MP} (^{o}C)**	**Atomic number Z**	**Density (g/cm^3)**	**Electron-hole pair creation energy, W (eV)**	**Resistivity (Ω-cm)**	**Mobility, μ (cm^2/Vs) hole/electron**	**Carrier lifetime, τ (x10^{-6}sec)**	**Mobility-lifetime product of electron $\mu\tau_e$ (cm^2/V)**	**Handling; crystal growth**
Ideal	1.6- 2.1	700-1200	>50^a	-	<3E_g	$\geq 10^{10}$	-	-	$\geq 10^{-3}$	Robust; Non-hygroscopic
Ge	0.67	938	32	5.33	2.96	50	1900/3900	≥300	0.57	Excellent; Growable
HgI_2	2.1	260	80, 53	6.4	~4.2	10^{12}	4/100	~2	10^{-4}	Very soft; Difficult to grow
CdTe	1.5	950-1085	48, 52	6.2	4.43	10^{9}	100/1100	0.4	0.4×10^{-3}	Small crystal domains
CdZnTe (CZT)	1.6-1.9	1175	52	5.78	4.6	$>10^{10}$	50/1000	~1	10^{-3}	Small crystal domains
4H-SiC	3.27	1550-1750	14, 6	3.21	7.28	$>10^{12}$	115/1020	~1	0.8×10^{-3}	Polytype inclusions, high temperature and defects
a-Se alloy	2.24	365-485	34	4.29	~50	$\sim10^{13}$	0.12/0.04	342	1.4×10^{-5}	Large area detector possible

a: For detection of high energy x-ray and gamma ray

Note: Data were collected from these references: [2, 6, 8, 9, 10, 11, 12].

1.3 CHOICE OF A-SE, CZT, AND SIC AS RADIATION DETECTORS

In order for a detector to detect and quantify the ionization radiations caused by nuclear material, it must be able to absorb nuclear radiation, generate electron-hole charge pairs, and transport the charge pairs across the detector material to be collected by readout electronics. Therefore, semiconductor materials for nuclear detectors must offer following material properties:

- Large bandgap energy ($\geq$ 1.5 eV at 300 K) contributing to low thermal noise (generation of electron-hole pair is due to ionization by radiation only not due to elevated temperature)
- High resistivity ($\geq 10^{10}$ Ω-cm), for low leakage current, thereby low noise
- Small electron–hole pair generation energy so that more charge carriers could be generated by the incident radiation
- High mobility lifetime product ($\mu\tau \geq 10^{-3}$ cm^2/V) for both electrons and holes for good charge transport properties so that probability of charge collection will be high and recombination is low
- Low dielectric constant and high intrinsic mean drift length for faster collection time thereby better time resolution
- High atomic number and density to stop high energy x- and gamma-ray
- High atomic displacement energy for radiation hardness, damage resistance
- High thermal conductivity for high temperature operation

Nuclear radiations from radioactive materials cover a vast energy range from a few eV (soft x-rays) to MeV (high energy gamma rays). A single detector may not be ideal to capture this wide range of radiations. Thus there are various distinct applications of the radiation detectors and each application will impose certain requirements.

As can be seen in Table 1.1 semiconductors CZT, a-Se, and SiC have several favorable properties for nuclear detectors. These semiconductors were first chosen for the research project because of their inherent wide bandgap energy and high resistivity that will imply low thermal generation of charge carriers that is independent of the incoming radiation, leading to low thermal noise and high resolution. Radiation detectors based on these materials, therefore, are able to operate at or above room temperature (~300 K) without any need for cooling with liquid nitrogen, thus allowing possibility of portable compact detector device. These semiconductors also offer direct readout meaning that incident radiation is directly converted to electrical response unlike scintillators where incoming radiation is first converted into light then a second detector system converts light to electrical response.

CZT has higher density and higher atomic number offering stopping power to absorb high energy x-rays and gamma-rays so CZT could be used for x- and gamma ray spectrometers. Furthermore, CZT has tunable bandgap energy (depending on Zn concentration), higher density, low electron-hole pair generation energy, and high electron mobility which are ideal for gamma radiation detectors. Such detectors could be used for screening of radioactive materials and radiological dispersal devices (RDDs) at the ports-of-entry, for detecting illicit radioactive enrichment, nuclear weapons and their components during verification of non-proliferation treaty, for monitoring and management of nuclear waste at nuclear power plants, and for hard x-ray and gamma ray imaging of space for future NASA or DOD exploration missions.

However, hole mobility of CZT is several orders of magnitude less than electron mobility (μ_h = 50 cm^2/Vs compared to μ_e = 1000 cm^2/Vs), thereby giving rise to a relative stationary hole movement within the electron collection time [12]. Since detection signals are a composite of both the electron and hole signals, the resulting spectrum will yield incomplete information about the incident radiation. To compensate for the effects of poor hole trapping, special detector structures such as small pixel, Frisch grid, guard ring could be adapted where readout signal is due to electron movement only [13]. CZT also suffers from poor crystal yield due to defects and inhomogeneity, making the material very costly [14]. With continued growth experiments, it is hoped that CZT will become more cost effective to produce and will become an effective replacement of cumbersome Ge gamma-ray detectors.

Amorphous selenium (a-Se) offers the highest resistivity (10^{13}) among the three semiconductors chosen for the study, thus has potential for very low thermal noise. Although a-Se does not have high enough Z value (atomic number = 34) to stop gamma rays, it has enough stopping capabilities for x-rays and has commercially being used for mammography [15, 16]. Unlike crystalline semiconductors such as CZT, a-Se alloy growth process requires relatively low temperature (365 - 485°C), and thick layer (500 μm) could be deposited via low cost technique such as thermal evaporation to obtain large area detectors. The characteristics such as high thermal neutron cross-section (3840 barns, 1 barn = 10^{-24} cm^2), low effective atomic number of Se for small gamma ray sensitivity, and high radiation tolerance due to its amorphous structure, makes a-Se a favorable candidate for solid-state thermal neutron detectors [17, 18, 19]. Existing gas proportional counters used for neutron detection employ ^{3}He gas, however, there is a world-wide shortage of ^{3}He gas, so a-Se will offer solid-state neutron detection system without the requirement of ^{3}He gas. In addition to current applications in medical imaging such as x-ray mammography, a-Se neutron detectors will find extensive use in nuclear power plants including safeguard of special nuclear materials (SNMs), reactor instrumentation, process monitoring, and nuclear waste management.

Drawbacks of a-Se are it's much higher than ideal electron-hole pair creation energy (~50 eV, 22 times of bandgap energy) and poor charge transport properties ($\mu\tau_e = 1.4\times10^{-5}$ cm^2/V). High field has been applied to generate charge carries in the avalanche field region to reduce the electron-hole pair production energy form 50 eV to ~12.5 eV [20, 21]. Transport properties of electron and holes are reported to be improved by alloying a-Se with As and Cl doping, which also helps in stabilizing the amorphous structure [22, 23].

Silicon carbide is an indirect wide band-gap semiconductor. Although there are many polytypes (variations of crystal structure), 4H-SiC is the preferred one for electronic devices due to better electrical properties [24]. Wide bandgap energy, high breakdown electric field, high carrier saturation drift velocity, and high atom displacement energy make 4H-SiC a potential candidate for nuclear detectors. Epitaxial layer of SiC is highly crystalline which offers superior electronic properties that are appropriate for nuclear radiation detection. High bandgap energy (~3.27 eV at 300 K) of 4H-SiC allows detector operation well above room temperature (~773 K) and extremely low leakage currents (low noise) at operating bias (~ tens of pA for 20 μm 4H-SiC epilayers). Because of low Z value SiC is appropriate for detectors of low energy x-ray (<10 keV) regime. SiC is a highly radiation hard material because of high displacement energies of the constituent elements, making it available for detectors that are deployed in harsh environments such as high radiation field in the upper atmosphere and/or outer space. Therefore SiC based soft x-ray detector will find its application in NASA's astronomical planet finding missions.

One of the primary obstacles to development of SiC devices is the presence of various defects in device structures. These defects in SiC include dislocations, micropipes, grain boundaries, stacking faults, and have detrimental effects on device performance [25, 26, 27]. For example, dislocations are the primary defects in SiC that affect the current-voltage (I–V) characteristics of devices and micropipes significantly affect device leakage current and breakdown voltage. Therefore defect-device performance correlation is an import study in order to achieve optimum detectors. In this dissertation research a significant amount of time was spend for defect analysis using techniques such as electron beam induced current (EBIC), thermally stimulated current (TSC), and deep level transient spectroscopy (DLTS).

In summary, all three materials have their own merits as nuclear detectors, and with respect to their inherent properties, they capture different types of nuclear radiation, offering diverse nuclear detectors applications (cf. Table 1.2). They also have some inadequacy which must be resolved in order to achieve the goal of high performance nuclear detectors based on these materials. Table 1.3 summarizes strategies that will require in resolving these significant issues. These strategies were explored during the dissertation research and are described in details in the subsequent chapters.

Table 1.2. Weighing pros and cons of the wide bandgap semiconductors that are investigated in this study

	a-Se	**CZT**	**4H-SiC**
Advantages	• Highest resistivity 10^{13} Ω-cm • Atomic number, Z (34), high enough to stop x-rays • High thermal neutron cross sections with B-10 doped a-Se alloys • Low temperature growth (365 – 485 °C) • Possibility of low-cost, large-area detector	• High mobility (μ) • Atomic number Z high enough to stop hard x-ray and gamma rays • Very low electron-hole pair creation energy (~4.28 eV) • Good electron mobility (~1000 $cm^2/V.s$ • Room temperature operation	• High bandgap, so very low leakage current (low noise) • High temperature operation (≥773 K) • Possibility of large-area • Highly radiation hard suitable for harsh environments • Low Z, good for soft x-rays
Disadvantages	• Radiation damage at high gamma doses • Relatively low mobility (could be improved by selective doping) • Relatively high electron-hole pair creation energy (high electric field could be applied to lower this)	• Hole mobility is much lower than electron mobility, energy resolution could be improved by single carrier detector structure • Large area is not possible • High cost	• Material quality not optimized yet (presence of device killer defects) • High temperature growth
Applications	• x-ray, gamma-ray, and thermal neutron detectors • Process monitoring and nuclear waste management at nuclear power plants • Homeland security • Medical imaging (mammography)	• Hard x-ray and γ-ray detectors • Screening at ports of entry, non-proliferation treaty verification • NASA space mission • Medical imaging (PET and CT)	• Low energy x- and gamma ray • In high radiation field NASA applications such as planet finding mission • Nuclear power plants

Table 1.3. Issues concerning a-Se, CZT, and SiC as radiation detector materials and intended mitigation strategies

Issues/Risks	Mitigation Strategies
Low resistivity	• Compensating doping • Post-growth annealing and component overpressure growth
Low electron mobility	• Reduce carrier-scattering defect densities by isoelectronic doping
Low hole mobility	• Use Frisch grid, coplanar, or small pixel detector structure so that single electron transport mechanism holds
Low carrier recombination time	• Analyze impurity concentrations • DLTS to identify and quantify deep levels • Microscopy to correlate inclusions and grain boundaries
Low breakdown voltage	• Correlate to native defects, non-stoichiometry, and ionizing centers • Correlate to different surface treatments and passivation

1.4 DISSERTATION OVERVIEW

This study conducts a comparative investigation of three wide-bandgap semiconductors – a-Se, CZT, and SiC – for nuclear radiation detection applications. The research was centered on four key areas: (i) precursor material purification and crystal growth experiments; (ii) material and detector characterization to evaluate crystal quality and device attributes such as resistivity, breakdown voltage, carrier mobility, carrier lifetimes, contact performance, and their contribution in device applications; (iii) defect analysis to understand the impact of native defects on electrical properties and how they affect device characteristics and their performances; (iv) device fabrication and evaluation of nuclear detector with radiation sources to determine detector sensitivity, resolution, and efficiency. The results obtained were crucial information about the controllable variables for optimum detection performance.

This dissertation is divided into five chapters. Chapter 1 provides a background, review of the existing nuclear detectors, properties of ideal nuclear detectors, and motivation for selecting a-Se, CZT, and SiC as detector materials for present study.

Chapter 2 describes the experiments carried out to develop a new high performance thermal neutron detector based on enriched boron (^{10}B) doped a-Se (As, Cl) detectors. First, purification of selenium (Se) precursor material by zone purification and subsequent impurity analysis by glow discharge mass spectroscopy was carried out. Synthesis of boron doped a-Se alloys was performed in a specially designed alloying reactor. Trace amount of arsenic (As) and chlorine (Cl) were added to the alloy composition to stabilize the amorphous structure, a requirement for high resistivity. Large area alloy films were prepared by thermal evaporation and characterized by different techniques such as scanning electron microscopy (SEM), x-ray diffraction (XRD), electron beam induced current (EBIC), and current-voltage (I-V) measurements. Monolithic metal-semiconductor-metal (MSM) detector structures were fabricated using various metals of different work functions for Schottky contact analysis. A thermionic emission model has been used to study the Schottky contacts. Finally, nuclear detector performance evaluations with ^{241}Am alpha source and ^{252}Cf neutron source were carried out and detection resolution were measured from Pulse Height Spectra (PHS) measurements.

Chapter 3 details the investigation performed on the CZT detectors. Unlike a-Se detectors where thin- films are used for nuclear detector, large single crystals are used to fabricate CZT detectors for hard x-ray and gamma radiation detection. This chapter describes a novel crystal growth methodology using excess tellurium (Te) as the solvent; this method is a modified Bridgman growth method where some advantageous aspects of travelling heater method have been incorporated. Furthermore control electronics were customized for growth ampoule pulling and rotation along with automation via H-Bridge motor controller and Arduino microcontroller to ensure growth of high quality homogeneous crystals. The characterization includes analysis of the stoichiometry of the grown crystals, optical characterization using UV-Vis spectroscopy, defect analysis by thermally stimulated current spectroscopy (TSC) and electron beam induced current (EBIC) imaging, and electrical characterization using I-V, and C-V measurements. Two type of detector structures namely “planar” and “guard-ring” geometry were fabricated and evaluated for carrier (electron and hole) transport properties such as mobility and mobility-lifetime products. The fabricated detectors are characterized using Pulse Height

Spectra (PHS) measurements for radiation testing using x-ray and gamma-ray sources. Further analysis of fabricated detectors was performed using biparametric correlation.

Chapter 4 describes the fabrication and performance of radiation detectors based on n-type 4H-SiC epitaxial layer grown on off-axis bulk SiC crystals. First, radiation detectors were fabricated using low-leakage current and low-defect bearing 4H-SiC n-type epilayer on high-purity low resistive 4H-SiC wafers. Detailed defect characterization using deep level transient spectroscopy (DLTS) and electrical characterizations using current-voltage, and capacitance-voltage measurements were carried out for high purity n-type 4H-SiC epitaxial layers. A systematic study was conducted to evaluate performance of 4H-SiC n-type epilayer detectors as alpha particles and low energy x-ray and gamma radiation detectors.

Finally, Chapter 5 concludes the research presented in this dissertation. A brief review of the current challenges and suggestions for future work are also provided.

CHAPTER 2: AMORPHOUS SELENIUM THERMAL NEUTRON DETECTOR

2.1 OVERVIEW

This chapter details the experiments carried out to develop enriched boron (^{10}B) doped a-Se (As, Cl) alloy film detectors for thermal neutron detection. Such a solid-state nuclear detector will be employed for safeguards of nuclear materials and spent fuel at nuclear power plants, verification of international non-proliferation treaty, and surveillance of nuclear terrorism activities for national security. To develop high performance a-Se neutron detectors a series of experiments were carried out including a-Se alloy material preparation, optimization of alloy composition, film preparation and characterizations, detector fabrication and electrical characterization, and finally, testing with radiation sources. Detection performance was evaluated with single layer planar (up to 4″ x 4″ area and varying thicknesses of 65-300 μm thick) detectors using high energy alpha particles and neutron sources. The ^{10}B-doped a-Se (As, Cl) alloy detectors grown from highly resistive alloy film contributed very low electrical noise to the readout spectra under high voltage bias, and showed specific signature of thermal neutron detection.

2.2 CONSIDERATIONS FOR A-SE NEUTRON DETECTOR

Amorphous selenium (a-Se) alloy materials have become highly-demanding as a xerographic photoreceptor and a direct conversion x-ray detector material for medical imaging applications [28, 29] including digital mammography [30] and digital chest radiology [31, 32]. This is mainly due to its ability of operating in very high reverse bias voltage without breakdown while maintaining very low dark leakage current attributed to its high resistive nature and its feasibility of large-area thin-film deposition [29, 33, 34]. In this dissertation, a novel concept was implemented by doping a-Se alloys with enriched boron (^{10}B) to detect alpha particles which are surrogate for thermal neutrons. With the expansion of nuclear power, there are growing concerns about the nuclear proliferation and nuclear terrorism risk. High performance, solid-state nuclear spectrometers will be employed for safeguards of enriched materials and spent fuel, verification of non-proliferation treaty, and surveillance of nuclear terrorism activities.

Current neutron detection system such as the gas proportional counters are inadequate by their stability of response, speed of operation, size, and recently by world-wide shortage of ^{3}He gas used in this system. Thus a-Se based solid-state neutron detection system will offer an alternative compact design without the requirement of ^{3}He. Amorphous selenium (a-Se) has many favorable characteristics for a neutron detector - a high thermal neutron cross-section (3840 barns, 1 barn = 10^{-24} cm^{2}), a wide bandgap (2.22 eV at 300 K) which allows room temperature operation, high radiation tolerance due to its amorphous structure, and low effective atomic number of Se for small gamma ray sensitivity offering easy gamma ray discrimination. Presence of ^{10}B is essential to capture thermal neutrons. When captured by the ^{10}B nucleus, thermal neutrons undergo the following reaction, producing two energetic charged particles [35].

$$^{10}\mathrm{B} + {}^{1}\mathrm{n}_0 \text{ (neutron)} \longrightarrow {}^{7}\mathrm{Li} + {}^{4}\mathrm{He}\,(\alpha) + 2.79 \text{ MeV} \tag{2.1}$$

The kinetic energy of the charged particles excites electrons in the valence band of a-Se lattice expelling the electrons into the conduction band and thereby producing holes in the valence band. The generated charge carriers (electrons and holes) are free to move, and under an electric field across the a-Se film, they travel to their respective electrodes producing a measurable electrical current signal. Charge-sensitive amplifier electronics are used to measure the current pulses indicating the occurrence of a thermal neutron capture event. Figure 2.1 shows a schematic of neutron capture by enriched boron and resulting charge carrier generation in the a-Se film.

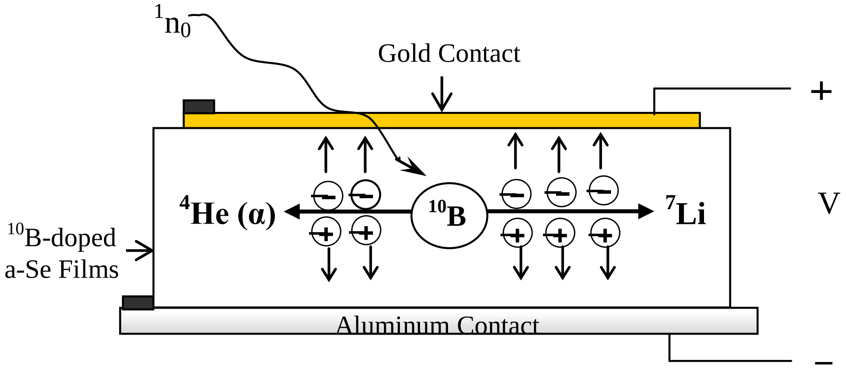

Figure 2.1. Conceptual design of a thermal neutron detector using B-doped a-Se

In this study to develop high performance a-Se alloy neutron detectors, first alloy composition was optimized to ensure good opto-electronic properties. Second, a series of characterizations were carried out such as scanning electron microscopy (SEM), x-ray diffraction (XRD), glow discharge mass spectroscopy (GDMS), optical absorption study, current-voltage (I-V) measurements to identify presence of any performance-limiting factors. Then boron (^{10}B) doped a-Se (As, Cl) alloy detectors were fabricated and radiation detection performance was evaluated using high energy alpha particles and neutron sources. The following sections provide experimental parameters and results on the research work carried out on a-Se neutron detectors.

2.3 SELENIUM ALLOY PREPARATION

2.3.1 Zone Purification of Precursors

Semiconductors' opto-electronic properties of crystals are strongly and negatively influenced by the presence of trace levels of residual impurities since they reduce substantially charge carrier transport properties. Under high electrical field operation, impurities might cause harmful native defects which may act as recombination centers and significantly deteriorate charge carrier transport properties and collection efficiency. These defects/trapping centers could also lead to charge build up hence hindering the uniformity of the electric response across the detector volume. Commercially available selenium material is of 5N purity (99.999%) and cannot be used in radiation detector devices since a-Se is highly sensitive to material impurity. Therefore, zone refining (ZR) process was carried out on the commercially available Se to obtain a-Se material of ~7N purities (impurity at ppb level or lower) for successful applications as radiation detectors.

Zone refining technique [36] relies on the idea that impurities are distributed differently in their solid and liquid phases at equilibrium. If C_s is the impurity concentration in the solid phase, and C_l is the impurity concentration in the liquid phase, then the segregation constant k refers to the relative concentration of impurities in the solid crystal compared to that of the melt:

$$k = \frac{C_s}{C_l} \tag{2.2}$$

If a small zone of a material is melted with the remainder of the material remaining solid, impurities will collect in this molten zone when k < 1. Figure 2.2 illustrates the ZR process. A section of the material at one end is melted, and the molten zone is passed through the feed material very slowly by moving the heater very slowly towards the other end of the ampoule. The impurities get dissolved in the molten zone and transported through the material from one end to other. Thus most of the impurities will be collected in one end of the material, and the remainder of the material will be relatively pure. If this process is repeated multiple times further purification of the material is achieved, and eventually a highly pure material could be obtained [37, 38]. Just as with the impurities, the portion of the ingot containing pure precursor material is purified further due to more zone passes [37].

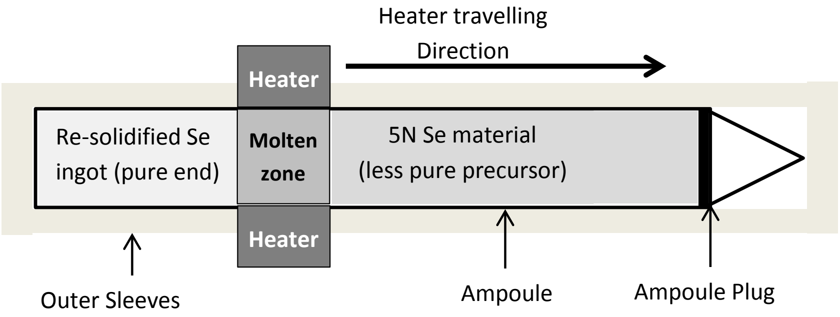

Figure 2.2. Schematic of zone refining process, showing the solidified pure end, molten zone material where impurity segregation occurs, and there is yet more precursor material to be purified.

Figure 2.3. ZR a-Se ingots (~7N) in quartz ampoules after multi-pass zone purification.

Commercially available 5N selenium (Alpha Aesar) was purified using an in-house horizontal zone refining (ZR) system. First, the quartz ampoule was thoroughly cleaned using successive washes with acetone, methanol, 10% HF aqueous solution and de-ionized water (18 MΩ) and then baked overnight at 950°C under a constant nitrogen flow (~0.25 liter/min). The ampoule was loaded with 5N Se, sealed and then suspended over the track actuator in the horizontal ZR system. The ZR system uses a single zone furnace mounted on a track actuator which is controlled using an Arduino electronics microcontroller that can be programmed to perform motor control. The heater temperature was maintained at about 255°C (melting point of Se is 221°C) using a temperature controller. Using Arduino program the motion of the heater was controlled at ~ 4 cm/hr. Once the heater passed the entire length of ampoule (constitutes for one ZR pass), the heater was then quickly returned to its original position. About 40 ZR passes were carried out which took around 32 days.

A yield of ~85% purified material with ~7N purity was obtained after the completion of ZR process [18]. Photographs of typical ZR ampoule after completion of zone purification for Se are shown in Figure 2.3 with impurities segregated to the right end of the ampoule, and pure precursor material on the left side of the ampoule. After completion of the ZR process, the ampoule was cut and the zone-refined material was removed inside an argon-controlled glove box. Depending on uniformity of shiny color, a length of ingot was considered 'pure' material, and cropped from the impure end of the ingot. The removed 'pure' precursor material was then stored in argon filled polyethylene bottles until they were ready to be used in the alloy materials synthesis.

Table 2.1. Impurity analysis by GDMS showing reduction in elemental impurity concentration in Se material after zone-purification.

Element	Concentration before ZR	Concentration after ZR
Se	Major	Major
Hg	5-9 ppm	<3 ppb
Pb	10-15 ppm	<6 ppb
Sn	12 ppb	Not Detected
Ag	5-6 ppm	Not Detected
Cu	20-25 ppm	0.2 ppm
Fe	12 ppm	Not Detected
Mg	4-6 ppm	Not Detected
Si	3-5 ppm	0.4 ppm
Te	6-8 ppm	0.35 ppm
H_2O	10-12 ppm	Not Detected

To examine the effectiveness of ZR process, zone-refined selenium were analyzed using glow discharge mass spectrometry (GDMS) to determine the presence and concentration of different impurities and compared to that of non-ZR Se samples. A typical GDMS analysis data after 40 ZR passes are presented in Table 2.1. The data clearly demonstrated that most of the major impurity concentrations were reduced to ppb level or lower. The results confirmed that purification by ZR process reduced several impurities (which can act as defect center) in commercially bought Se precursor.

2.3.2 Alloy Synthesis

It is well known that unalloyed a-Se material is prone to crystallization [10, 28]. In order to use a-Se in high energy radiation detector applications or for medical imaging devices, alloying with various elements for stabilizing is a necessity. A very effective way for retarding the a-Se crystallization is to alloy it with arsenic (As) in the range of 0.3%-0.6%. While this specific amount of As keeps the p-type properties of a-Se and prevents the crystallization, as a tradeoff, it decreases hole lifetime resulting in decreased hole properties of the material. To overcome this drawback, a-Se is further alloyed with chlorine (Cl) in the parts-per-million (ppm) range. Careful control of the alloy composition is therefore instrumental in ensuring optimum detector performance.

For the preparation of stabilized a-Se (As, Cl) alloys with controlled electrical properties, a custom designed alloying reactor was used. The reactor operation is customized with a specific temperature profile for each alloy. The process cycle was operated in a glove box maintained in a pure argon atmosphere. A picture of the alloying reactor with the reactor schematic is shown in Figure 2.4. The aim was to have a final mixture containing ~0.5% As and ~5ppm Cl to keep physical and electrical properties of the alloy in an optimum level. Using ZR Se, a successive synthesis of different master alloys, as listed below, were carried out to prepare a-Se (As, Cl) bulk alloy.

- Synthesis of Se-As master alloys at 658-700°C, using ZR a-Se and 7N As
- Synthesis of Se-Cl master alloys at 345-355°C, using ZR a-Se and $SeCl_2$ gas

- Synthesis of a-Se (As, Cl) bulk alloys at 465-485°C, using ZR a-Se, Se-As master alloy, and Se-Cl master alloy.

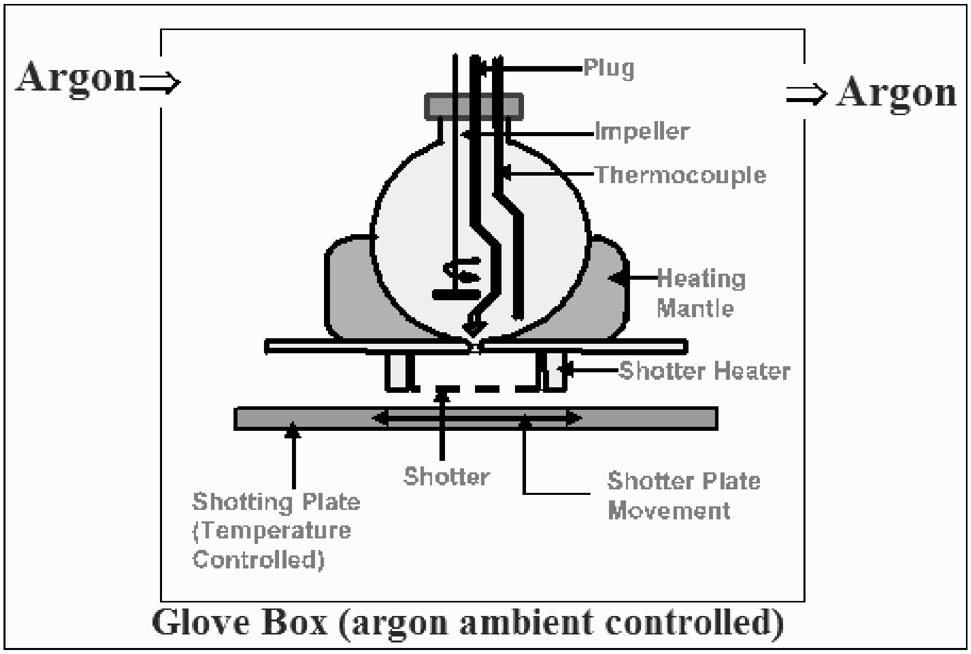

Figure 2.4. Schematic diagram (top) and a picture (bottom) of a-Se alloying reactor.

Boron-doped a-Se (As, Cl) alloy materials were prepared in the pelletizing alloy reactor as used to synthesize a-Se alloys and is shown in Figure 2.4. The alloy reactor was heated in a controlled manner using a PID temperature controller (Omega) to 465°C and a rotating impeller (400-450 rpm) mixed the precursors to ensure homogeneity. After 5 hours, the melt was cooled to 355°C and shotting was performed with Stainless Steel 316 shotter maintained at 360°C on a shotter plate at 5°C. When the melt reached the shotting plate, it was quenched due to rapid decrease of temperature and it formed an amorphous phase. The alloying parameters such as height (dynamic relaxation effect) of a-Se (B, As, Cl) liquid melt in the shotter, synthesis temperature vs. time, and shotting plate temperature are very important and were observed closely. A typical temperature profile with alloying time for one process run is presented in Figure 2.5. The phase diagram of the B-Se system is presented in Figure 2.6.

The phase diagram of the B-Se (Figure 2.6) show that the thermodynamics of B- alloy formation has some problems associated with an immiscibility-gap on the selenium rich side and with formation of B_2Se_3 compound which is very stable and has a very low vapor pressure. These problems were overcome by heat treating the alloy melt at elevated temperature of 475 °C for 10-15 min. Furthermore, the activity coefficient of B in the B-Se system is very low and hence so is the partial pressure of boron. To overcome this problem, two different concentrated alloys of mono-dispersed boron in a-Se (As, Cl) matrix was prepared in order to increase the activity coefficient of boron. The key was to avoid the reaction of boron with selenium and successively increase boron concentrations in pre-synthesized alloys. The physical appearances of the synthesized bulk a-Se (As, Cl) alloys and B-doped a-Se (As, Cl) alloys are shown in Figure 2.7. The synthesized alloys have a dark color with shiny surface on one side.

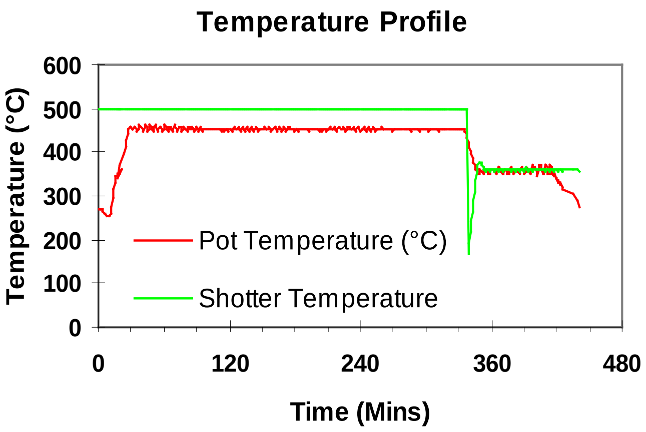

Figure 2.5. Temperature profile (Temperature vs. Time characteristics) for ^{10}B-doped a-Se (As, Cl) bulk alloy synthesis.

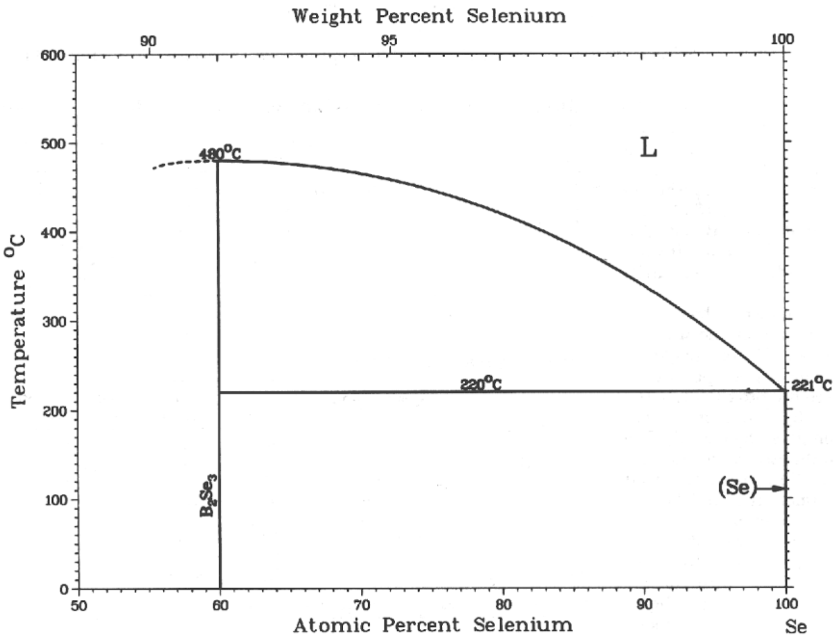

Figure 2.6. The phase diagram of B-Se alloy system.

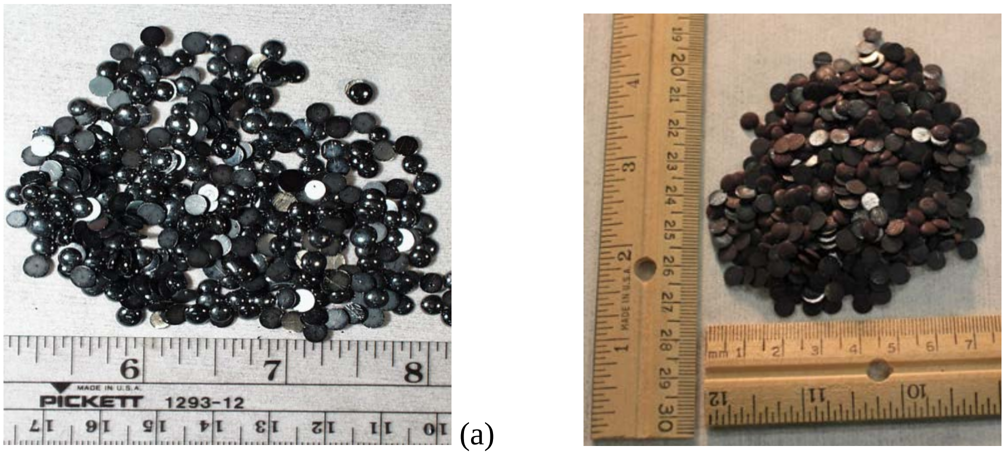

(a) (b)

Figure 2.7. (a) Dry pellets of a-Se (~0.52% As, 5ppm Cl) alloys and (b) ^{10}B-doped a-Se (~0.52% As, 5ppm Cl) alloys.

2.4 SELENIUM ALLOY FILM DEPOSITION

2.4.1 Substrate Preparation

After alloy synthesis, various alloy films with different thicknesses were deposited over aluminum and ITO coated glass substrates by carefully controlling the thin film deposition process. Substrates were prepared before films were deposited to ensure surface uniformity and improved adhesion. Indium tin oxide (ITO) coated TEC-7 or TEC-15 glass substrates and aluminum oxide substrates (up to 10 × 10 cm^2 in area) were used for the study. Benefit of aluminum oxide substrates is that it could act as blocking layer for the injection of electrons from the respective negatively biased electrode. ITO coated glass substrates were rinsed successively in ethanol, in acetone, followed by sonication with isopropanol, and finally with deionized water; and then they were dried by blowing nitrogen (N_2) gas.

Aluminum (Al) substrate of following specifications: 1100 grade, ~3×10^{-6} Ω-cm electrical resistivity; sheet of thickness 0.032″, was purchased from McMaster-Carr company. Next Al substrates were washed with soft soap detergent and water to remove any grease and dust from the surfaces. Abrasives used in polishing Al may become embedded in the surface due to softness of 1100 grade Al sheets, and may transfer larger particulates to finer stages of polishing. The metal sheets were already planar; therefore the mechanical grinding stage was skipped completely in order to eliminate unnecessary scratching and pitting by large-grit abrasives. The cleaned substrates were mounted flat on teflon cylindrical studs by molten red wax, then cleaned thoroughly with acetone and isopropanol. Fine polishing of the Al substrate surfaces were carried out by using a suspension of 1 µm alumina (Al_2O_3) powder D.I. (deionized) water (~50 g/500 ml H_2O) on short nap cloth disk (micro-cloth acquired from Buehler) at polishing wheel speed about 500 rpm for 10 minutes. The Al substrates were then ultrasonically cleaned in D.I. water for about 5 minutes to remove any remaining abrasives. For chemical polishing, the substrates were laid in an acid bath composed of 75 ml H_2SO_4 (1N), 150 ml H_3PO_4 (85% w/w) and 10 ml HNO_3 (68-70% ACS reagent grade) at 65 °C temperature for 2 minutes, followed immediately by washing in D.I. water and drying with a N_2 gun. For the formation of Al_2O_3 passivation layer on the Al-substrate, the polished Al-substrates were oxidized in an open air in a pre-profiled furnace at 375 °C for about an hour resulting in a visibly white Al_2O_3 layer on the substrate surfaces.

2.4.2 Film Deposition by Thermal Evaporation

The film deposition was carried out using in-house thermal evaporation facilities (CHA SE 600 evaporator). Figure 2.8 shows the schematic of the thermal evaporator system used for a-Se (As, Cl) alloy film preparation. This evaporator is equipped with planetary rotation system for substrate rotation. Substrate temperature accessories and vacuum fixtures (capable of a vacuum pressure of 2×10^{-8} torr) are installed within the thermal evaporation system. The mounting capabilities inside the vacuum chamber of the thermal evaporation system were modified so that two large area (10×10 cm^2) films, two 5×5 cm^2, and two 2.5×2.5 cm^2 films (sister samples) could be produced in each deposition cycles. Film depositions are monitored by a quartz crystal thickness monitor. A test sample is placed with the depositions and the corresponding film thickness was measured by Dektak IIA surface profilometer.

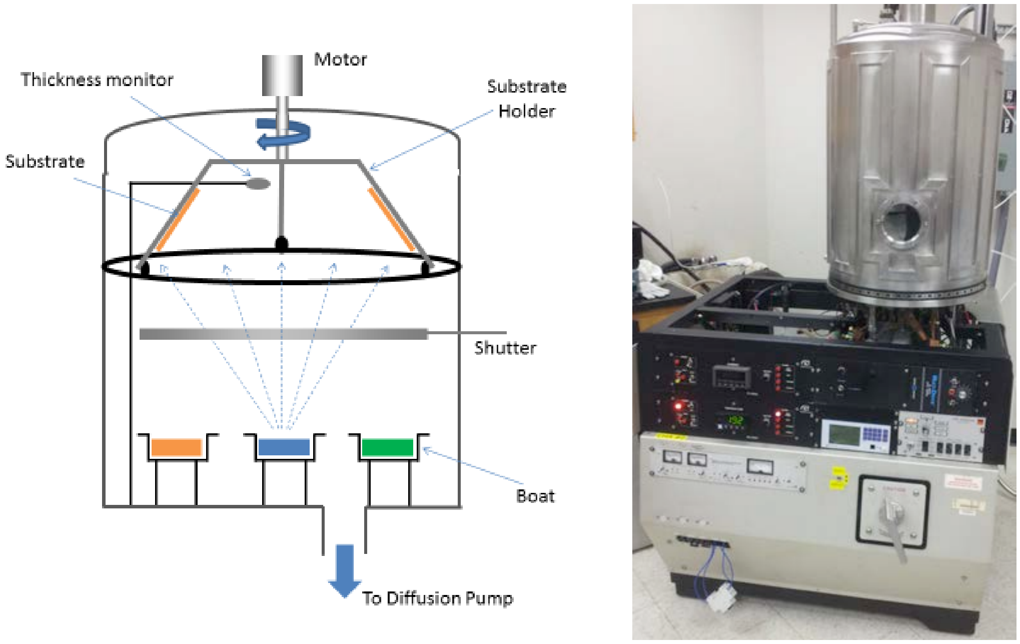

(a) (b)

Figure 2.8. (a) Schematic of thermal evaporator system and accessories and (b) a picture of in-house CHA-SE600 thermal evaporation system used for a-Se alloy films.

For a-Se film deposition, first the prepared substrates of different sizes placed on the planetary rotating discs where they were held by thin tungsten wires placed on the edges. The bulk alloy was then measured and loaded in a molybdenum or a tungsten boat. The vacuum chamber was evacuated to about 2×10^{-6} torr and the chamber temperature was raised to ~ 100 °C in order to get rid of any moisture or residual gases. After about few minutes at ~100 °C, the temperature was lowered to 60 °C. To grow amorphous structure, deposition of a-Se required a substrate temperature of 60-65 ^{o}C. As Se has poor thermal conductivity and low glass transition temperature (~50 $^{\circ}$C), it is crucial to control the substrate temperature during the deposition process, otherwise the alloy film could easily become polycrystalline. Thus the substrate temperature was monitored and precisely controlled during the deposition process to keep the deposited films with homogeneous amorphous structure all over the film surface. The vacuum during the deposition process kept in a minimum level ~10^{-6} torr and increment of the boat current was controlled precisely for smoother a-Se phase transitions. After the deposition runs, no polycrystallinity or grains were observed on the films.

An Inficon XTC/2 thin-film deposition controller connected to a quartz crystal thickness monitor was programmed for automated deposition of a-Se alloy films. The tooling factor was precisely calculated in order to accurately control the deposited film thickness within ± 1% of the desired value. B-doped a-Se (As, Cl) alloy films up to 100 cm^2 in area grown on ITO coated glass substrates are presented in Figure 2.9. The appearance of B-doped a-Se (As, Cl) alloy films of different sizes grown on oxidized aluminum substrates in a single deposition run are also shown in Figure 2.10. The structural, physical, and electrical characterization of a-Se (As, Cl) films on ITO coated glass and Al substrates were carried out in details as described in the next section.

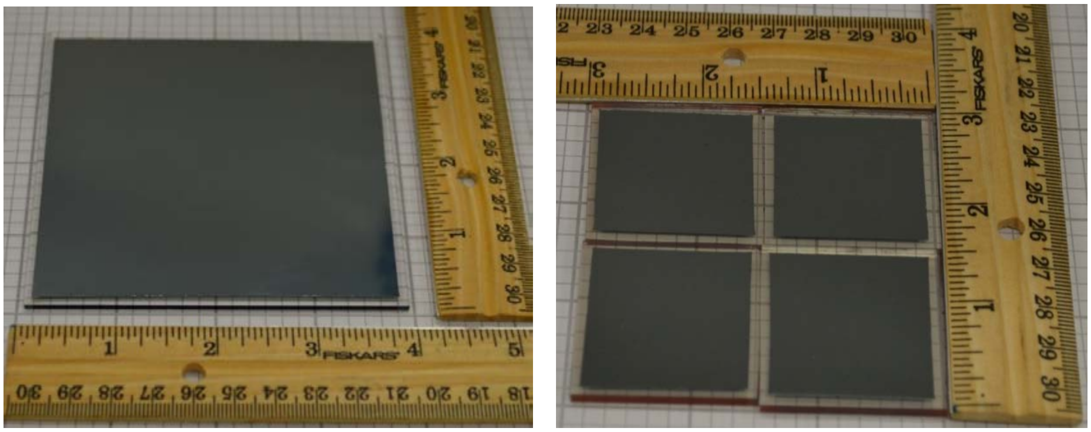

(a) (b)

Figure 2.9. Enriched ^{10}B-doped a-Se (As, Cl) thin films deposited on ITO coated glass substrates: (a) 10 × 10 cm^2 (4 × 4 sq. inches) films of ~ 300 μm and (b) 4 × 4 cm^2 (~1.5 × 1.5 sq. inches) sister films (deposited in one single deposition run).

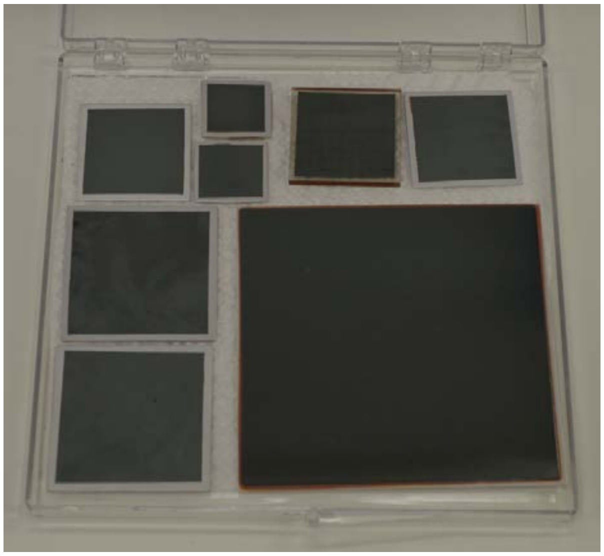

Figure 2.10. Enriched ^{10}B-doped a-Se (As, Cl) thin films deposited on Al/Al$_2$O$_3$ substrates (4 × 4, 2 × 2, 1.5 × 1.5, and 1 × 1 sq. inches) in a single deposition run grown in the modified evaporation system with larger mounting capabilities in the vacuum chamber.

2.5 ALLOY FILM CHARACTERIZATION

2.5.1 Surface Morphology Studies

The surface morphology and microstructure of the deposited B-doped a-Se (As, Cl) alloy films were examined by scanning electron microscopy (SEM) studies with different magnifications. In SEM, beam of electrons are focused on the sample, and electromagnets rather than lenses are used for focusing, so much higher resolution could be obtained. The electron beam interacts with sample atoms, producing various signals that are collected to produce SEM image. Figure 2.11 (a) shows SEM images of the surfaces of grown alloy films. The picture at left shows very smooth and shiny surfaces without any micro-cracks or defects (even with1000 x magnification). The SEM picture at right shows a few typical defects sometimes encountered with thin film deposition cycle. The alloy films with defect-free smooth surface morphology were used to fabricate neutron detectors. Figure 2.12 (a) shows a typical SEM image taken at the edge of the ^{10}B-doped a-Se (As, Cl) alloy film on ITO-coated glass substrates.

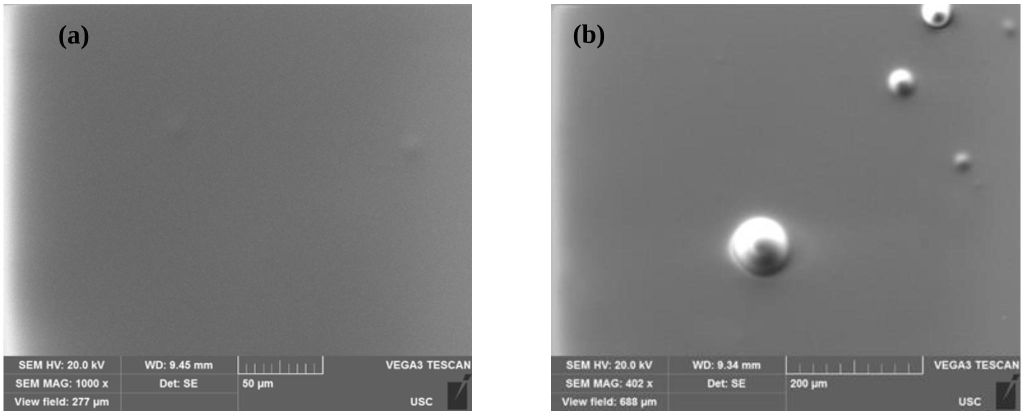

Figure 2.11. SEM images of doped ^{10}B doped a-Se (As, Cl) alloy films deposited on ITO-glass substrates: (a) showing smooth surface, 1000× magnification; (b) showing a few surface defects, 400 × magnification.

2.5.2 Compositional Characterization

Energy-dispersive x-ray spectroscopy (EDAX) is an important tool to determine elemental composition of a material. Performed within a SEM setup, in this technique, high-energy electrons from SEM beam excite and expel inner-shell electrons within the sample atoms. As electrons from the outer shell fill the holes created by the excited inner-shell electrons, x-rays are generated. The energies of these x-rays are distinctive of the elemental atom and contribute to the characteristic peaks on the EDAX spectra. The element concentration is determined by integration of the peaks corresponding to the major elements present [39]. Figure 2.12 (b) presents an EDAX line scan showing the elemental concentration along the edge of the ^{10}B-doped a-Se (As, Cl) alloy film on ITO-coated glass substrates. The EDAX scan shows the presence of Sn, O, and In of sodalime glass (SLG) at the substrate side. Presence of Se and As is observed across the alloy film; however, counts of Cl are very small probably due to Cl concentration in ppm level. Boron count is not observed because of low atomic mass; for that inductively coupled plasma mass spectroscopy (ICP-MS) was performed.

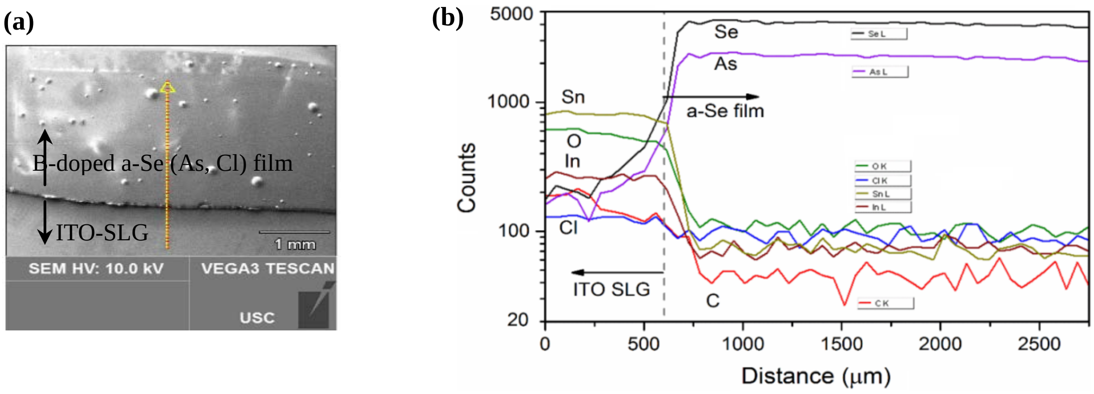

Figure 2.12. (a) SEM image taken at the edge of the B-doped a-Se (As, Cl) alloy film on ITO-coated glass substrates, and (b) EDAX line scan showing the elemental concentration along the yellow arrow shown in (a).

2.5.3 Structural Characterization by XRD

Amorphous structure of selenium alloys was confirmed by x-ray diffraction (XRD) analysis. In order to get a diffraction pattern, the ground a-Se powder is bombarded with x-rays. When these x-rays interact with the material they either get diffracted or transmitted. Because of unique physical properties like composition, lattice spacing and arrangement, the incoming beam gets diffracted at characteristic angles. Intensity versus angle plot is measured to determine the corresponding material. The x-ray diffraction pattern was obtained using a Rigaku D/MAX 2100 powder x-ray diffractometer (CuK_{α} radiation, $\lambda = 0.15406$ nm). The observed diffraction patterns shown in Figure 2.13 corresponded very well to the standard x-ray pattern for Se alloys with an amorphous structure. There are no diffraction peaks for any crystallographic orientation observed in the literature [40]. No other peaks due to impurities or any other phases were observed within the sensitivity of the instrument (0.1%). Hence the XRD confirms the amorphous structure of the stabilized a-Se (As 0.52%, Cl 5 ppm) alloy. For detector applications, maintaining amorphous structure is important because the resistivity decreases by orders of magnitude if the alloys are polycrystalline.

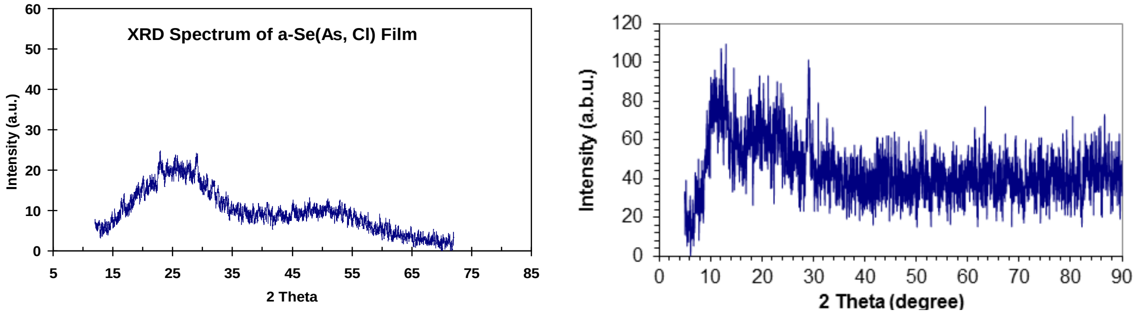

Figure 2.13. XRD patterns showing amorphous structure of (a) a-Se (As, Cl) alloy film and (b) B-doped a-Se (As, Cl) film on ITO-coated glass substrates.

2.5.4 Optical Absorption Study

The optical absorption studies were conducted on B-doped a-Se (As, Cl) alloy films on ITO glass substrate to determine the bandgap energy. Large bandgap energy ($\geq$ 1.5 eV) is required for high resolution detectors so that the detection signal is due to the ionization by radiation only and not due to thermal noise. The relationship between indirect band gap energy, E_g, and absorption coefficient, α, as a function of the photon energy, $h\nu$, could be expressed the following equations:

$$(\alpha h\nu) \propto \left(h\nu - E_g\right)^{1/2} \qquad 2.3$$

$$or, \quad (\alpha h\nu)^{2} = B.h\nu - E_g \qquad 2.4$$

where h is Planck's constant, ν is the frequency of light, and B is a constant. By plotting optical absorption ($\alpha h\nu$) vs. incident photon energy ($h\nu$) the bandgap energy could be determined. Figure 2.14 shows such optical absorption curve obtained for B-doped a-Se (As, Cl) alloy film.

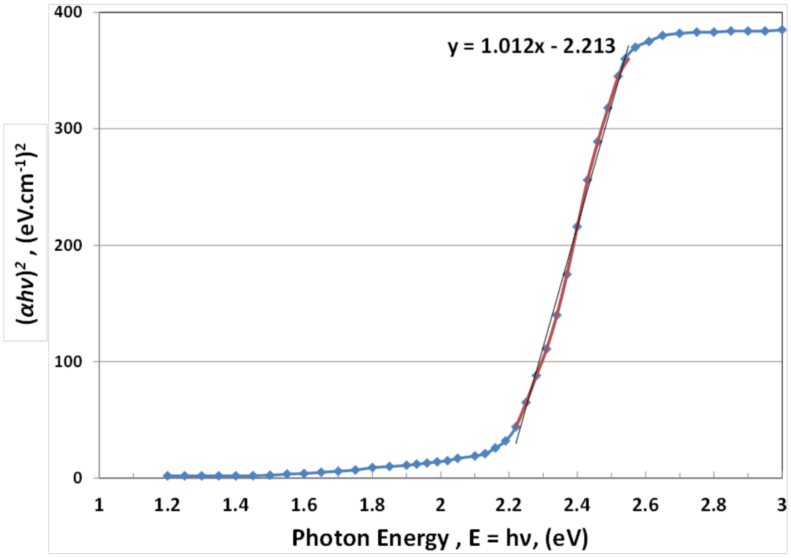

Figure 2.14. Optical absorption spectra of B-doped a-Se (As, Cl) alloy film.

An ITO coated glass slide was used as the reference, and the values of α were not corrected for the reflection of the alloy film surface. By extrapolating the linear region of the curves to $(\alpha h\upsilon)^2 = 0$ [41], the bandgap energy (E_g) was estimated to be about 2.21 eV at 300 K which is in close agreement with other a-Se based alloys as reported in the literature [16, 31].

2.6 BORON-DOPED A-SE DETECTOR FABRICATION

A planar metal-semiconductor-metal (MSM) structure (see Figure 2.1) was used to create boron- doped a-Se (As, Cl) alloy film based neutron detectors. Using the deposited a-Se (^{10}B, As, Cl) films, devices with two different contact structures were fabricated:

Detector Structure (1): Au /a-Se (^{10}B, As, Cl)/ Glass/ITO

Detector Structure (2): Au /a-Se (^{10}B, As, Cl)/ Al_2O_3/Al

Different contact structures were studied to reduce the leakage current of the device by controlling carrier transport inside the devices for better detection signals. In order to obtain a relatively low leakage current, a thin blocking layer (electron blocking) is necessary at the interface between the B-doped Se alloy film and the ITO-glass or aluminum substrate bottom contact. This was achieved for aluminum substrate using Al/Al_2O_3 layers as an electron blocking layer in the device (structures #2). The aluminum oxide layer prevents dark current injection from the substrate. Al substrates were oxidized by heating at 220 °C for about two hours. The top free surface of B-doped a-Se (As, Cl) layer normally acts as a blocking layer for holes preventing injection of surface charges into the bulk.

Gold top contacts were deposited on the top of the alloy films by using metallization shadow mask technique. Semitransparent gold contact of thickness ~10 nm was deposited by RF/DC sputtering unit (Figure 2.15). The bottom contact was oxidized aluminum /aluminum (Al_2O_3/Al) or ITO. Thin copper wires were attached with silver epoxy and the contact area was encapsulated with very thin epoxy adhesives. Fabricated detectors of different sizes and bottom contacts are shown in Figure 2.16.

Figure 2.15. RF/DC 13.56 MHz frequency sputtering unit used for metallization.

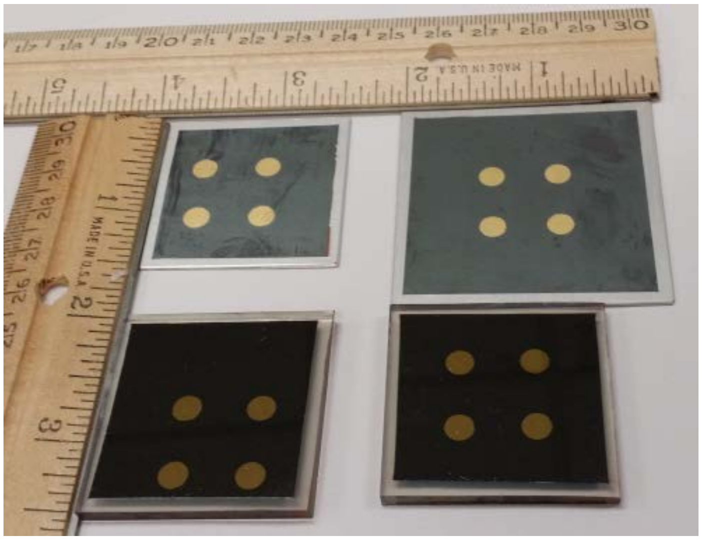

Figure 2.16. Enriched ^{10}B-doped a-Se (As, Cl) alloy film devices with 2 × 2 monolithic arrays - 1.5″×1.5″ and 2″×2″ on Al/Al_2O_3 substrates (top) and 1.5″×1.5″ on ITO coated glass (bottom); gold top contact with individual pixel size of ~ 0.78 cm^2.

2.7 ELECTRICAL CHARACTERIZATION OF B-DOPED A-SE DETECTORS

B-doped a-Se (As, Cl) alloy film must have high resistivity, which will reduce the leakage current flowing through the detector under high bias conditions. For high resolution detectors, it is crucial to maintain the leakage (dark) current at very low levels of ~10^{-10} – 10^{-12} A, when biased. Thus current-voltage (I-V) studies using metal-semiconductor junction is used for electrical characterization to determine the leakage current of the fabricated alloy film detectors and then calculate the resistivity.

The current-voltage characteristic (I-V characteristic) of a metal-semiconductor junction is determined by the barrier height at the interface. There are two types of metal-semiconductor junctions: (i) Ohmic contact which has no barrier, allowing holes and electrons to travel through the semiconductor without being blocked and thereby producing a linear current-voltage response; (ii) Schottky contact is a rectifying contact which has potential barrier height at the interface restricting carrier movements. Schottky barrier offers easy current flow in the forward direction and little current flow in the reverse direction, current flows mainly in one direction. The barrier height (ϕ_{bi}) at the metal-semiconductor interface is the difference between metal work function (ϕ_m) and semiconductor work function (ϕ_s):

$$\phi_{bi} = \phi_s - \phi_m \tag{2.5}$$

Figure 2.17 shows band diagrams of Ohmic and Schottky contacts between a metal and a p-type semiconductor at thermal equilibrium. The work function is characterized by the energy required to remove an electron from the Fermi level (E_F) to the vacuum level. Once the metal-semiconductor junction is formed, the metal and the semiconductor Fermi levels get by exchanging charges at the edges of the bands. The energy band diagrams shows that there is no barrier blocks to halt the flow of holes in the case of Ohmic contact between metal and p-type semiconductor. Hence the current can flow through the junction regardless of the polarity of the applied voltage. The rectifying effect of the Schottky contact is due to the formation of this barrier height (ϕ_{bi}) at the junction.

The condition to form an Ohmic contact with a p-type semiconductor is that the metal must have higher work function compared to that of the p-type semiconductor ($\phi_m > \phi_s$). On the other hand a Schottky contact will be formed if $\phi_m < \phi_s$ [42]. The work function of amorphous selenium is ~5.9 eV. The work function of gold (Au) is 5.1eV, which is less than that of a-Se. Hence, gold top contact formed Schottky contact with a-Se in the fabricated ^{10}B-doped a-Se (As, Cl) detectors.

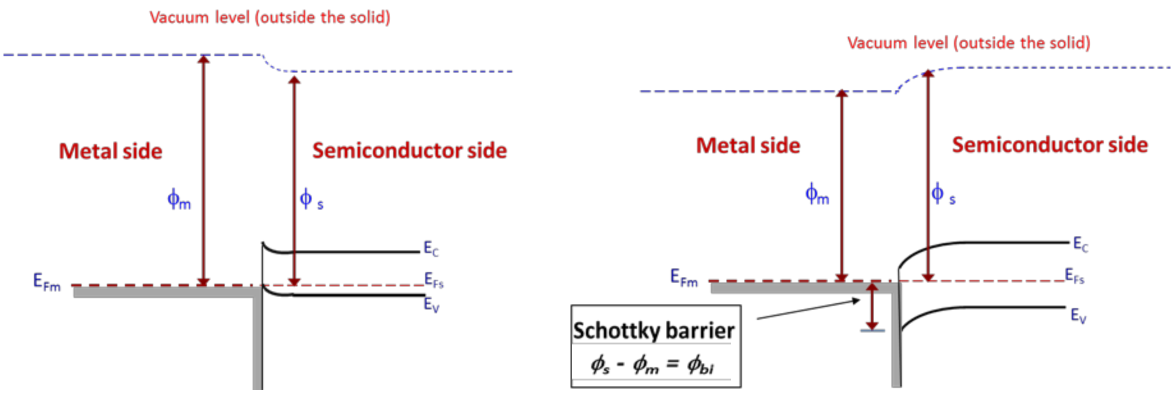

p-type Ohmic contact

p-type Schottky contact

Figure 2.17. Band diagrams of Ohmic and Schottky contacts between a metal and a p-type semiconductor at thermal equilibrium energy.

Current-voltage (I-V) characteristics were carried out by measuring the current flowing through the a-Se detector at various applied voltages across the detector. The electrical resistance was measured from inverse slope of the linear regression of dark current-voltage curve. The resistivity was calculated using the equation:

$$\rho = R \cdot \frac{A}{L} \qquad 2.6$$

where ρ is the resistivity of the crystal in Ohm-cm, R is the resistance in Ohms, A is the contact area (cm^2), and L is the thickness of the a-Se film. I-V measurement was carried out using Keithley 237 source measure unit.

Figure 2.18 shows the current-voltage (I-V) characteristic of enriched ^{10}B-doped a-Se (B, As, Cl) detector with top gold contacts and ITO glass or oxidized Al as bottom contact. The detector on ITO glass substrate (Figure 2.18 (b)) indicates low leakage current (~-10 nA at -1000V), and high rectification ratio showing typical diode characteristic. Figure 2.18 (c) shows I-V characteristic of a detector fabricated on Al substrate with Al_2O_3 interfacial layer as electron blocking layer. The measured leakage current for these detectors were in the range of pA (pico-amp) to a fraction of few nA at -1000V. The low leakage current at a very high bias is beneficial for detector performance because higher electric field can be applied to the detector without increasing noise and that will enhance the signal from a detector. The devices with Al_2O_3 electron blocking layer showed two to three orders of magnitude higher resistivity compared with the devices without an electron blocking layer. The resistivity the ^{10}B-doped a-Se (B, As, Cl) detector measured to be $\geq 10^{12}$ Ω-·cm for the gold top electrode and the aluminum oxide and aluminum bottom electrode devices. This is a promising result, which can further improve the performance of a-Se (B, As, Cl) alloy detectors by reducing leakage current significantly.

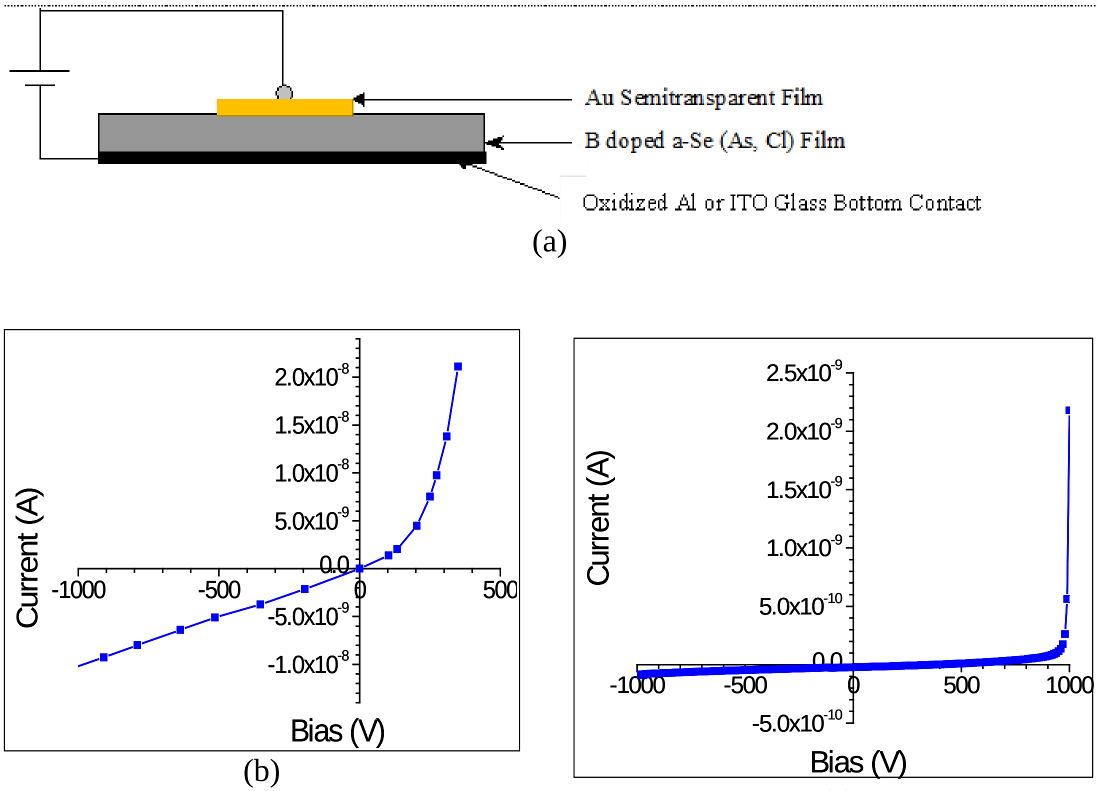

(a)

(b)

(c)

Figure 2.18. (a) Schematic of enriched ^{10}B-doped a-Se (B, As, Cl) planar MSM detector; (b) Current-voltage (I-V) characteristic of such detector fabricated on ITO glass; and (c) I-V characteristics of detector fabricated on oxidized Al substrate with Al_2O_3 as blocking contact.

2.8 Metal Contact Studies for Schottky Devices

For high resolution detectors, it is crucial to maintain the low dark (leakage) current levels (~10^{-10} – 10^{-12} A) under high bias conditions. The choice of metal used for the top contact on metal/a-Se/metal sandwich structures plays a critical role in this matter. While obtaining high Schottky barrier heights might become an issue on p-type semiconductors, the high work function of amorphous selenium (ϕ_{Se} ~5.9 eV) makes this goal cumbersome to achieve by using metals with low ϕ_m values. However the complex physical properties of a-Se and unpredictable metal/a-Se junction mechanisms make it very challenging to control the leakage current by solely controlling the barrier height. Therefore optimum contacts were determined by experimenting with a set of various metals as top contacts.

The voltage dependent junction current in a Schottky contact can be expressed as:

$$I = I_s(e^{\frac{\beta V}{n}} - 1) \qquad 2.7$$

where I_S is the saturation current, V is the applied voltage, n is the diode ideality factor, $\beta = q/k_B T$, q being the electronic charge (1.6 × 10^{-19} C), k_B the Boltzmann constant (8.62 × 10^{-5} eV/K), and T is the absolute temperature (°K). The saturation current is given by:

$$I_S = A^* A T^2 \left(e^{-\beta \varphi_B}\right) \qquad 2.8$$

where A is the area of the diode, φ_B is the Schottky barrier height, and A^* is the effective Richardson constant which can be expressed as:

$$A^* = 4\pi^2 \ m^*/h^3 = 120 \ (m^*/m) \ Acm^{-2} \, K^{-2} \qquad 2.9$$

where h is Planck constant, and m* is the electron effective mass [42].

Using logarithm, the Equation 2.7 could be written as:

$$log(I) = \frac{\beta V}{n} + log(I_s) \qquad 2.10$$

Using current measurements at varying applied voltage and then plotting log(I) versus applied voltage bias, we could measure the ideality factor 'n' from the slope and saturation current I_s from the intercept. Figure 2.19 shows a typical such plot.

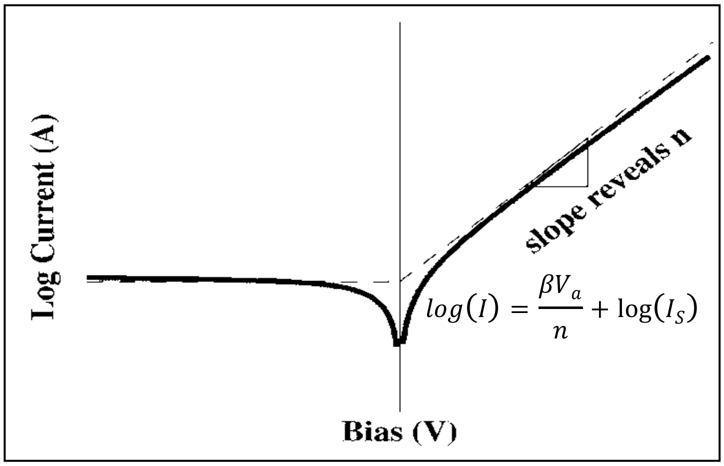

Figure 2.19. Plot of semi log I vs V of I-V curve of Schottky contacts.

The junction properties between B-doped a-Se (As, Cl) alloy films and a wide variety of metals with different work functions (Au, Ni, W, Pd) were investigated using current-voltage measurements. The aim was to investigate whether the choice of metal can improve the performance of the detector by minimizing the dark leakage current. For the top metal contacts, we have found significant dependencies of metal work functions on current transients following application of voltages from - 800 to 1000 volts. By evaluating the barrier height dependency on the metal work function, we were able to estimate the space charge densities by using time of flight (TOF) measurements.

Monolithic 3 × 3 arrays of metal contacts (M-S-M devices) for contact studies are presented in Figure 2.20. Thin films of various metals were deposited on top of ^{10}B-doped a-Se (As, Cl) alloy film to form the front contact. Metal deposition has been carried out by RF/DC 13.56 MHz frequency sputtering unit in argon ambient. Current-voltage (I-V) characteristics of various metals contacts were carried out and are shown in Figure 2.21. Among the four metal contacts tested, Au contacts showed best diode characteristics with high rectification. I-V characteristics in general showed very low leakage currents in the reverse biases as well as forward biases. All metal contacts showed low dark currents under very high bias and leakage current pass beyond nA levels. The performances of Ni and W contacts showed lowest leakage currents (~ 10^{-11} A at - 800V). Forward bias voltage degradations were observed for some contacts especially with Ni and Pd contacts. Further investigation is going on to investigate time dependence of the current transients under high bias by exposing the detector at a constant positive bias for 10-12 hours and measuring diode current.

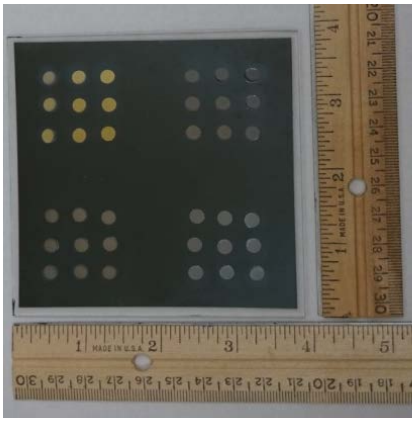

Metal	Work functions, ϕ_m (eV)
Au	5.1
Ni	5.15
W	4.55
Pd	5.12

Figure 2.20. Metal contacts (monolithic 3 × 3 arrays) on 10 x 10 cm^2 (4 × 4 sq. inches) ^{10}B-doped Se (As, Cl) detector fabricated on Al/Al_2O_3 substrate. Upper left: gold (Au); upper right: nickel (Ni); lower left: tungsten (W); and lower right: palladium (Pd).

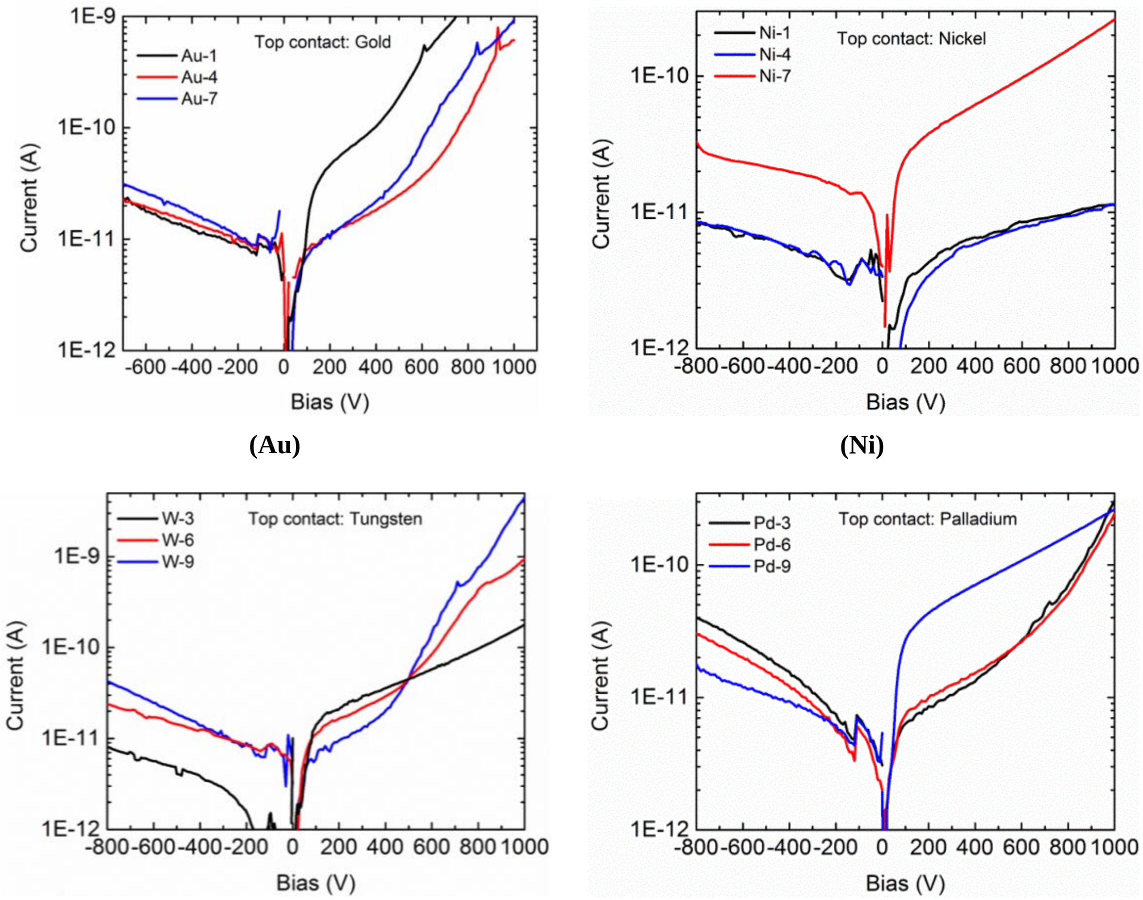

(Au) **(Ni)**

(W) **(Pd)**

Figure 2.21. Current-voltage characteristics of various metals contacts of monolithic arrays in Figure 2.20; very low leakage currents were seen for all of these metal contacts.

2.9 NUCLEAR RADIATION TESTING OF B-DOPED A-SE DETECTORS

Thermal neutrons when are captured by ^{10}B nucleus undergo an (n, α) nuclear reaction, producing two daughter particles (^{7}Li and α) as shown in Figure 2.22. The released 2.79 MeV kinetic energy is shared by these two charged particles traveling in opposite directions (energy of ^{7}Li = 1.014 MeV and E_α = 1.78 MeV). The kinetic energy of the charged particles excites electrons in a-Se atoms into the conduction band and subsequently generates holes in the valence band. Generated electron-hole pair is free to travel to their respective electrodes under an electric field across the a-Se film, producing a measurable electrical current. The resulting signal pulse indicates the occurrence of a thermal neutron capture event. These signals are then transformed into radiation spectrum by using standard nuclear instrumentation consist of preamplifiers, shaping amplifier, and multi-channel analyzers (MCA).

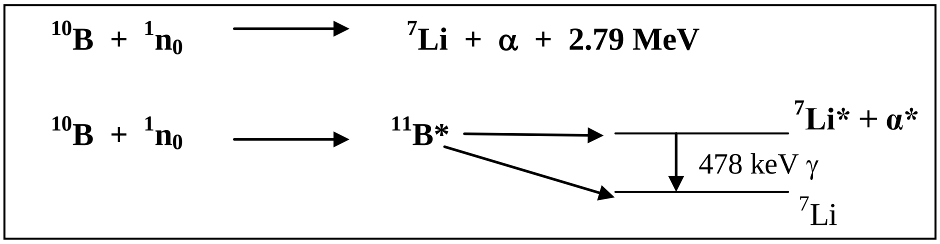

Figure 2.22. The ^{10}B (n, α) ^{7}Li reaction upon neutron capture by ^{10}B nucleus.

Figure 2.23 shows the schematic diagram of the detection testing setup. A preamplifier allows the charge signal to be converted to a voltage signal, which can be sent over standard BNC cables to a shaping amplifier. Preamplification is a critical component, because noise introduced in this stage of the detection setup can have a significant effect on the resulting detection spectrum. The preamplifier pulse output is shaped by the shaping amplifier, which will filter as much noise as possible while preserving information about the energy of the radiation countered by the detector. The shaping amplifier spends a certain amount of time measuring the signal, which is known as the shaping time. After shaping, the amplified pulses are sent to a multi-channel analyzer (MCA). The MCA converts the analog signals into digital information containing the height of the shaped pulse (the "pulse height"), and record the number of pulse heights acquired within a given range. The resulting histogram, produced by the

MCA is called “Pulse Height Spectrum” (PHS), which depicts how many counts of radioactive photons interacted with the detector in a given energy window.

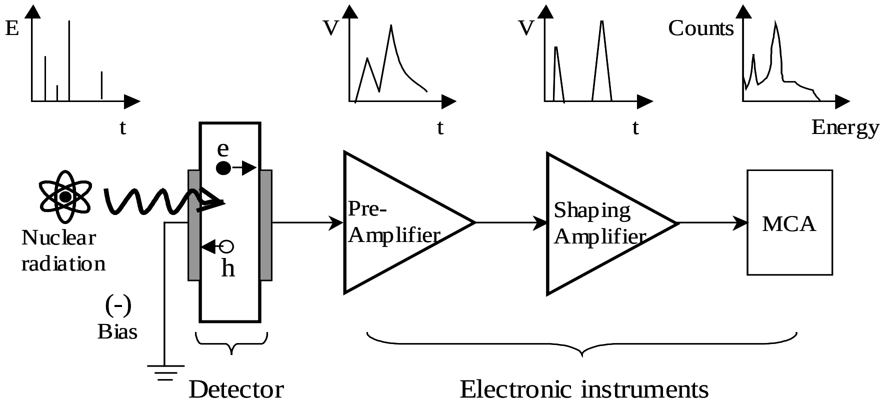

Figure 2.23. Schematic of the detector testing electronics.

The response of the detectors to the nuclear particles was evaluated by irradiating the detector with nuclear radiation sources and by recording the pulse height spectrum (PHS) produced from the detector. The bias to the detector was applied using a Canberra 3102D high voltage power supply. The charge signals generated by the interaction of the nuclear particles with the detector were amplified with a Princeton Gamma-Tech RG-11B/C-RT preamplifier, and a Canberra 2022 linear amplifier. The amplified signal was then fed into a Canberra Multiport II multichannel analyzer and evaluated using Genie-2000 software.

Response of the fabricated ^{10}B-doped a-Se (As, Cl) alloy detectors to nuclear radiation was first evaluated by irradiating the detector with 0.1 mCi ^{241}Am source (peak energies: 60 keV for γ and 5.5 MeV for α particles) at room temperature (~300 K). Alpha particles were used as surrogates for neutrons since ^{10}B neutron capture reaction directly produces α-particle (Figure 2.22). Figure 2.24 shows the pulse height spectrum produced by the detector with ^{241}Am radiation source. This spectrum completely vanishes and counts become background noises when a piece A4 white copying paper was placed in between the radiation source and detector, confirming the detector's response to alpha particles. By comparing response with gamma radiation, it is clear that the peak is distinctive signal of α-radiation.

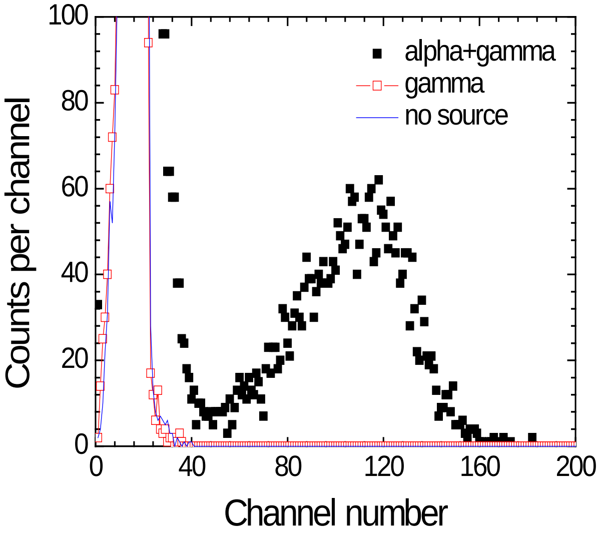

~0.1 mCi ^{241}Am source

Bias: - 1000V,
Coarse gain: 30,
Fine gain: 3-00,
Shaping time: 2 μs,
Acquisition time: 120 s)

Figure 2.24. Pulse height spectra of B-doped Se alloy detector under ^{241}Am source (strong source). No detection peak was observed with A4 bond paper, blocking the α-source. By comparing response with gamma radiation, it is clear that the peak is distinctive signal of α-radiation.

Finally, neutron response of the fabricated ^{10}B-doped a-Se (As, Cl) alloy detectors was evaluated by irradiating the detector with a californium-252 source (0.7 μCi ^{252}Cf) at 300 K. A stack of four 0.25″ high-density polyethylene (HDPE) moderator was placed ~ 3 cm from the ^{252}Cf source to convert fast neutrons emitted from the source to thermal neutrons [43]. Figure 2.25 shows the pictures of the neutron source vault and the detection setup. Figure 2.26 shows the pulse height spectrum produced by the detector under thermal neutrons form ^{252}Cf neutron source moderated by HDPE at various bias voltages. The measured pulse-height spectra under thermal neutron irradiation show very well resolved peaks corresponding to the product energies of ^{10}B and thermal neutron reaction described in Figure 2.22. Figure 2.26 shows that the peak position shifted to higher energies (represented by higher channel) with higher applied voltages. This is due to greater collection efficiency since charges are more quickly separated and swept to the collecting electrodes under higher voltage bias applied to the detector.

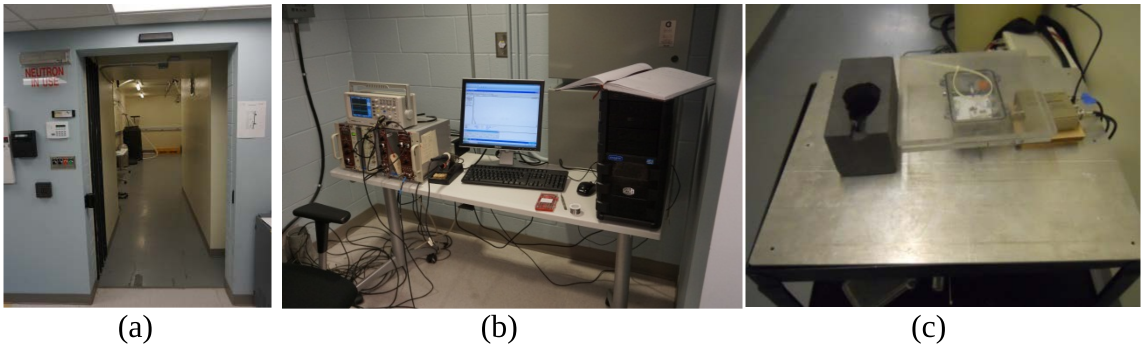

(a) (b) (c)

Figure 2.25. (a) Picture of a neutron vault; (b) Picture of a detection system located outside of the neutron source vault chamber; (Middle) (Right) Detector electronics and sample box is within the neutron vault chamber and are placed below the 0.7 μCi ^{252}Cf source and with HDPE moderator during measurements.

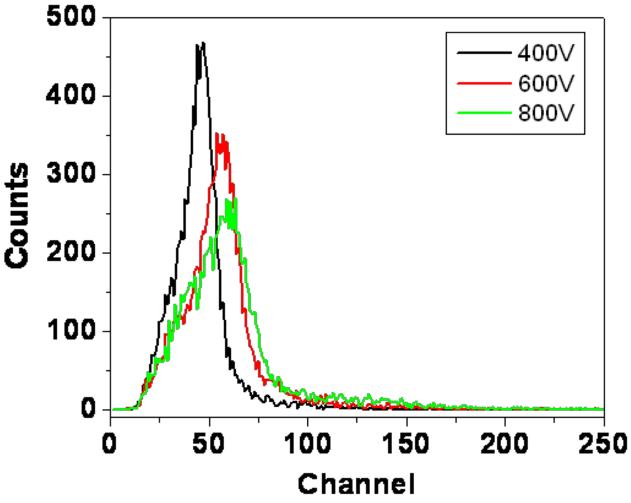

~0.7 μCi ^{252}Cf source

Coarse gain: 30,
Fine gain: 3,
Shaping time: 0.5 μs,
Acquisition time: 60 s)

Figure 2.26. Detection spectra of ^{10}B-doped Se (As, Cl) alloy detector under 0.7 μCi ^{252}Cf neutron source and with a stack of four 0.25” HDPE moderators. As expected the peak shifted to higher energies due to greater collection efficiency with higher applied voltages.

2.10 CONCLUSION

Direct read-out solid-sate thermal neutron detectors have been fabricated from enriched ^{10}B-doped a-Se (As, Cl) alloy films. Alloy composition was stabilized and optimized using As and Cl doping to Se precursor, which was zone refined to increase purity to ~7N in order to minimize deterioration in charge carrier transport and collection efficiency due to impurities. Characterizations carried out with scanning electron microscopy (SEM), x-ray diffraction (XRD), glow discharge mass spectroscopy (GDMS), optical absorption study, current-voltage (I-V) measurements, measured stoichiometry, morphology, bandgap energy, resistivity, and dark leakage current. The bandgap and resistivity was determined to be 2.21 eV and $\geq 10^{12}$ Ω-cm, respectively, at 300K. I-V characteristics showed very low leakage (~-10nA at -1000V); by using Al_2O_3 as blocking layer, leakage current is reduced to pA to a fraction of nA at -1000V. Metal-semiconductor-metal (MSM) detectors were fabricated with up to 4″×4″ alloy films with thickness up to 300 μm. The detectors demonstrated distinctive pulse-height spectra when irradiated by ^{241}Am α-source and ^{252}Cf neutron source moderated by HDPE stack, which was reduced to background noise when the sources were blocked or removed. These data are very encouraging and corresponds very well with the requirements of ideal semiconductor properties for application in neutron radiation detection. The data confirms that ^{10}B-doped a-Se (As, Cl) alloy films can be used to construct high performance compact neutron detectors.

CHAPTER 3: CZT GAMMA-RAY DETECTORS

3.1 OVERVIEW

Cadmium zinc telluride (CZT) is a direct-bandgap ternary semiconductor grown by alloying binary compound cadmium telluride (CdTe) with zinc (Zn). The ratio of Cd:Zn is commonly 90%:10% for detector grade CZT crystals [9]. CdTe has cubic lattice structure; after alloying with Zn, 10% of the Cd atoms are replaced with Zn atoms to form the ternary lattice structure of $Cd_{0.9}Zn_{0.1}Te$ (henceforth known as CZT). Varying the concentration, x, of zinc present in the $Cd_{1-x}Zn_xTe$, the bandgap energy of CZT can be adjusted from 1.5 to 2.2 eV. CZT has many favorable properties for gamma-ray and x-ray detectors, and years of research show its effectiveness [9, 44, 45, 46, 47]. Its wide bandgap (>1.5 eV at 300 K) offers room temperature operation, high atomic numbers (Cd = 48, Te = 52) and high density (5.8 g/cm^3) enables absorption of high energy gamma ray, high resistivity (10^{10} Ω-cm) reduces the effect of thermal noise, and good electron mobility (1100 cm^2/Vs) represents decent charge collection to generate readout spectra. Thus, CZT is one of the most promising room temperature radiation detector and can be used for a variety of optoelectronic devices and applications such as x- and gamma radiation spectroscopy for detection of dirty bomb or special nuclear materials (SNMs) to combat security threat, nondestructive testing for industrial process monitoring and control, for medical imaging using nuclear medicine such as in positron emission tomography (PET), and space astronomy for NASA application.

The following sections provide experimental procedures, theoretical background as needed, results and discussion on the research work carried out on CZT. Details of the CZT single crystal growth by tellurium solvent method, morphological, optical and electrical characterization of grown CZT crystals, surface processing, nuclear radiation detector fabrication, and testing of these devices are presented. First, elemental precursors (Cd, Zn, and Te) were purified using multi-pass zone purification method. Zone-refined precursor materials were then employed to grow CZT single crystal, by solvent-growth method [48]. Semiconductor characterization was then performed on the CZT crystals to determine crystal morphology, elemental stoichiometry, band gap, and electrical resistivity [49, 50]. Deep-levels and surface defect studies were conducted to determine the type and concentration of defects present in the crystals and the defect levels are correlated with detector performance [49, 50].

CZT nuclear detectors were fabricated using in-house grown materials. Two different types of detector structures were investigated. First, planner detector was tested where both charge carriers, electrons and holes, generate electrical signals in the readout system [48, 50, 51]. Second, detector structure with guard ring was studied where only single carrier (electron only which has much higher mobility) will be responsible for readout spectra. This is carried out to compensate for the poor hole mobility. Electrical characterization was performed to determine the charge transport properties. Pulse height spectroscopy measurements were carried out using a ^{241}Am (59.6 keV) and ^{137}Cs (662 keV) radiation sources on CZT radiation detectors. Finally, detectors were characterized using analog and digital radiation detection systems to measure their performance and energy resolutions [48, 49, 50, 51, 52].

3.2 CZT CRYSTAL GROWTH

This section describes zone purification of precursor materials (Cd, Zn, and Te), preparation and carbon coating of growth ampoules, and details of the CZT single crystal growth by solvent growth method.

3.2.1 Precursor Purification by Zone Refining Method

Since material impurities have a very strong negative impact on device performance [44, 45], it is imperative that very high purity precursor materials are used for growth of semiconductor crystals. The highest purity that is readily commercially available for elemental precursors of CZT (cadmium, zinc, and tellurium) is 5N (or 99.999% pure). Therefore further purifications of these precursors were carried out using in-house multi-pass horizontal zone refining system. The existing set-up consists of a computerized process controller, a data acquisition system, and all safety features. An automated zone refiner was custom fabricated to work round the clock in programmable mode. A photograph of a zone refiner is shown in Figure 3.1. Details of how the zone refining system works have been provided in Chapter 2, Section 2.3.1.

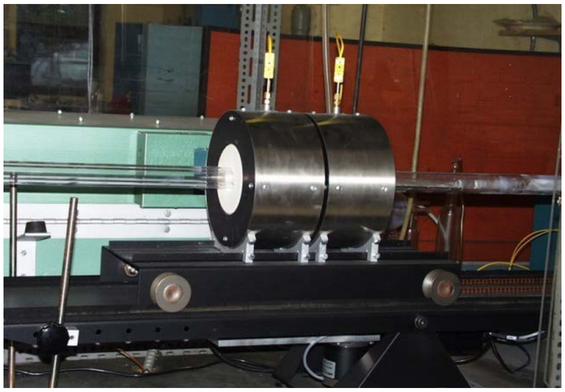

Figure 3.1. A photograph of a horizontal, two-heater zone refining system.

For zone refining, the quartz tubes used (length = 60 cm, OD = 28 mm, and ID = 25 mm) were manufactured by Quartz Scientific, Inc. The quartz tube was first closed at one end to make an open ampoule. The open ampoule was thoroughly cleaned using successive washes with acetone, methanol, 10% HF aqueous solution and de-ionized (DI) water (18 MΩ) and then baked overnight at ~ 1000 °C under a constant nitrogen flow (~0.25 liter/min). The cleaned and dry quartz ampoule was filled up to first 18″ of the length with individual precursor feed material (~500 grams Cd, Zn, or Te of 5N purity), sealed and then suspended over the track actuator in the horizontal zone refining furnace. The furnace temperature was slowly ramped up (at a rate of 1 °C per minute) to a temperature which is slightly above the melting point of the precursor material. The melting points of precursor materials Cd, Zn, and Te are 321.1°C, 419.6°C, and 449.5°C, respectively, at 1 atm pressure. The track actuator moved the furnace along the ampoule length at a rate of 30 mm per day, and the furnace made 40-45 passes from one end of the ampoule to the other.

The ring furnace melted a small zone of solid precursor material. When the heat source was removed, the melted precursor material re-solidifies, and due to solid-liquid phase transition, impurities got segregated from solid phase to the molten zone. As the furnace slowly moved along the ampoule, shifting the molten zone from one end to other, the expelled impurities got accumulated to the end of the ampoule. After multiple passes (typically 45 passes), most of the impurities were collected into one end of the ampoule, while the remainder of the material became highly pure. A photograph of a typical zone refined cadmium (Cd) ingot is shown in Figure 3.2, with impurities segregated to the left end of the ampoule, and pure precursor Cd material on the right side of the ampoule.

Figure 3.2. Zone refined (ZR) Cd ingot within a quartz ampoule; pure precursor material is on the right side while segregated impurities are on the left side of the ampoule.

After completion of the ZR process, the ampoule was cut and the zone-refined material was removed inside an argon-controlled glove box. Depending on uniformity of transparency, a length of ingot was considered 'pure' material, and cropped from the impure end of the ingot. The removed 'pure' precursor material was then stored in argon filled polyethylene bottles until they were ready to be used in the CZT crystal growth. Glow discharge mass spectroscopy (GDMS) analysis was performed on the zone refined (ZR) precursor materials (Cd, Zn, and Te) and compared with the pre-ZR data to evaluate the effectiveness of the ZR purification. Table 3.1 shows the results of the GDMS analysis performed on the zone-refined Cd, Zn, and Te materials. Samples were tested for 72 elements from Li to Pb. The relative error associated with the GDMS technique is reported to be about 20%. The GDMS data showed that zone refining process has segregated out a diverse array of impurity materials. The concentrations of the common elemental impurities in the zone-refined precursor Cd, Zn or Te material were 3-10 times less compared to samples before zone purification. For example, the concentration of Hg impurity in Cd decreased from 4.5 ppb to 0.3 ppb after zone purification.

Table 3.1. Impurity analysis of zone refined Cd, Zn, and Te materials by Glow Discharge Mass Spectroscopy (GDMS). Impurity concentration in parts per billion. Parenthesis data are after zone purification showing the effectiveness of zone refining process.

Impurity	**Cd**	**Zn**	**Te**
O	3.2 (≤ 0.5)	2.7 (< 0.4)	5.2 (< 0.6)
Na	1.6 (0.5)	1.4 (0.2)	1.8 (<0.4)
Sn	1.2 (< 0.5)	1.2 (< 0.2)	1.4 (< 0.2)
Al	2.8 (0.3)	1.5 (n/d)	1.8 (n/d)
Cd	Major	1.4 (0.3)	1.6 (0.3)
Li	4.2 (1.4)	4.8 (1.2)	2.4 (<0.3)
Mn	5.2 (1.5)	1.4 (<0.3)	1.2 (<0.3)
Hg	4.5 (0.3)	5.1 (<0.3)	4.2 (<0.3)
Ba	1.5 (<0.2)	0.8 (<0.2)	1.4 (<0.2)
Cr	1.4 (< 0.3)	2.4 (< 0.3)	1.5 (< 0.3)
Se	n/m	n/m	1.1 (<0.2)
Tl	1.6 (0.2)	2.6 (<0.3)	1.8 (<0.2)
Zn	1.4 (0.6)	Major	n/m
Pb	2.3 (n/d)	1.8 (n/d)	1.2 (n/d)
Te	4.5 (0.6)	0.8 (<0.1)	Major
Cu	4.1 (1.2)	2.2 (0.2)	1.4 (<0.3)
Pd	1.8 (<0.3)	1.6 (<0.2)	1.8 (<0.2)
Co	2.2 (<0.2)	1.8 (<0.4)	1.5 (<0.2)
Ni	3.2 (0.3)	1.8 (n/d)	1.2 (n/d)
Ca	5.2 (0.3)	0.6 (n/d)	0.4 (n/d)
Fe	0.5 (0.2)	0.4 (n/d)	0.6 (n/d)
Hg	4.2 (0.3)	4.2 (<0.5)	4.1 (<0.3)
Si	5.2 (1.6)	2.8 (0.6)	2.4 (1.2)

n/d – Not detected
n/m – Not measured

3.2.2 Carbon Coating of Growth Ampoule

The combination of the low melting point (321°C) with high thermal conductivity (0.9 $W/cm^{-1}K^{-1}$) and volume expansion on melting, makes Cd susceptible to adhere to the inside wall of the quartz ampoule and react with the SiO_2 material [53, 54]. This is one of the major issues with CZT crystal growth. To protect the precursor Cd material and the resulting CZT ingot from interaction with the quartz surface, as well as, to prevent wearing of the ampoule surface, the interior of the quartz ampoule were coated with thin layers of carbon. Carbon coating also prevents reaction of materials with a quartz ampoule. As carbon is a neutral impurity, it doesn't influence the electrical properties of the grown crystals. Any residual oxygen or water present within the quartz ampoule walls also got trapped in the carbon layer.

Prior to carbon coating, quartz ampoule was successively rinsed with acetone, methanol, and DI water. Next the ampoule was etched using 10% hydrofluoric acid, and rinsed with DI water several times. Ampoules were then loaded into the stainless steel encasement, and purged with argon for 15 minutes.

The quartz ampoule wall is coated with carbon by n-Hexane (HPLC grade, 95+%) vapors at about 850 °C within a furnace under argon flow. Figure 3.3 shows the schematic and picture of the carbon coating system developed in our laboratory, where several modifications were added to the basic systems described by Harrison et al. [54]. For example, a new housing for the quartz ampoules with our new design of stainless steel piping system was developed. This allows ampoules to be held within the coating system and once coated easily be removed to crystal growth furnace without harmful fumes escaping the encasement, as seen in the schematic in Figure 3.4 [55].

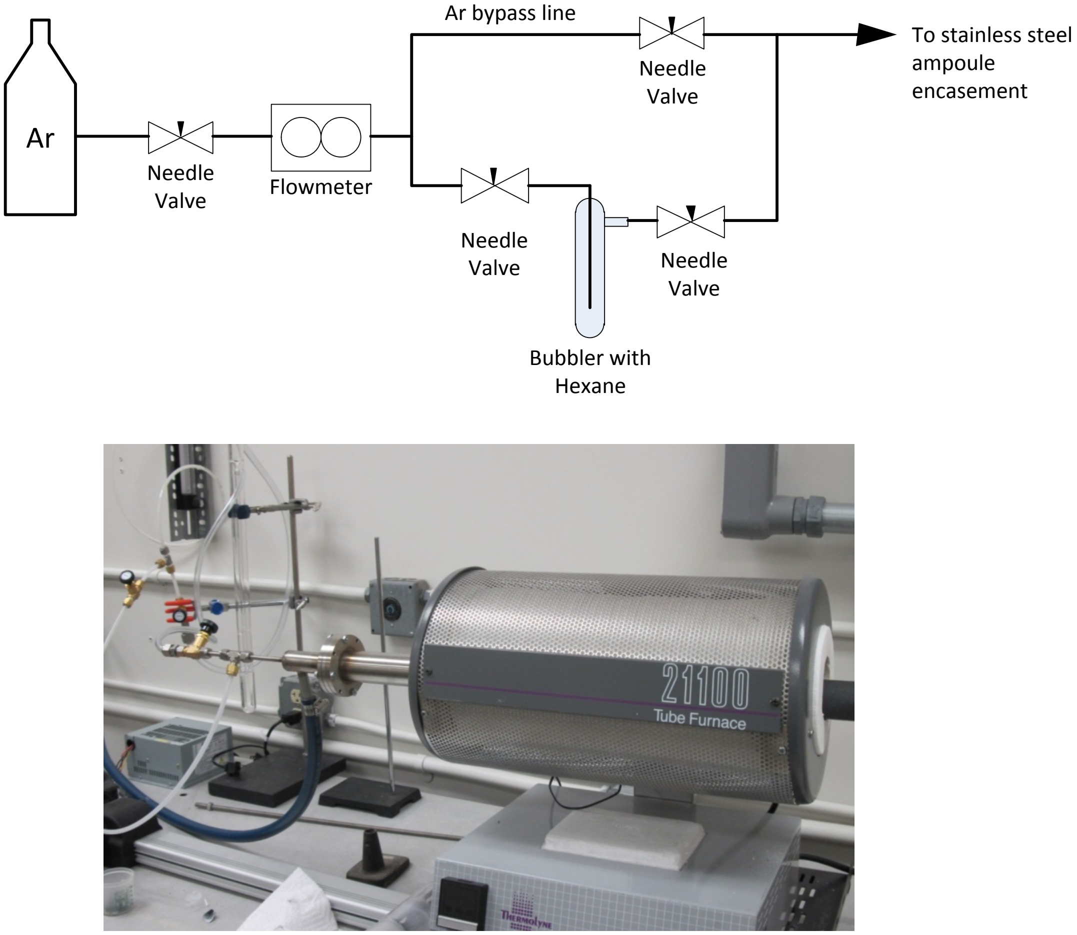

Figure 3.3. Schematic diagram (top) and a picture of carbon coating system developed in our laboratory for coating quartz ampoules (bottom).

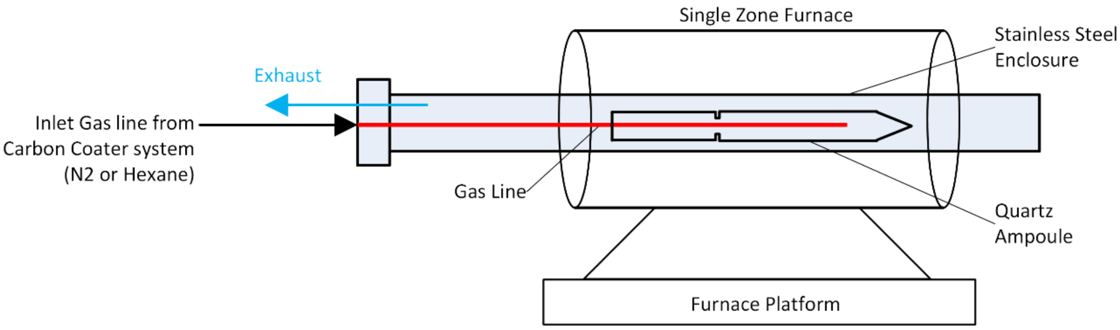

Figure 3.4. Schematic diagram of the furnace end of the in-house carbon coating system, showing the inlet, ampoule encasement, and exhaust for the system [56].

For carbon coating, the furnace temperature was ramped up to 850 °C at a rate of 1 °C per minute, under argon flow. After purging with argon for 15 minutes at 850 °C, argon flow through the normal hexane (n-hexane) bubbler is enabled. At a hexane flow rate of 15 mL/minute, it took about 1.5 hours to coat the inner wall of a 1″ diameter ampoule with 1 µm thick carbon layer. After coating, argon flow is resumed, and the ampoule is purged of hexane gas for 30 minutes. The carbon coated ampoule is then annealed at 1100 °C for 1 hour. Furnace temperature, time, bubble rate (by controlling argon gas pressure from the reading of a regulator), and location of the ampoule were changed to find the optimum conditions. For n-hexane, no carbon coating was observed below the furnace temperature of 800 °C at bubbling rate of ten bubbles/s. Carbon coating was formed at 850 °C. At <850 °C, the carbon film was delaminated and if the bubbling rate is not high enough. For good adhesion, we need a vigorous bubbling rate, which is over 10 in the regulator reading. We have observed that between acetone vs n-hexane: n-hexane is more efficient in pyrolysis reaction because it consumes less solvent for a carbon coating of similar quality. Figure 3.5 shows a picture of carbon coated 1″dia. quartz ampoules.

Figure 3.5. Picture of carbon coated quartz ampoules used for CZT crystal growth.

3.2.3 Single Crystal Growth Methods

Single crystal of CZT growth entails transformation of precursor materials from a liquid phase to the solid phase ternary CdZnTe compound in order to grow an ordered lattice structure. To form the covalent bonds in CZT compound that hold together the elements within the lattice structure, the growth temperature must be well above the melting point of the precursor elements as well as the compounds themselves (CdTe, ZnTe, and CZT). The melting points of precursor materials Cd, Zn, and Te are 321.1°C, 419.6°C, and 449.5°C, respectively, at 1 atm pressure. CdTe has a melting point of 1096°C for an atomic ratio of 50% Cd to 50% Te [53]. As seen on the ternary phase diagram shown in Figure 3.6, the melting point of $Cd_{0.9}Zn_{0.1}Te$ is ~1120 °C [57].

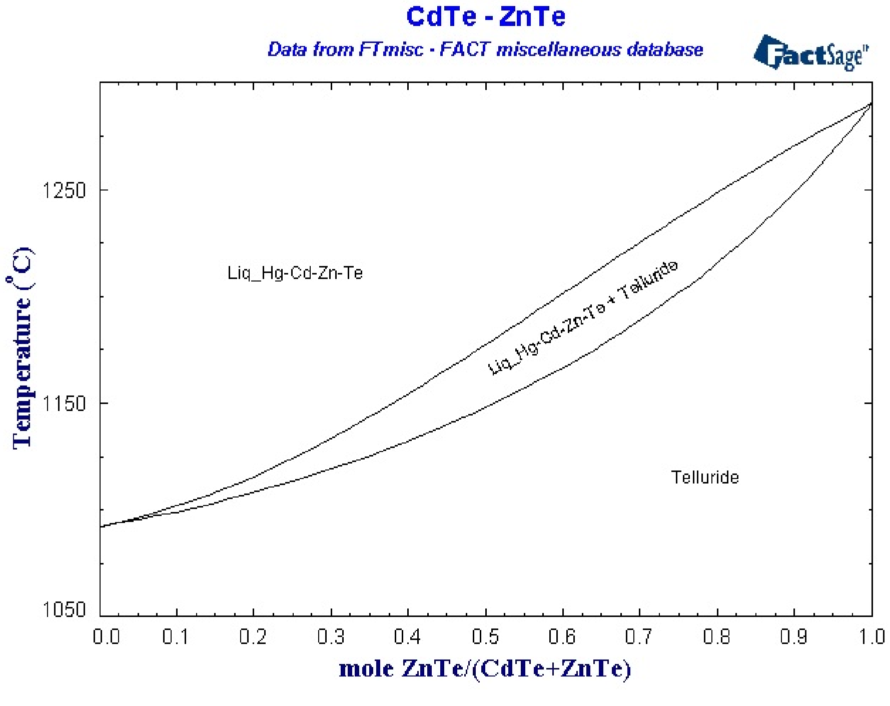

Figure 3.6. Phase Diagram for CdZnTe. Top line indicates liquidus temperatures, bottom line indicates solidus temperatures [57].

CZT crystal is typically grown by melt growth techniques such as Bridgman method and the travelling heater method (THM) which involve melting the precursor material, and then crystallizing the material by changing pressure, temperature, or a combination of both [45, 47, 58]. The Bridgman technique uses a "hot" and "cold" zone to create a temperature difference within a furnace. A seed crystal is placed at the base of the growth ampoule. The precursor material melts at the hot zone which is kept at a temperature of about 1130 °C above the melting point of CZT. As the growth ampoule moves through the furnace, hot zone is translated into the cold zone and the molten precursor gets solidified along with the seed crystal. Although Bridgman method has been used extensively to grow CZT material, crystals grown by this technique suffer from non-homogeneity, small grain sizes, and zinc segregation [9, 45, 47]

The travelling heater method (THM) requires the material to be grown be dissolved in a compatible solution. CZT grown using the THM technique involves placing pre-synthesized $Cd_{0.9}Zn_{0.1}Te$ and additional tellurium as the solvent material within a quartz ampoule [58]. The sealed ampoules are then placed in a furnace with a hot zone. Being a solution growth method, the growth temperature is lower for the travelling heater method compared to the Bridgman method. A uniform crystal without zinc segregation is achieved, however, THM requires that a homogeneous source ingot be used [58, 59]. Figure 3.7 shows schematic diagrams of Bridgman and THM methods and compares the temperature profiles for CZT crystal growth by these methods.

For this study, CZT single crystals were grown using solvent growth technique that combines many favorable features of the Bridgman method and THM growth methods. For example, as in Bridgman or THM, a seed crystal is used for directional growth of CZT single crystal. Like Bridgman method, synthesis of CZT compound from the elemental precursors and growth of single crystal are carried out in the same quartz ampoule, unlike THM which requires CZT to be pre-synthesized. On the other hand, similar to THM method, the solvent growth method requires lower growth temperature. For the solvent growth method of CZT with Te solvent, the melting temperature was ~980 °C. Furthermore, as in THM, the furnace was modified to perform multiple passes through hot/cold zone to ensure homogeneity and segregation of excess Te from the rest of the CZT ingot. Custom pulling and rotation was installed, along with automation via H-Bridge motor controller and Arduino microcontroller (Figure 3.9 and Figure 3.10).

3.2.4 CZT Growth by Tellurium Solvent Method

CZT crystals with stoichiometric ratio of $Cd_{0.9}Zn_{0.1}Te$ were grown by tellurium (Te) solvent growth technique using 50% excess Te as a solvent. Zone refined precursor elements at a Cd:Zn:Te ratio of 30:12:58 at% were used along with indium (In, at 15-25 ppm) as a dopant. The elemental materials were loaded into the carbon coated growth ampoule, which was then evacuated and sealed under ultra-high vacuum (10^{-6} torr or higher) to maintain an inert vacuum-sealed environment inside the ampoule (Figure 3.8). Ampoules were loaded onto the multi-zone growth furnace and attached to the puller and rotation system (Figure 3.9). Using progressively slower ramp-up rates, the furnace temperature was raised to 980 °C and held at that temperature for several hours to ensure a thorough melting of the precursor materials. Ampoule was then lowered to a zone of 900 °C for CZT synthesis. After synthesis, the ampoule was lowered into the cold zone at a very slow rate of 2 mm/hr to initiate single crystal growth. The CZT ampoule was rotated using accelerated crucible rotation, at a rate of 12 rotations per hour.

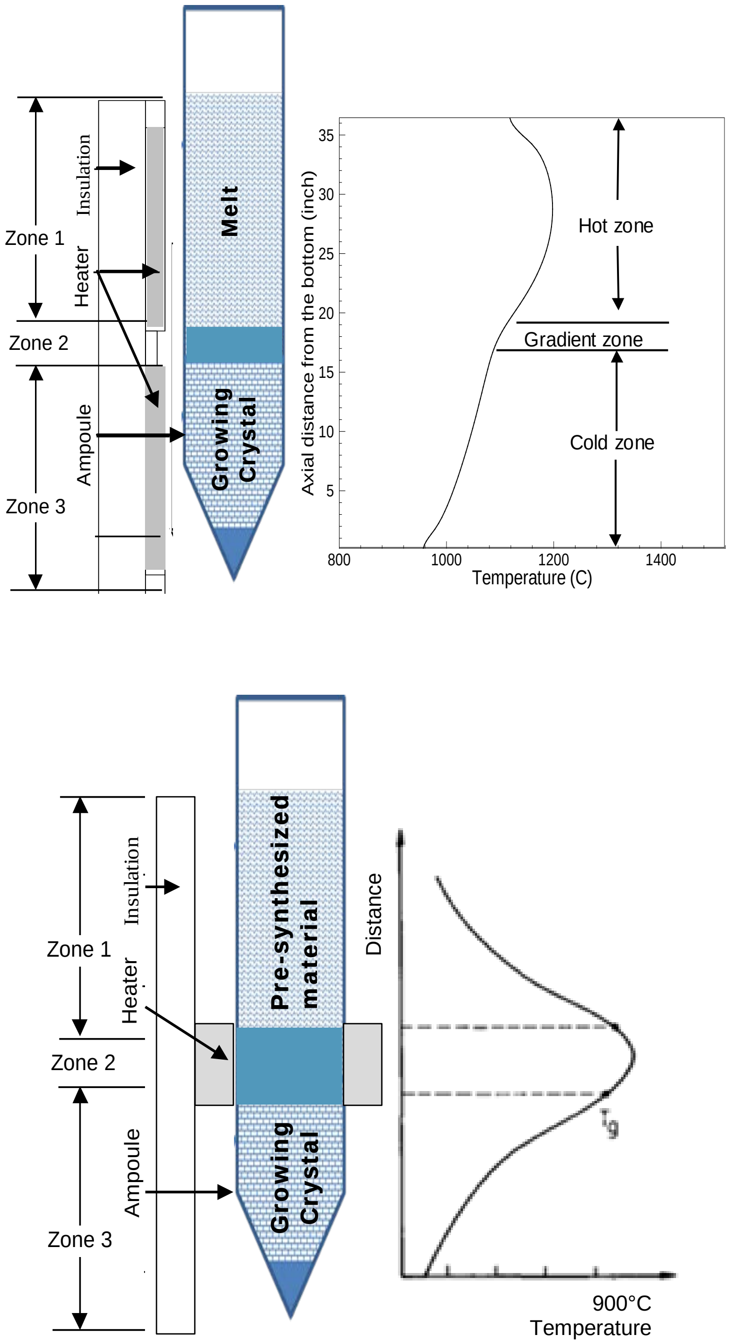

Figure 3.7. Schematic diagram and temperature profile of CZT crystal growth by Bridgman method (top) and travelling heater method (bottom)

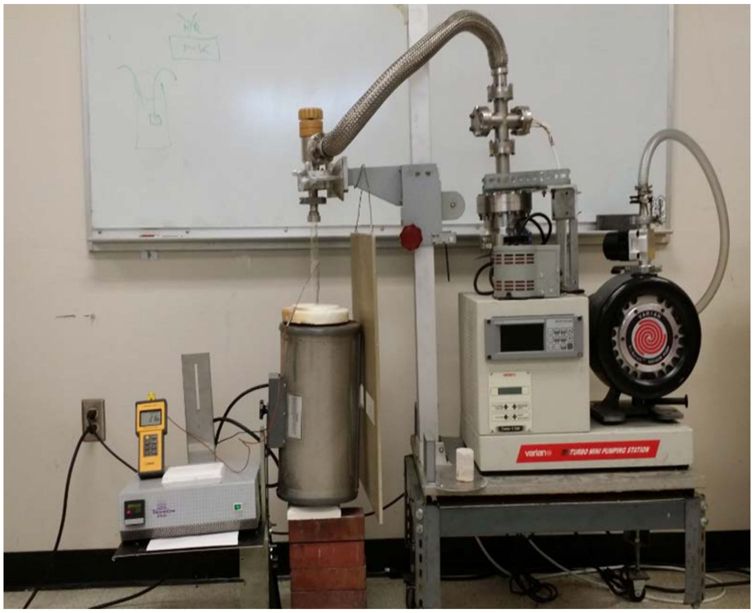

Figure 3.8. Picture of a quartz ampoule sealing set up at USC.

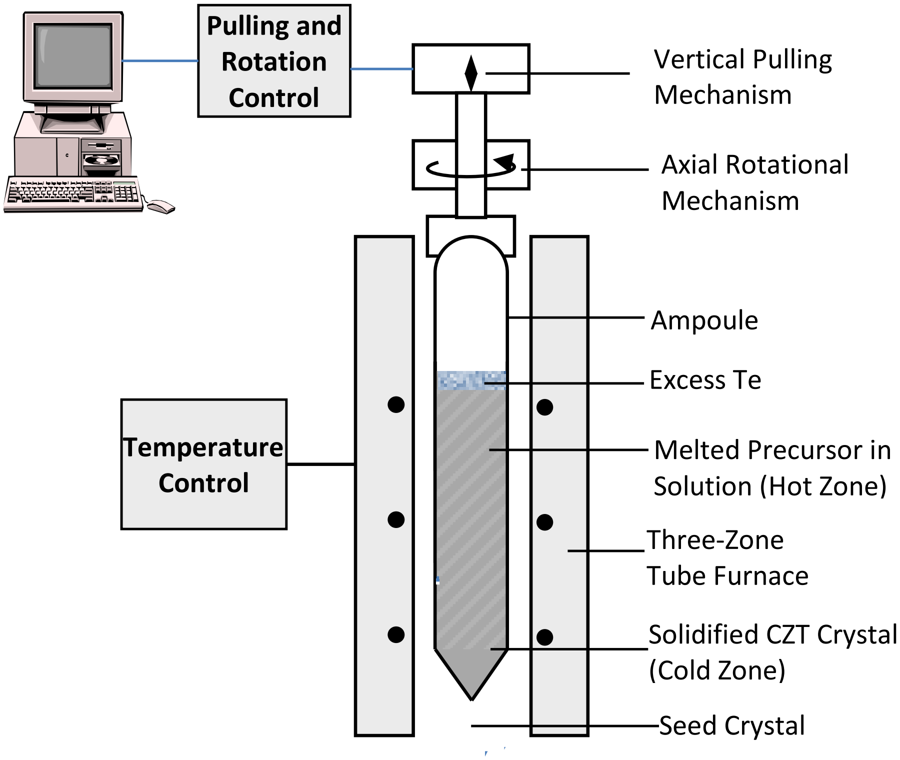

Figure 3.9. Schematic of CZT crystal growth furnace at USC.

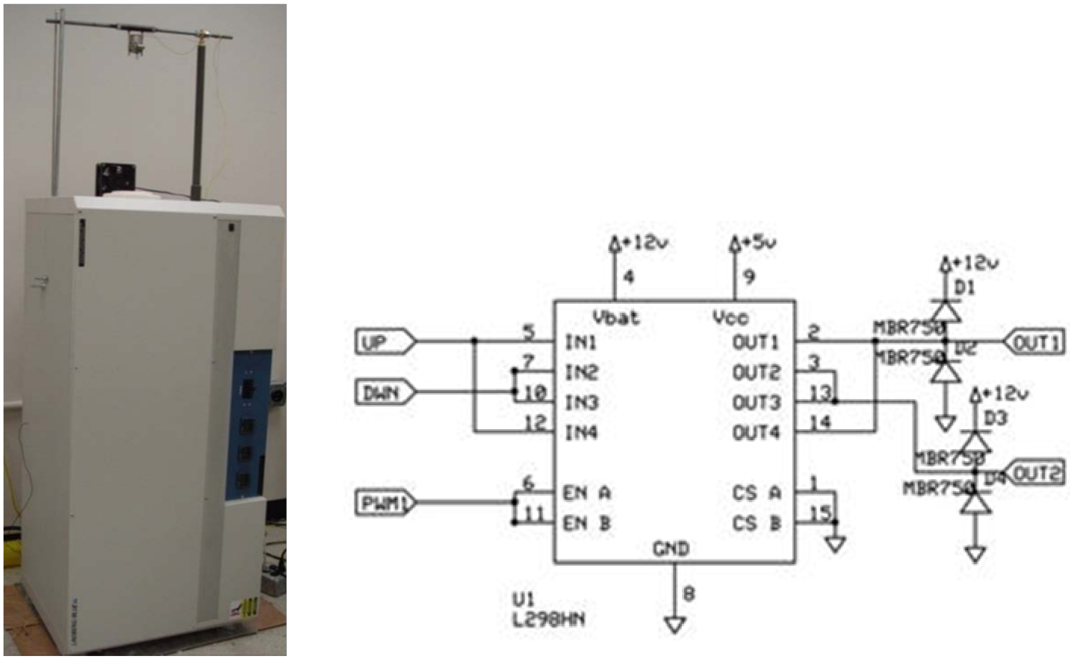

Figure 3.10. Picture of in-house growth furnace (left) with custom electronics for controlled pulling and rotation of the growth ampoule to ensure crystal quality and homogeneity. Custom pulling and rotation was installed, along with automation via H-Bridge motor controller and Arduino microcontroller.

After crystal growth, the quartz ampoule containing the grown CZT crystals were removed from the furnace, grown CZT ingot was retrieved by cutting the quartz ampoules, and CZT wafers are obtained by cutting the ingot carefully with a diamond wire-saw. Figure 3.11 presents pictures of grown CZT single crystal ingot and wafers. The cut crystal is then polished using a series of sandpapers of different grits and ultimately microfiber pads to achieve a mirror finish on all faces. CZT crystal wafers are then cleaned using an ultrasonicator, etched with 2% bromine-methanol solution (Br-MeOH) for 1 minute and 30 seconds, and rinsed off with de-ionized water. These wafers were then characterized prior to use as nuclear detectors.

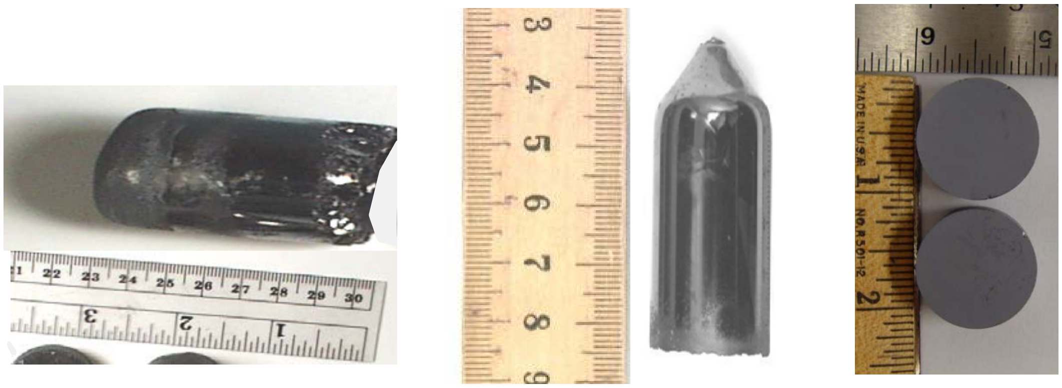

Figure 3.11. Typical pictures of grown CZT crystals: (left and middle) CZT crystal ingots and (right) two polished CZT crystal wafers.

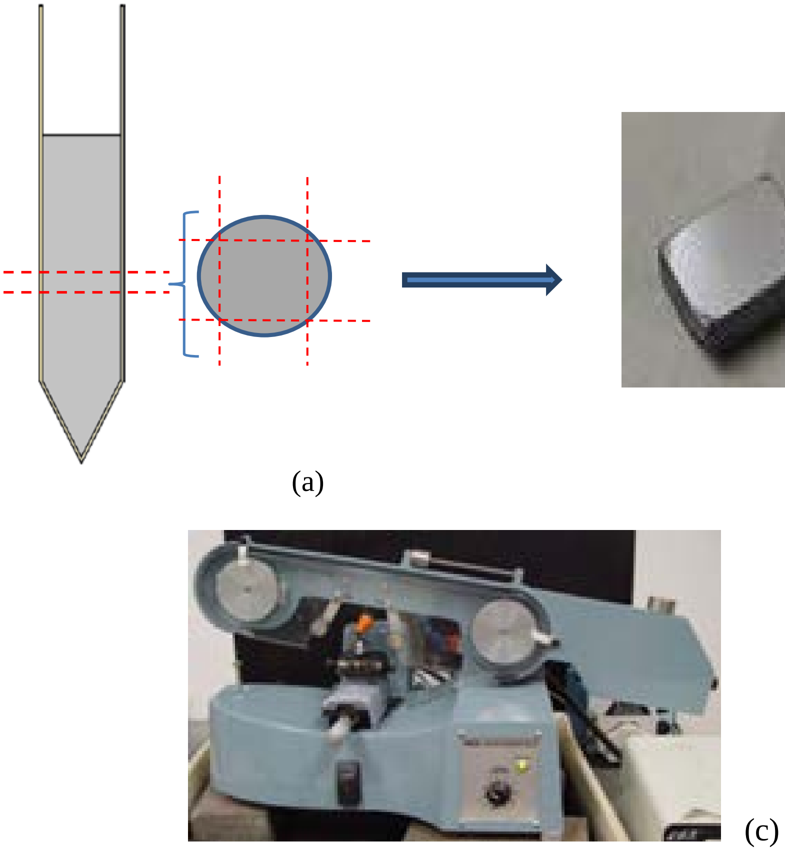

Figure 3.12. Schematic of a grown CZT ingot and a cut wafer (a) which was then diced and polished to mirror finish (b) in order to prepare for detector fabrication; (c) diamond impregnated stainless steel wire saw used to cut crystals.

3.3 CZT CRYSTAL CHARACTERIZATION

This section provides experiments and results of morphology; stoichiometry, optical and electrical characterization of the grown crystals to ensure their effectiveness as radiation detectors. Scanning electron microscopy (SEM) was used to analyze morphology of polished CZT wafers. Energy dispersive x-ray analysis (EDAX) was used to determine the stoichiometry of the CZT ingot. Optical transmission was used to determine band gap energy of the grown crystals. Electrical characterization through current-voltage (I-V) studies reveals the resistivity of the grown CZT material. Finally, deep-levels and surface defects were characterized using electron beam induced current (EBIC) and thermally stimulated current (TSC) measurements.

3.3.1 Morphological Characterization

CZT crystal wafers were polished using a series of sandpapers of different grits and ultimately microfiber pads to achieve a mirror finish on all faces. CZT crystal wafers were then etched with 2% bromine-methanol solution (Br-MeOH) for 1 minute and 30 seconds, and rinsed with DI water. These wafers were examined under scanning electron microscope (SEM) to assess their surface morphology. In SEM, beam of electrons are focused on the sample to form an image instead of light as in regular microscope. The electrons interact with atoms in the sample, producing various signals that are collected to produce images showing that surface topography of the sample. Because the SEM uses electromagnets rather than lenses, a much higher resolution could be obtained. Figure 3.13 (a) shows SEM images of the surface of grown CZT wafer samples. The SEM picture at left shows very smooth and shiny surfaces without any micro-cracks or defects. In order to do quantitative analysis of the crystal quality, etch pit density was evaluated by taking SEM picture of the grown single crystal after Everson etching [60]. The SEM picture in Figure 3.13 (b) shows etch pits revealed after etching. The etch pit density was $\leq 3 \times 10^4$ cm^{-2}, which also confirmed good crystal quality.

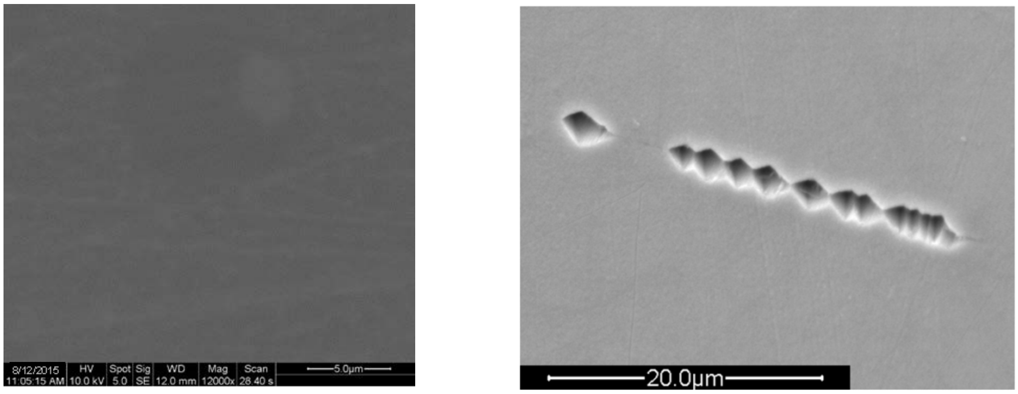

(a) (b)

Figure 3.13. (a) SEM picture of a polished and chemically etched CZT crystal wafer; (b) SEM picture of etch pits revealed after Everson etching.

3.3.2 Compositional Characterization

The goal was to grow CZT with $Cd_{0.9}Zn_{0.1}Te$ stoichiometry in order to produce detector grade crystals. Historically, stoichiometry has been a significant issue with CZT due to the segregation of Zn from the rest of the ingot. To verify the grown CZT crystals had desired stoichiometry (proper ratio of Cd:Zn:Te), multiple samples from grown CZT ingot were analyzed using energy-dispersive x-ray spectroscopy (EDAX).

Performed in a scanning electron microscope, EDAX is an important tool to determine the elemental composition of a material [39], where sample to be tested is bombarded with high-energy electrons from the SEM. These high-energy electrons excite and expel inner-shell electrons within the material, creating an electron-hole pair. As electrons from the outer shell fill the holes created by the excited inner-shell electrons, x-rays are generated. The energy of these x-rays is distinctive of the atom and contributes to the characteristic elemental peaks on the EDAX spectra. The element concentration is determined by integration of the peaks corresponding to the major elements present, and taking the ratio of the area under the peaks.

EDAX was carried out on five wafers cut at different axial distances along the grown ingot using a Tescan Vega 3 SEM-EDAX microscope. The surface of each sample wafer were polished (but not etched) and then scanned in three different spots simultaneously, and values were averaged. The Zn distribution profile presented in Figure 3.14 showed an approximately ± 5% deviation of stoichiometry at the top and bottom portions of the ingot, but less than 0.1% at the center. Due to a higher Zn distribution coefficient (K_{Zn} (CdTe) = 1.35 [61]), the axial variation of Zn concentration was higher at the growing-end (tip-end). However, the Zn concentration variation across the sliced wafer was much more uniform (≤ 1%).

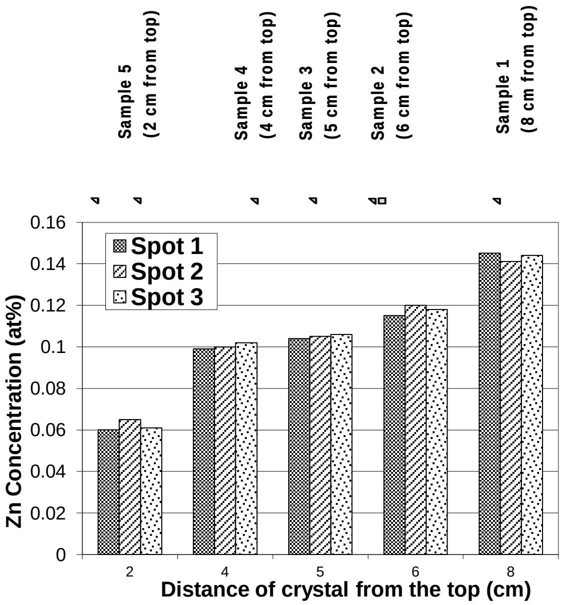

Figure 3.14. Zn axial and cross-sectional concentration profile of grown CZT crystals.

The EDAX data suggests that stoichiometric CZT crystals can be harvested from the middle to upper region of the CZT ingot grown by the solvent growth method. Thus the CZT wafers obtained from these regions were used for radiation detector fabrication.

3.3.3 Optical Characterization

For high resolution detector performance, large bandgap energy (≥ 1.5 eV) is required so that detection signal is due to ionization by radiation only not due to thermal noise. Hence, optical characterization was performed using UV-Vis spectroscopy to determine bandgap energy. For this study, transmission properties were measured from 750 nm to 1500 nm wavelengths using a thin (~ 30 μm thickness) CZT wafer. The band gap energy, E_g, was calculated from the cut-off wavelength (λ) of the transmission spectrum, by using the following equation:

$$E_g = \frac{hc}{\lambda} \qquad 3.1$$

where h is Planck's constant, c is the speed of light, Eg is the band gap of the CZT crystal, and λ is the cut-off wavelength. The optical transmission results for grown CZT and CdTe (reference sample) samples are shown in Figure 3.15. The optical transmission is ~60% for CZT for wavelengths greater than 800-900 nm. As can be seen, the band edge for the reference CdTe crystal is at a longer wavelength as expected than the band edge for the CZT crystal (due to addition of Zn). The band gap of CZT sample was calculated from the cut off wavelength of the transmission spectrum and calculated to be ~1.56 eV which is within the expected range for $Cd_{0.9}Zn_{0.1}Te$ and is ideal for semiconductors employed in nuclear detectors.

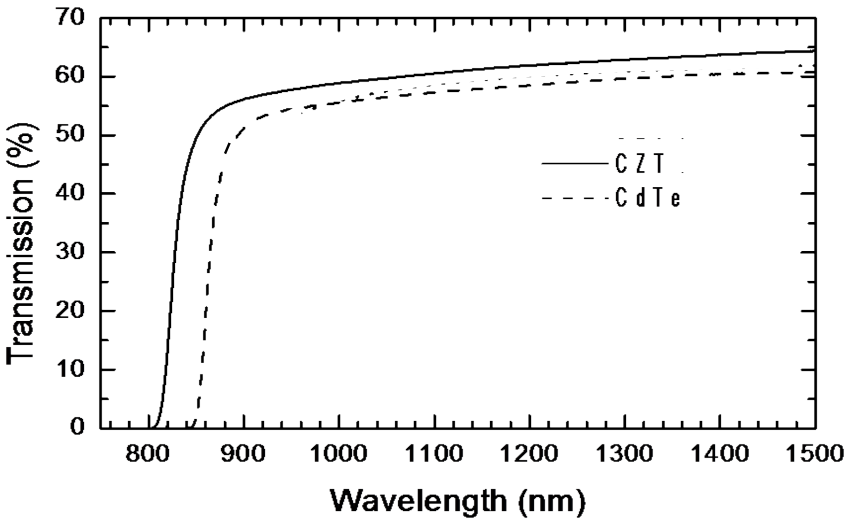

Figure 3.15. Optical transmission properties of a solution-growth CZT wafer. CdTe was used as a reference.

3.3.4 Electrical Measurements: Resistivity

For high performance detector, CZT crystal must be of high resistivity, which will reduce the leakage current flowing through the detector when biased. Current-voltage (I-V) studies using metal-semiconductor junction is used for electrical characterization to determine the resistivity of the grown CZT material. The current-voltage characteristic (I-V characteristic) of a metal-semiconductor junction is determined by the barrier height at the interface. There are two types of metal-semiconductor junctions: (i) Ohmic contact which has no barrier, allowing holes and electrons to travel through the semiconductor without being blocked and thereby producing a linear current-voltage response; (ii) Schottky contact is a rectifying contact which has potential barrier at the interface restricting carrier movements and produces a non-linear response. For nuclear detectors, an Ohmic contact is preferred since it allows the detector to have higher charge collection efficiency.

The following formulas can be used to calculate the barrier height at the metal-semiconductor interface:

$$\phi_b = \phi_m - \phi_s \qquad 3.2$$

$$\phi_s = \chi + (E_C - E_F) = \chi + \frac{Eg}{2} \qquad 3.3$$

where ϕ_b is the barrier height, ϕ_m is the metal work function, ϕ_s is the semiconductor work function, E_c is the energy of the conduction band edge, E_F is the Fermi-level energy, E_g is the bandgap energy, and χ is the electron affinity. The electron affinity of CZT is about 4.3 eV and the bandgap energy was determined to be 1.56eV. Using these values in Equation 3.3, the work function of CZT was calculated to be at 5.08eV.

CZT crystals grown in our laboratory contains indium doping in order to compensate for intrinsic defects. It was reported that doping with indium also increases the resistivity and makes CZT slightly p-type [62]. To form an Ohmic contact with a p-type semiconductor, a metal must have higher work function compared to that of the semiconductor ($\Phi_m > \Phi_s$) [42]. Opposite (($\Phi_m < \Phi_s$) is true for an n-type semiconductor. CZT has a work function of 5.08eV as calculated above, so the metal to form the Ohmic contact needs to have a work function greater than 5.08eV. There are very few metals with such high metal work function; examples are gold (Au, Φ_m = 5.4eV) and platinum (Pt, Φ_m = 5.64eV). Since Au is an inert metal can be deposited by electroless deposition and sputtering, it was the metal of choice to make CZT radiation detector.

A simple CZT detector of 7 × 7 × 5 mm^3 was fabricated by forming contacts with gold, applied to the top and bottom of the CZT crystals by DC sputtering, using a Quorum Q150T DC sputtering unit. Current-voltage (I-V) characteristics were carried out by measuring the current flowing through the CZT detector at various applied voltage bias across the detector. I-V characteristics were carried out at room temperature using a Keithly 237 electrometer setup. The electrical resistance was estimated from inverse slope of the linear regression of current-voltage curve. The resistivity was calculated using the following equation:

$$\rho = R \cdot \frac{A}{L} \qquad 3.4$$

where ρ is the resistivity of the crystal in Ohm-cm, R is the resistance in Ohms, A is the contact area (cm^2), and L is the thickness of the CZT crystal in cm. Figure 3.16 shows the current-voltage characteristic of a CZT detector with gold contacts (2.6 mm electrode diameter). From the inverse slope of the linear fit of the I-V characteristic and using Equation 3.4, the electrical bulk resistivity was estimated to be 2×10^{11} Ω-cm. This is high enough resistivity to fabricate a functional CZT radiation detector. The CZT detectors showed very low leakage current at a high bias (below 5 nA at – 1000V) due to their high resistivity, which are beneficial for high resolution detectors.

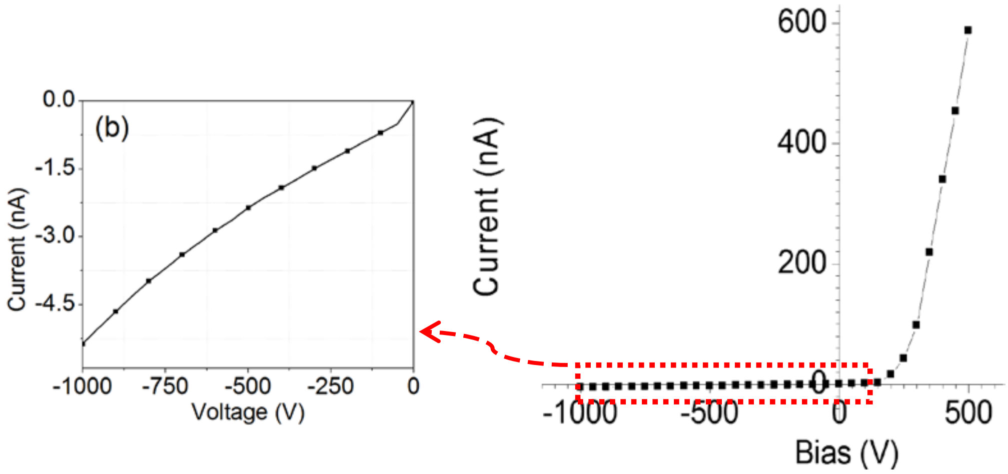

Figure 3.16. I-V characteristic of a detector-grade CZT crystal (right) and detailed reverse bias I-V characteristic (left).

3.4 DEFECT CHARACTERIZATION FOR CZT SCHOTTKY DEVICES

The crystallographic defects and impurities in grown CZT crystals constrain its nuclear detector performance. CZT crystals grown by various methods have been associated with formation of Te inclusions/precipitates and zinc segregation in the grown crystals which have resulted in major crystalline defects such as dislocations, grain boundaries, and twinning [37, 50, 51]. Such defects impede pulse charge collection due to the presence of deep electronic defect levels which act as traps and recombination centers for mobile charge carriers. Macro-defects such as cracks, grain-boundaries, and twin-boundaries can lower the yield of usable single-crystal volume of CZT ingot. Surface defects can cause increased leakage current and poor noise performance for a fabricated CZT detector. Furthermore, deep defect levels within the CZT semiconductor can act as charge traps (electron or hole), which can trap the charges generated due to interaction with nuclear radiation [52]. In particular, the poor hole transport properties of CZT caused by deep-level defects require that special detector geometries be applied to CZT-based detectors. Therefore it is critical to study and further improve the understanding on the formation and characteristics of these electrically active defects which degrade CZT based detector performance.

Using non-destructive characterization techniques such as electron beam induced current (EBIC) and thermally stimulated current (TSC) spectroscopy measurements, the crystallographic defects can be visually identified and correlated to the mobile charge loss in detectors as affected by defect trapping and recombination effects. Additionally, TSC has been used to determine the activation energy associated with the deep level defects in the grown CZT crystals.

3.4.1 Thermally Stimulated Current (TSC)

Defect analysis using Thermally Stimulated Current (TSC) experiments was performed to determine the presence of deep-level defects within the grown CZT crystals. In TSC experiments, a semiconductor sample is cooled to a temperature below 100 K. At this temperature, first the trap centers for holes/electrons are filled using photon energy. The sample is then heated slowly at a constant rate; as a result, the energy stored in the traps is released. The current generated by the trapped charges are recorded and plotted as a function of temperature producing TSC spectra. The TSC peaks representing trap centers will appear at various heating rates, and can be plotted on an Arrhenius plot. The activation energies of the trap centers can be determined from the slope of the Arrhenius plot, generated from the trap centers T_m, using the following equation [63]:

$$\frac{E_T}{kT} = \ln\left(\frac{T_m^4}{\beta}\right) + \ln\left(\frac{10^{17} * \sigma}{E_T}\right) \qquad 3.5$$

where E_T is the activation energy of the trap level, β is the heating rate, σ is the capture cross section, k is the Boltzmann’s constant, and T is temperature. After determining the activation energy, TSC peaks were fit using the following equation to determine the trap capture cross section:

$$I_{TSC} = CV_b q\mu\tau N_T e * \exp\left(-\int \frac{e}{\beta \mathrm{d}T}\right) \qquad 3.6$$

where C is the constant related to the sample geometry, V_b is the bias voltage, q is electronic charge, μ is the carrier mobility, τ is the carrier lifetime, N_T is the trap capture cross section, e is the emission rate of trapped carriers, and β is the heat rate.

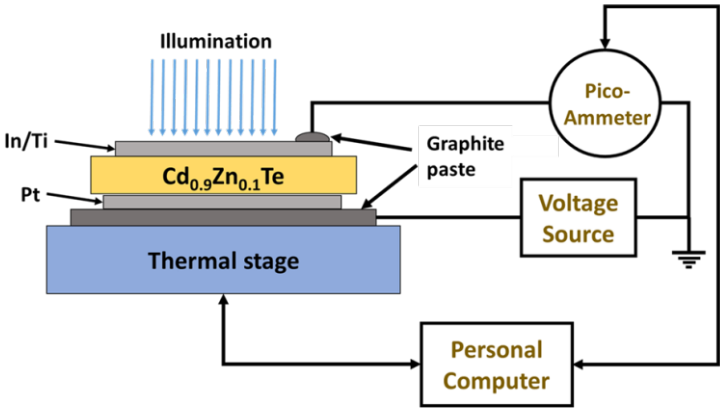

Figure 3.17. Schematic of the thermally stimulated current TSC experimental setup.

Figure 3.17 shows the schematic of TSC experimental setup. A thermal stage provided temperature variation, and the generated TSC spectrum was controlled and recorded using a Keithley 6517A electrometer connected to a PC running LabVIEW software. The CZT Schottky diode was attached to the thermal stage using graphite paste. TSC measurements were conducted from a temperature range of 94 to 400 K under a 10^{-5} torr vacuum inside a low temperature microprobe station. CZT Schottky diodes (1 cm x 1 cm x 0.1 cm) with indium (In, ϕ_m = 4.12 eV) and/or titanium (Ti, ϕ_m = 4.33 eV) as top contact and platinum (Pt) as bottom contact were used for TSC experiments. Traps in the CZT diode were filled by illumination at 94 K for 2 minutes using a 10 W white halogen light bulb through a microscope window. To analyze TSC spectrum and to identify the CZT defect levels, we have used the simultaneous multiple peak analysis (SIMPA) method [64, 65]. The TSC spectrum is a sum of all charge released by defect levels and can be expressed as:

$$I_{SIMPA}(T) = \sum_{i=1}^{m} I_{TSC}^{i}(T) + I_{dark}(T) \qquad 3.7$$

where $I_{TSC}^{i}(T)$ represents the i^{th} individual TSC peak and m is the total number of defect levels that contribute to the peak analysis at temperature T.

Figure 3.18 shows the TSC spectrum of the fabricated CZT Schottky detector, carried out at a heating rate of 15 K/min and under a bias of -10V. To this spectrum simultaneous multiple peak analysis (SIMPA) curve fitting was applied. The curve fitting has identified the defect levels D_1-D_{11}, which are described by discrete TSC peaks, and their respective energy levels and capture cross sections are summarized in Table 3.2. The cross-sections of defects were calculated assuming an effective-to-rest electron mass ratio (m^*/m_o) of 0.1128. Defect levels D_1 and D_2 are related to the so-called A centers in the CZT crystals affected by Cd vacancies and shifted by In doping [64, 66, 67, 68]. Defect level D_3 has been attributed to a V_{Cd}^{-} or V_{Cd}^{2-} defect in the literature [69, 70], and may be related to the A center levels. Defect levels D_4-D_8 have been observed to be related to the V_{Cd}^{2-} defect [64, 68, 69, 70], however defect level D_4 has also been theoretically calculated to be related to a Te-Te split bonding complex energy level [64, 71, 72]. Defect levels D_9-D_{11} are related to a Te_{Cd} antisite complex which may be related to the growth method (Te-solvent) and Te inclusions [66, 72].

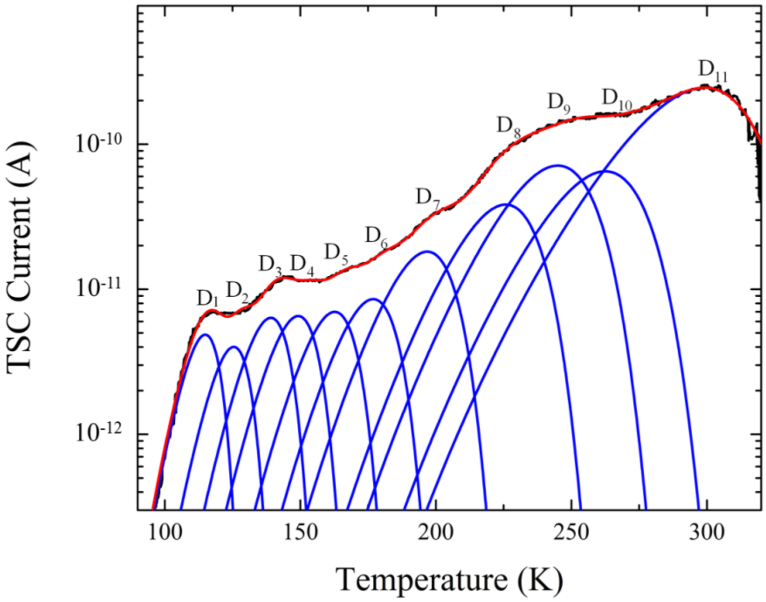

Figure 3.18 Thermally stimulated current (TSC) spectrum of CZT Schottky diode radiation detector (heating rate: 15 K/min, reverse bias: - 10 V), fitted by the simultaneous multiple peak analysis (SIMPA) method.

Table 3.2. Trap parameters deduced from TSC measurement of the fabricated CZT Schottky diode radiation detector presented in Figure 3.18.

Deep level defects	**Activation energy (eV)**	**T_m (K)**	**Capture cross sections (cm^2)**	**Origin of defect levels**	**Ref.**
D_1	0.181 ± 0.007	115.2	1.960×10^{-19}	A center, [V_{Cd}-In]$^-$	67, 68, 69
D_2	0.199 ± 0.026	125.3	7.263×10^{-19}	A center, [V_{Cd}-In]$^-$	67
D_3	0.215 ± 0.014	139.1	6.833×10^{-19}	V_{Cd}^-/ V_{Cd}^{2-}	70, 71
D_4	0.231 ± 0.038	149.3	3.091×10^{-19}	V_{Cd}^{2-}, $(Te\text{-}Te)_{spl.}$	64, 71, 72
D_5	0.251 ± 0.026	162.7	2.431×10^{-19}	V_{Cd}^{2-}	67
D_6	0.269 ± 0.021	177.0	1.750×10^{-19}	V_{Cd}^{2-}	68
D_7	0.287 ± 0.006	196.6	1.102×10^{-19}	V_{Cd}^{2-}	73
D_8	0.315 ± 0.002	225.8	3.619×10^{-20}	V_{Cd}^*	68, 69, 70
D_9	0.329 ± 0.003	244.9	1.090×10^{-20}	Te_{Cd} complex	68, 72
D_{10}	0.354 ± 0.005	262.5	4.433×10^{-21}	Te_{Cd} complex	67, 68, 72
D_{11}	0.370 ± 0.003	299.1	3.968×10^{-21}	Te_{Cd} complex	68, 72

3.4.2 Electron Beam Induced Current

Electron Beam Induced Current (EBIC) analysis provides a unique correlation between collected current in a semiconductor sample under an electron beam and electrical defect properties in that sample. EBIC measurement produces an image displaying contrast by the variation of collected current. The crystallographic defects often are electrically active and introduce energy levels into the semiconductor band gap, acting as recombination or mobile carrier trap centers. Furthermore, if these defects are shallow level defects, then they may assist in unintentional doping and carrier concentration modulation. Defects in the CZT crystal can be delineated by observing the contrasts in the image which are the results of space-charge trapping [74].

Figure 3.19 presents the schematic of the EBIC setup. EBIC is performed using a scanning electron microscope (SEM). The electron beam from the SEM electron gun strikes semiconductor device, and as the beam scans across the sample, electron-hole pairs are generated in the semiconductor sample, and separated by the internal electric field due to the built-in space-charge region [75]. The resulting signal current is amplified and used as an image signal. Variations in the generation, recombination, and drift of the electron-hole pairs will result in variations in the contrast of the EBIC image. These variations are most likely caused by the spatial differences in crystal quality and defects within the semiconductor material.

According to the EBIC theory [74], total EBIC current (I_{EBIC}) at a point is sum of defective and defect-free regions. The current in the defect-free semiconductor (I_0) forms the background of EBIC image and depends on energy of the electron beam, E. The EBIC current of the defect region (I^*) forms the contrast in the image and depends on the defect strength γ and the point spread function H^* according to the following equations [74]:

$$I_{EBIC}(\xi,\eta,E) = I_0(E) + I^*(\xi,\eta,E) \tag{3.8}$$

$$I^*(\xi,\eta,E) = \iiint_F dxdydz\gamma(x,y,z)H^*(x-\xi,y-\eta,z;E) \tag{3.9}$$

where I_{EBIC} (ξ, η, E) is the total collected current, x, y, z are Cartesian coordinates, ξ, η are the point coordinates in the XY plane where the EBIC current is considered, I_0 (E) is the EBIC current in the defect-free region, $I^*(\xi, \eta, E)$ is the current contributed by the defect region, E is the energy of the electron beam, F is the region of space occupied by defect.

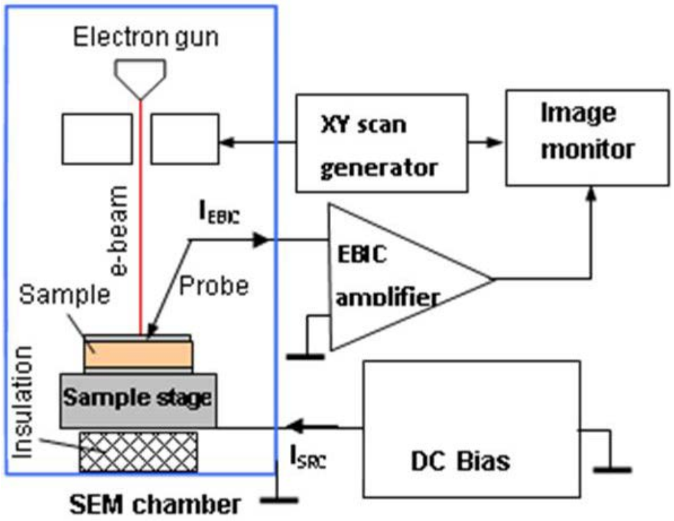

Figure 3.19. Schematic of electron beam induced current (EBIC) setup.

EBIC contrast images (spot size ~ 500 nm with accelerating voltage 23 kV) were taken on the CZT Schottky diode using a JEOL-35 SEM with the detector under reverse bias (50–100 V). CZT Schottky diode with indium (In) metal contact and platinum (Pt) back contact was used for EBIC study. The EBIC image of the reverse biased CZT

Schottky diode is presented in Figure 3.20 (b) and correlated to infrared transmittance (TIR) images of the CZT surface (Figure 3.20 (a)). The EBIC image shows interpenetrating dark and white regions. The leakage current in the diode is higher in the defective regions. Therefore dark regions in Figure 3.20 (b) represent defective regions having high leakage current, whereas white regions represent areas devoid of any defects due to the semi-insulating resistivity and lower leakage current.

The black spots observed in the TIR image in Figure 3.20 (a) are due to the inhomogeneity of the Te inclusions/precipitates distribution in the sample, whereas clear white areas are closer to stoichiometric $Cd_{0.9}Zn_{0.1}Te$ in composition. The morphology of the EBIC contrast image is similar to the TIR image morphology, with higher contrast regions in the EBIC image corresponding to a non-uniform distribution of tellurium (Te) within the bulk crystal. The results give insight on the type and severity of the electrical defects present with the CZT crystals grown by solvent growth method using excess Te as the solvent. This will assist in optimization of crystal growth process to reduce crystal defects produced in future growth runs.

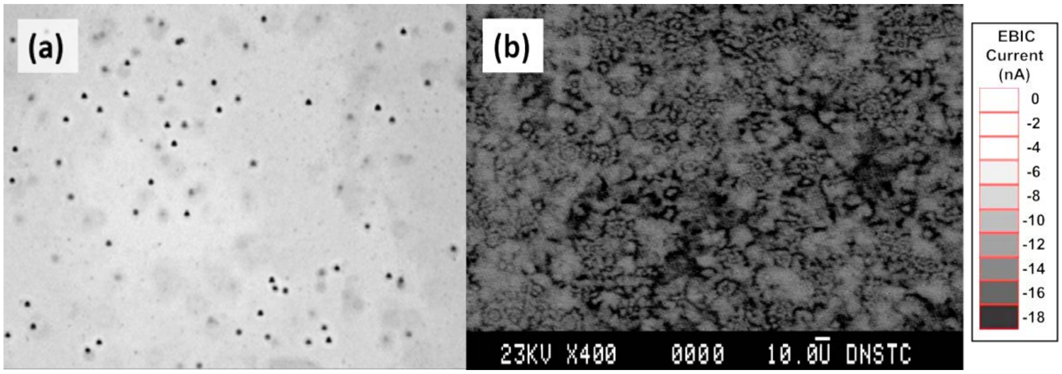

Figure 3.20. (a) IR transmittance image and (b) EBIC contrast image of the CZT Schottky detector.

3.5 CZT NUCLEAR DETECTOR FABRICATION

Following the material characterizations, low-defect bearing CZT crystal wafers were used for detector fabrication. Prior to detector fabrication, the grown CZT wafers were lapped by alumina suspension of various grain sizes down to 0.3 μm and polished by diamond paste of 0.03 μm grain sizes. The wafers were then etched by applying the following cycle: 0.5 % Br_2/MeOH dip for 20 seconds, ultrapure methanol rinse and final drying by blowing pure nitrogen. Just before depositing the top and bottom metal electrode on the CZT, the wafers were etched for 2 minutes in KOH-KCl solution (15 % each), then rinsed thoroughly in DI water and finally dried by blowing with nitrogen. This procedure gave the best results as it removed Te-rich oxides from the surfaces.

The electrodes were formed by DC sputtering semitransparent gold (Au) contact (100 – 120 Å) on one side using a metal mask and by depositing indium (In) contact (200 – 500 Å) on the opposite side using e-beam evaporation. Palladium or copper wires of 25 μm in diameter were attached to the electrodes by applying a 1 mm diameter graphite suspension in n-butyl acetate. The detectors fabricated in this manner were secured on an alumina substrate using a silicone adhesive (Dow Corning, RTV 3140).

Two types of detector structures were explored to fabricate CZT gamma ray detectors: planar metal-semiconductor-metal (MSM) structure and guard ring structure. The contact schematic, as well as photographs of the planar single pixel detectors fabricated in our laboratory, are shown in Figure 3.21. In a planar detector structure, large metal contacts are placed on both sides of the detector material. In this configuration, gamma-rays will interact with the semiconductor material to produce electron-hole pairs. Generated electrons will move towards the positively biased anode, and holes will move towards the negatively biased cathode. The readout signal is taken from the anode, and assuming neither holes nor electrons are lost when travelling to the contact electrodes, the charge seen by the electrodes ΔQ is expressed as follows:

$$\Delta Q = -(he_0)(0 - Z) + (ne_0)(1 - Z) = ne_0 \tag{3.10}$$

where h is the number of holes detected, n is the number of electrons detected, e_0 is the charge of an electron, and Z is the interaction depth within the detector [76]. If both the energy of the holes and the energy of the electrons are being read without loss of information, the charge read at the contact electrodes is independent of the depth of interaction.

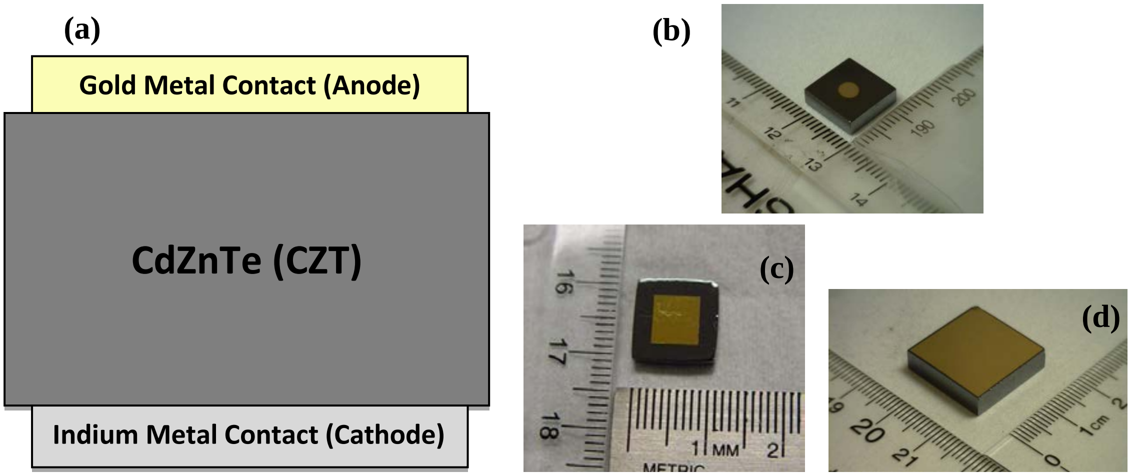

Figure 3.21 Schematic cross-sectional view of a CZT planar detector (a). Picture of fabricated planar single pixel detector using grown CZT crystal: (b) 12×12×4 mm^3; (c) 10×10×3 mm^3; and (d) 18×18×5 mm^3.

Guard ring structure was explored to reduce the noise caused by surface leakage current within a nuclear detector. Figure 3.22 shows schematics of the cross-sectional and top view of a guard ring structure. A guard ring structure involves the use of an anode contact electrode, surrounded by a space where only the bare semiconductor surface exists (no contact electrode). After the bare surface, another metal contact is placed, known as the guard ring. The anode is connected to the read-out electronics and the guard ring is kept at the same voltage potential as the anode. Since the guard ring is not connected to the anode, all current caused by surface conduction will be blocked by the guard ring, and therefore not interfere with the resulting detection signal from the anode, improving signal to noise performance of the detector.

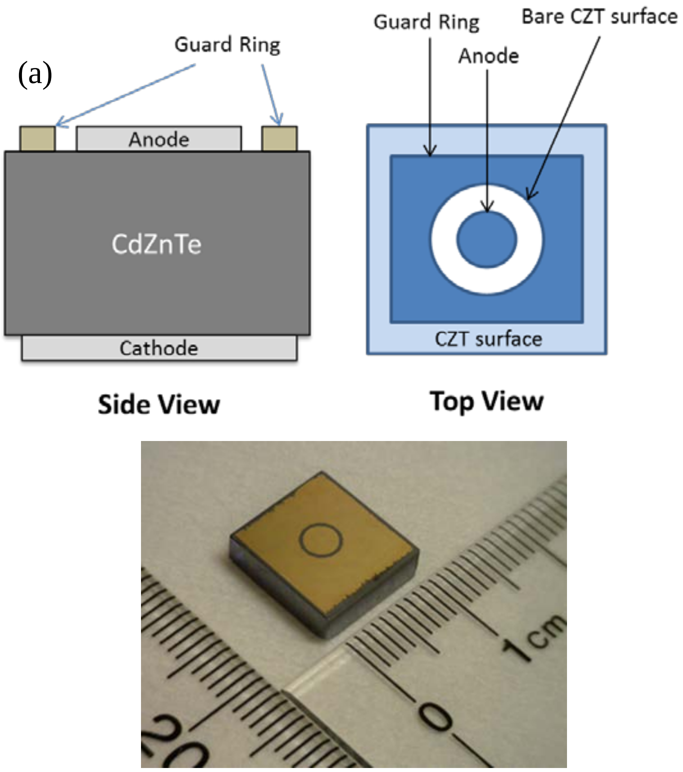

Figure 3.22. Schematics of a guard ring structure: (a) cross-sectional view and (b) top view; (c) picture of a typical single element guard-ring CZT detector (10×10×5 mm^3) fabricated at USC.

3.6 ELECTRICAL CHARACTERIZATION OF CZT DETECTOR

Prior to CZT detector testing with gamma-ray irradiation, electrical characterization of fabricated CZT detectors were carried out using current-voltage (I-V), capacitance-voltage (C-V), and charge transport measurements. I-V and high frequency (100 kHz) C-V measurements of the Schottky detectors were performed using a Keithley 237 High Voltage Source Measure Unit and a Keithley 590 CV Analyzer. All measurements were performed at room temperature (RT) under dark condition with forward voltage applied to the In/CZT/Au Schottky contact.

3.6.1 Current-Voltage Measurements

Current-voltage (I-V) characterization is an important assessment for fabricated CZT nuclear detectors. Detectors with high resistivity and stable I-V characteristics are more likely to produce high energy resolution under gamma-ray irradiation, by reducing the leakage current of the detector under voltage bias. Current-voltage characteristics were carried out by measuring the current flowing through the CZT detector at various applied voltage bias across the detector. Figure 3.23 shows I-V characteristics for In/CZT/Au detector at various applied bias. As discussed in detail in Section 3.3.4, the resistivity was measured form the inverse slope of the linear fit of the I-V characteristic and using Equation 3.4. The electrical resistivity was estimated to be 7×10^{10} Ω-cm with In/CZT/Au Schottky contact. This is high enough resistivity to fabricate a functional CZT radiation detector. I-V characteristics indicate high rectification ratio for the detector with small leakage current (~1 nA at 50V reverse bias). Such detector can be used for nuclear radiation detection applications with low noise at room temperature.

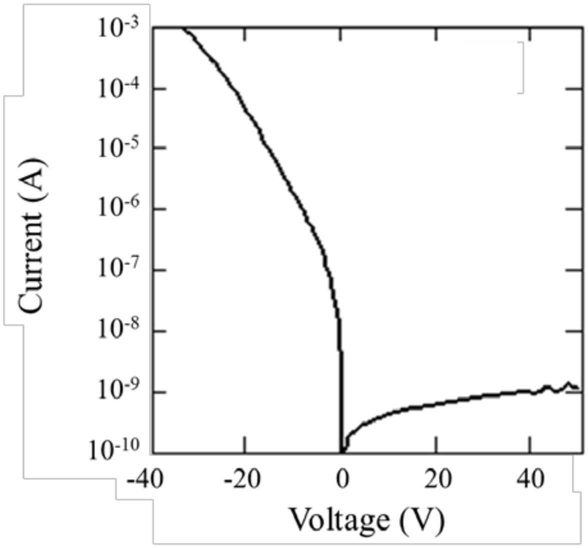

Figure 3.23. Room temperature current-voltage (I-V) characteristic of the 10×10×10 mm^3 CZT Schottky diode detector

3.6.2 Capacitance-Voltage Measurements

Capacitance-voltage (C-V) measurements were carried out to determine the full depletion bias. In a Schottky device, the depletion region at the metal-semiconductor junction extends fully to the semiconductor side. The capacitance (*C*) at the metal-semiconductor junction of the Schottky device is a function of depletion width, *W*, of the junction, which in turn depends on the applied bias across the detector. These relationships can be described by following equations [42]:

$$C = \frac{\varepsilon \times \varepsilon_0 \times A}{W} \tag{3.11}$$

$$W = \sqrt{\frac{2\varepsilon\varepsilon_0 \times (V_{bi} - V)}{qN_d}} \tag{3.12}$$

where C is capacitance, W is depletion width, A is the area of the junction, ε is the dielectric constant of semiconducotor material, and ε_0 is the permittivity in vacuum, q is the electronic charge (1.6 × 10^{-19} C), N_d is the effective doping concentration in the semiconductor, V_{bi} is barrier height at the junction (or junction potential) and V is the applied bias. Thus junction capacitance is inversely proportional to the applied bias.

Therefore, with increasing reverse bias, the width of the depletion region, *W*, will increase (Equation 3.12). Consequently, the capacitance, *C*, will decrease with increasing reverse bias, as per the Equation 3.11. High frequency (100 kHz) capacitance-voltage (C-V) characteristics of the CZT Schottky detector are shown in Fig. 6. The figure shows that under applied reverse bias capacitance first decreases but then levels off, displaying that the detector is almost fully depleted, which is ideal for higher charge collection efficiency. The semi-insulating nature of the CZT crystal is confirmed by this C-V characteristic.

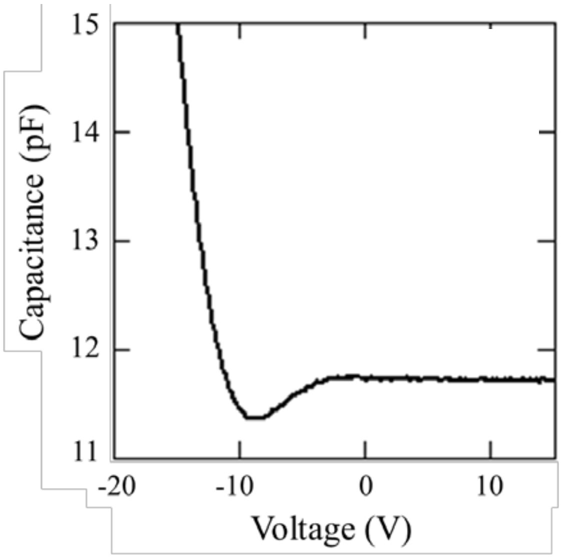

Figure 3.24. High frequency (100 kHz) capacitance-voltage (C-V) characteristic of the 10×10×10 mm^3 CZT Schottky diode detector (same detector as in Figure 3.23)

3.6.3 Charge Transport Measurements

As discussed earlier, the time electrons and holes takes to travel through the detector material to reach the respective electrodes is critical for high charge collection efficiency, subsequently for detector performance. Therefore, it is important to determine charge transport properties, such as drift mobility (μ), carrier lifetime (τ), and especially, carrier lifetime mobility product (μτ) for both charge carriers (electrons and holes), in order to assess detector performance. However, since hole charge transport properties are far worse than electron transport properties in CZT, the attention was given to transport properties of electrons.

Drift mobility of electron (μ_e) is defined as the velocity acquired by a charge carrier per unit applied electric field, and is given by the following equation [42]:

$$v_d = \mu_e E \tag{3.13}$$

$$E = \frac{V}{L} \tag{3.14}$$

where v_d is the electron drift velocity of electrons, E is the electric field, V is the bias voltage applied to the device, and L is the detector thickness. The carrier lifetime (τ) is defined as the average time charge carriers spend between generation and recombination. The mobility-lifetime product (μτ) is the product of the carrier mobility (μ) and the carrier lifetime (τ).

It is possible to measure the drift velocity of the electrons for a nuclear detector, under a known electric field bias, using time-of-flight measurement [77]. In this measurement, a detector is irradiated with a ^{241}Am alpha particle source on the cathode of the detector. The alpha particles have very less penetration depth in CZT, and will generate electron-hole pairs just below the cathode. So the generated electron will have to travel the entire distance across the detector to reach to anode at the other end. The anode will be grounded, and will collect the resulting generated signals. The signal is then translated to provide a mean rise time representing time required for electrons to reach to anode. The drift velocity is then calculated for each rise time using the relationship:

$$v_d = \frac{L}{t} \qquad 3.15$$

where L is the detector thickness in cm, and t is the rise time in seconds. By plotting drift velocities versus electric field, the electron mobility could be determined from the slope of a linear fit of the data (Figure 3.25). This process was performed on the CZT planar detector, and the electron mobility was calculated to be 1186 cm^2/Vs.

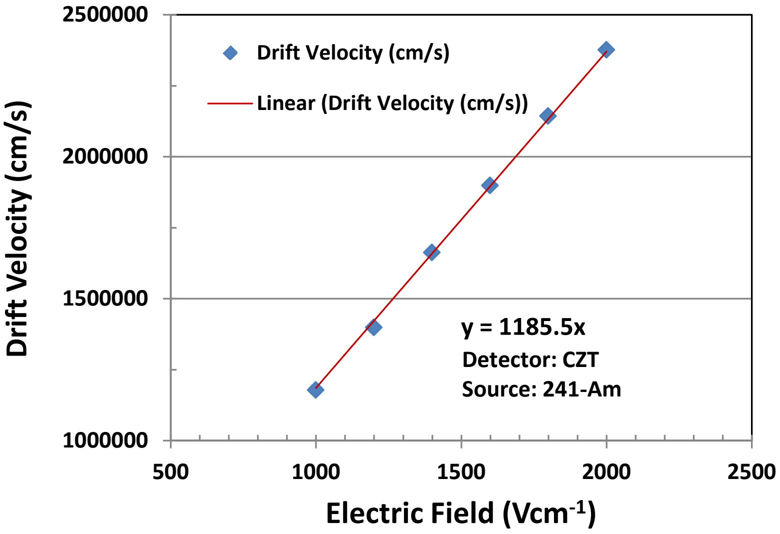

Figure 3.25. Drift velocity vs. Electric field plot for a CZT MSM detector (5 × 5 × 5 mm^3). The slope of the linear fit of the data provides the value for electron mobility.

3.6.4 Mobility-Lifetime Product Measurements

For CZT, the electron mobility-lifetime product ($\mu\tau_e$) is a common measurement used to characterize the charge transport properties of a detector, since it highlights both the electron trapping tendency and electron mobility, both of which are important to radiation detection. The mobility-lifetime product ($\mu\tau_e$) of electron could be determined using Hecht analysis. The charge collection efficiency (CCE) of electrons in a nuclear detector can be related to the $\mu\tau_e$ product using the Hecht equation [79]:

$$CCE = \frac{Q_s}{Q_o} = \frac{\mu\tau_e V}{d^2}\left[1 - exp\left(\frac{-d^2}{\mu\tau_e V}\right)\right] \qquad 3.16$$

where Q_s is the total charge detected, Q_o is the expected total charge, V is the bias voltage, and d is the detector thickness. Hecht equation shows charge collection efficiency is also a function of the applied bias voltage. As higher bias voltage is applied, carriers reaches to collecting electrode more quickly, thereby increasing the charge collection efficiency; as a results the peak positions of the detection signal shift to higher energies.

The electron mobility-lifetime product is measured by irradiating a CZT detector with alpha particles at the cathode, in the same configuration as for drift mobility measurements. After collecting the energy of the photopeaks versus bias voltage, the charge collection efficiency at each bias voltage is calculated by dividing the actual energy by the incident energy for ^{241}Am alpha particles (5.486 MeV). The charge collection efficiencies versus applied bias voltage are plotted, and the resulting values are fit using the single carrier Hecht equation (Equation 3.16) as shown in Figure 3.26. After the curve fitting, the $\mu\tau_e$ of the planar CZT detector was determined to be 5.9×10^{-3} cm^2/V.

The data obtained using various electrical characterizations of planar CZT MSM detector are summarized in the Table 3.3.

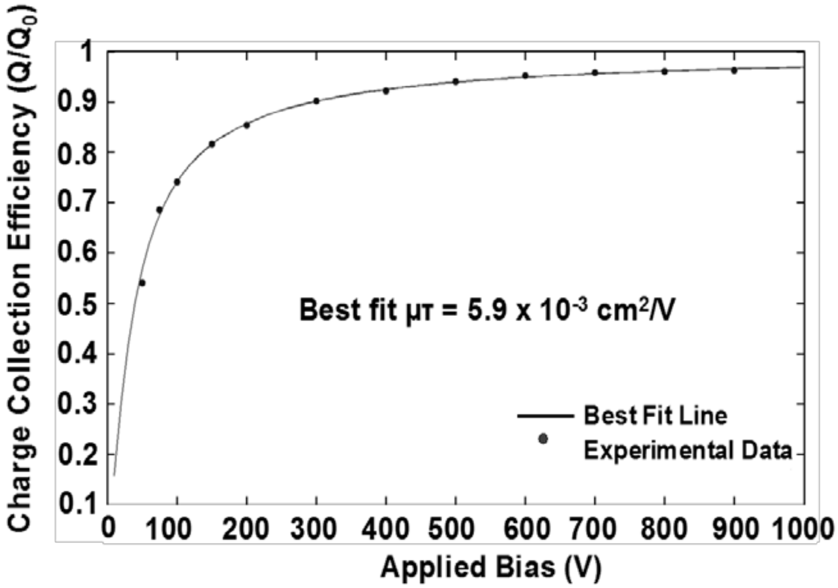

Figure 3.26. Charge collection efficiency versus applied bias voltage plot for a CZT MSM detector (5 × 5 × 5 mm^3). Fitting the data with the Hecht equation gives the value of mobility-lifetime product of electron ($\mu\tau_e$).

Table 3.3. Electrical properties of CZT Detectors

Parameters	**CZT ($Cd_{0.9}Zn_{0.1}Te$)**
Bandgap [eV, 300 K]	1.56
Resistivity [Ω-cm]	6×10^{10}
Leakage Current [nA]	5 (at -1000V)
Electron mobility [cm^2/V.s]	1186
Electron μτ product [cm^2/V]	5.9×10^{-3}

3.7 CZT DETECTOR TESTING USING NUCLEAR RADIATION

In this study, the CZT detectors were developed for detection of gamma radiation from nuclear materials. Gamma radiation has frequencies of above 10^{19} Hz and energies typically above 10 keV. In order to detect gamma radiation, first detector materials absorbs the gamma radiation to produce fast moving electrons within the detector by one of three methods: photoelectric absorption, Compton scattering, and electron-positron pair production [3]. Thus the photon energy of the gamma-ray is converted into electron energy. By applying an external voltage bias, the fast moving electrons can be collected at an electrode (anode), inducing a charge on the contact electrodes of the detector, which is then read out by the front-end detection electronics to provide pulse height spectra (PHS) for the incident radiation. Front-end electronics (Figure 2.23) consist of preamplifiers which converts charge signal to a voltage signal, shaping amplifier which filters noise, and multi-channel analyzers (MCA) which converts analog signals into digital information as pulse height spectrum.

The analog radiation detection experiments are conducted using a Canberra 3106D high voltage supply which biases the CZT radiation detector through an SHV bulkhead. The CZT detector is housed in an aluminum RFI/EMI shielded test box. Inside the box, the detectors are placed either in a PCB holding mount, or one electrode is placed on a gold foil test pad and the other electrode is connected to a pogo-pin contact. Underneath the detector, a ^{241}Am or ^{137}Cs nuclear source is placed to irradiate the detector. ^{241}Am provides low-energy gamma-rays at 59.6 keV or alpha particles at 5.486 MeV, while ^{137}Cs is used for high-energy gamma-rays at 662 keV. Figure 3.27 (a) shows the basic schematic configuration of the electrical connections to the CZT detector. The shielded aluminum test box (Figure 3.27 (b)) is connected to an Amptek A250CF preamplifier through a BNC, which is then connected to an Ortec 671 spectroscopic shaping amplifier. The shaping amplifier is then connected to an oscilloscope and a Canberra Multiport IIe multi-channel analyzer (Figure 3.27 (c)). Data from the multi-channel analyzer is sent to the Genie 2000 PC software, which generates the pulse height spectrum. The radiation detection setup in our laboratory at USC is shown in Figure 3.27.

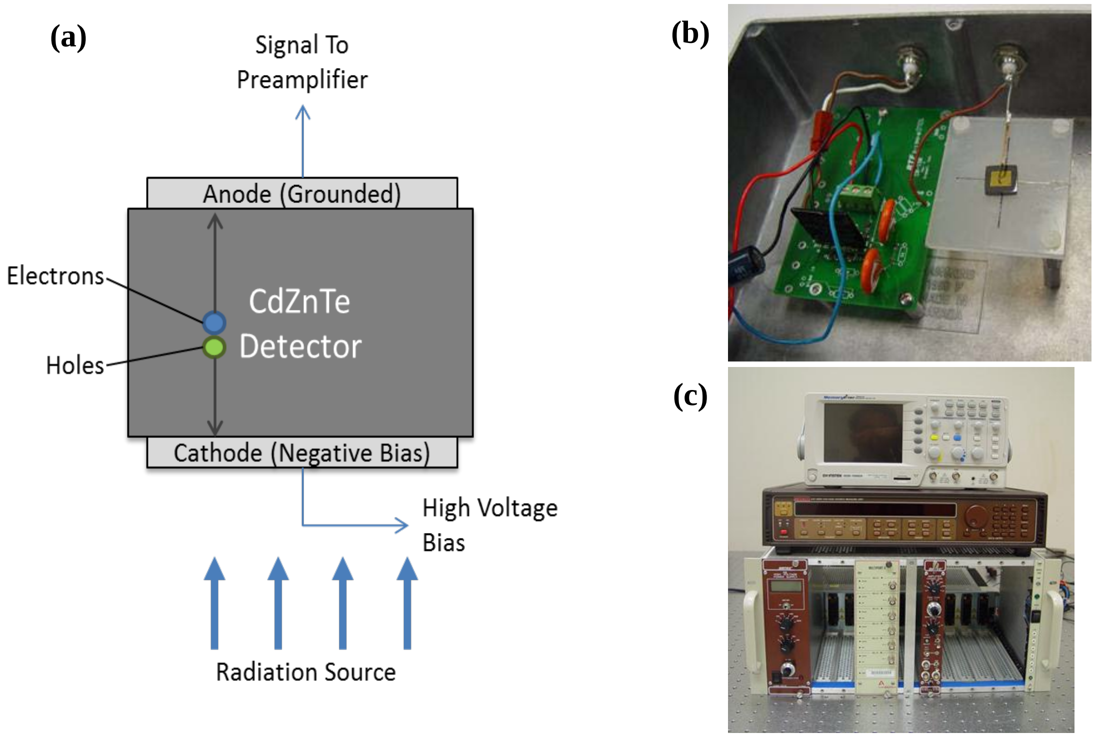

Figure 3.27. (a) Basic connection diagram for a CZT nuclear detector inside of the shielded test box, (b) picture of the shielded aluminum testing box with CZT detector, and (c) picture of the radiation detection system at USC.

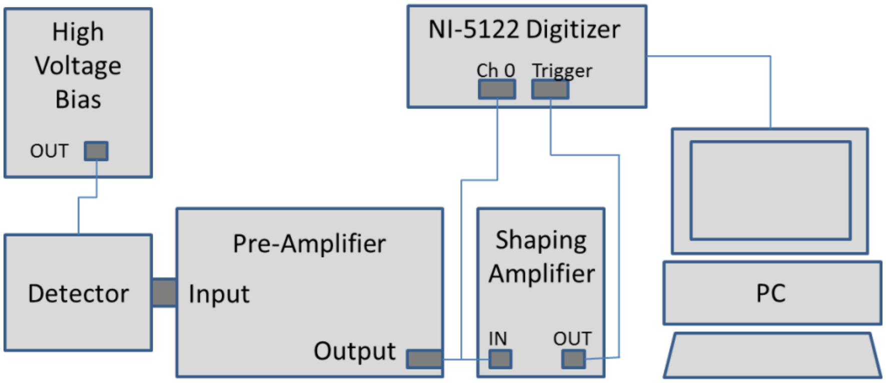

Figure 3.28. Schematic diagram of a digital nuclear detection measurement system at USC.

Once pulse height spectrum was generated, the full width at half maxima (FWHM) of the gamma-ray energy peak was calculated through Gaussian peak fitting using the Origin plotting software. The energy resolution of the detector is calculated by the following equation:

$$\%\, Energy\ Resolution = \frac{FWHM\ (keV)}{Incident\ Energy\ (keV)} * 100\% \tag{3.17}$$

where the incident energy is the centroid of the energy peak observed in the pulse height spectrum. Lower values of energy resolution and FWHM indicate better detector performance.

The planar CZT MSM detector and CZT detector with guard ring were first tested using the ^{241}Am (59.6 keV) source to test its response to low-energy gamma-rays. Figure 3.29 and Figure 3.30 show the resulting pulse height spectrum with ^{241}Am for planar detector and detector with guard ring, respectively. After performing Gaussian peak fitting, the FWHM of the gamma photopeak at ~59.6 keV was calculated to be ~6.2% and 5.8% respectively. Both these detectors clearly detect 59.6 keV energy, however the detector with guard ring showed a much sharper peak. The peaks are more resolved (low noise) due to lower leakage current observed for this detector.

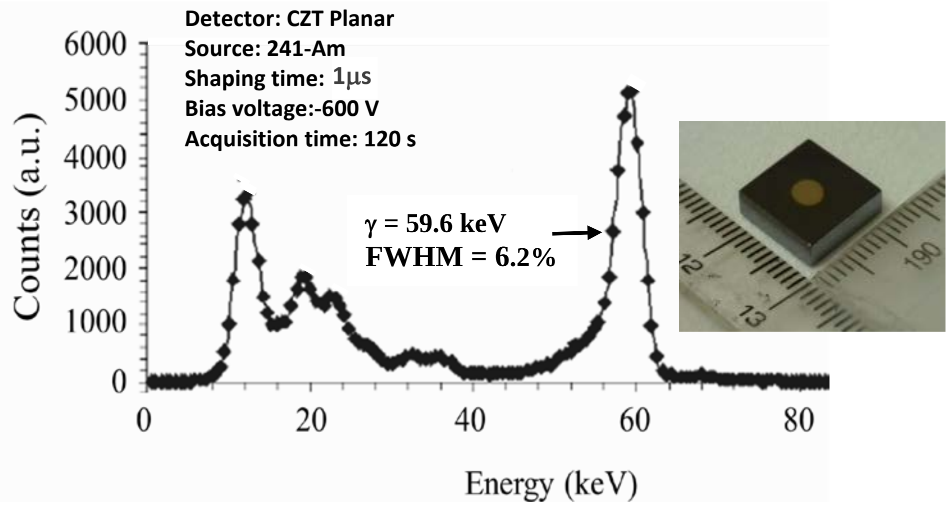

Figure 3.29. Pulse height spectrum (PHS) of the CZT Schottky diode detector with a resolution of 6.2% at 59.6 keV using a ^{241}Am radiation source.

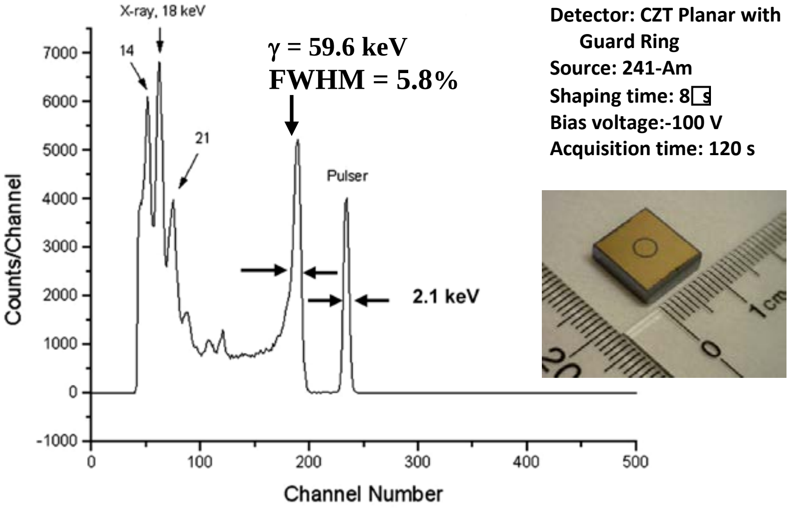

Figure 3.30. Pulse height spectrum (PHS) of the CZT Schottky diode detector with guard ring using a ^{241}Am radiation source. The peaks are more resolved due to lower leakage current (low noise). A resolution of 5.8% at 59.6 keV is observed.

Finally, CZT planar detector with guard ring was tested using ^{137}Cs (662 keV) source to test its response to high-energy gamma-rays. Figure 3.31 shows the resulting pulse height spectrum with ^{137}Cs for planar detector with guard ring. The data shows a sharp 662 keV energy peak. After performing Gaussian peak fitting, the FWHM of the gamma photopeak at 662 keV was calculated to be 2.6%.

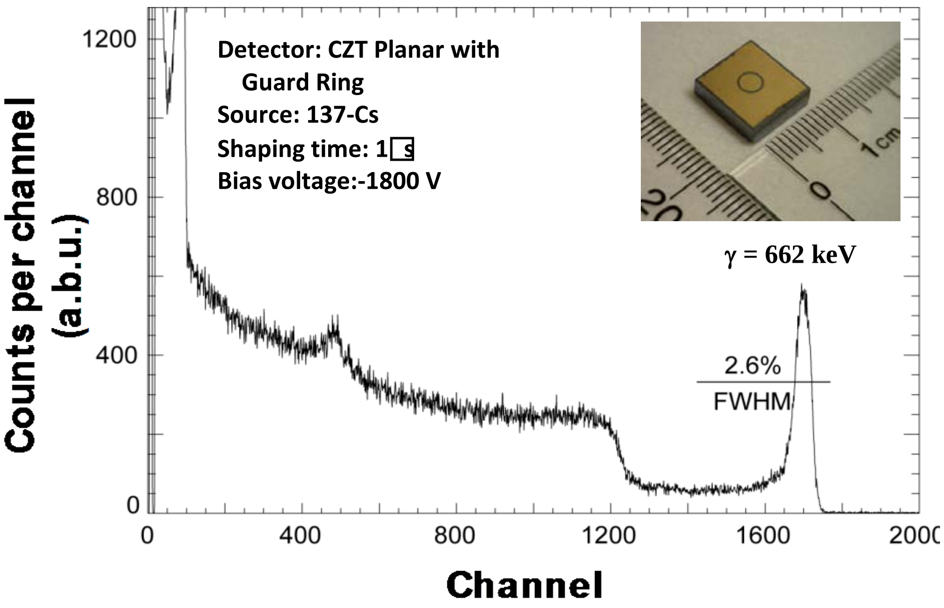

Figure 3.31. Pulse height spectrum obtained for CZT planar detector with guard ring using ^{137}Cs gamma radiation source.

3.8 CONCLUSION

CZT crystal was grown at a stoichiometry of $Cd_{0.9}Zn_{0.1}Te$ from zone refined ultra-pure precursor materials with 50% excess Te using modified multi-pass vertical furnace. The bandgap of the crystals was found to be 1.56 eV, which is in the correct range for detector-grade CZT. Defect analysis was performed on the grown CZT crystals using TSC and EBIC analysis. TSC experiments revealed deep-level defects in the crystal which contribute to hole trapping. EBIC results showed that clusters of dislocations and point defects within the bulk of the CZT crystals due to Te segregation. These results give insight on the type and severity of defects present within the solution-growth CZT crystals, which may assist in reducing defects present in future crystal growths.

The electrical resistivity was estimated to be 6×10^{10} Ω-cm, which is high enough to fabricate a functional CZT radiation detector. The CZT detectors showed very low leakage current at a high bias (<5 nA at –1000V) due to their high resistivity, which are beneficial for high resolution detectors. The drift mobility and mobility-lifetime product of electrons were estimated to be 1186 cm^2/Vs and 5.9×10^{-3} cm^2/V, respectively. These data provides an insight on the potential performance of the CZT nuclear detectors, and ensures that only the best samples are chosen to be fabricated into detectors.

Finally, CZT detectors were tested with gamma-ray irradiation. An energy resolution of 6.2% was obtained for CZT planar detector when irradiated with 59.6 keV low-energy gamma radiations (^{241}Am). The peaks were sharper and better resolution of 5.8% was observed for the CZT detector with guard ring with 59.6 keV radiation. An energy radiation of 2.6 % was observed for detector with guard-ring structure irradiated with high energy 662 keV gamma radiations using ^{137}Cs source.

CHAPTER 4: SILICON CARBIDE FOR ALPHA DETECTOR

4.1 OVERVIEW

Silicon carbide based high resolution radiation detectors for nuclear isotope identification and gamma- and x-ray imaging have recently attracted high attention. Unique properties of SiC make it an appealing candidate for its use in high-temperature and high radiation background with hot and humid environments, under which conventional semiconductor detectors (e.g., CZT, Si, Ge, etc.) cannot adequately perform [11, 79, 80, 81]. Due to favorable material properties of SiC such as wide band-gap (3.27 eV at 300 K), high radiation hardness and breakdown field, SiC detectors are expected to be compact, light-weight, and capable of operating long periods of consistent room-temperature and above operation. These properties are very important in a wide range of applications including radiation detectors, medical imaging, national security, environmental safety, space applications, and high energy astrophysics or astronomy.

In general, two types of SiC radiation detectors have been developed in our laboratory at USC and also by other research group: (a) diode-type detectors fabricated using SiC epitaxial layers [82, 83, 84, 85], and (b) bulk detectors utilizing semi-insulating (SI) SiC [79, 82, 84, 86]. Although diode-type detectors perform well in high-resolution detection of low penetration depth radiation (i.e. alpha, beta, low energy gamma rays, and soft x-rays), the unavailability of high quality thick low doped epitaxial films limit the application of the diode-type SiC detectors in the detection of high energy x-rays and gamma rays [11, 79, 84, 85]. Available epitaxially grown SiC layers have a maximum thickness in the order of 150 μm with a residual n-type doping ~ 10^{14} cm^{-3} that limits the depth of the depletion layer (detector's active region) to less than 100 μm at reasonable bias voltages [11, 79, 84, 85]. Bulk SI SiC available in the market with thicknesses up to 400 μm have shown very high defect densities and high impurity concentrations, which prevents its use as a high energy x- and gamma-ray detector [11, 79, 84, 85, 86]. However, recently, high-purity SI 4H-SiC wafers have become commercially available with low residual impurities corresponding to background net doping concentrations less than 10^{15} cm^{-3}. In addition, recent achievements in characterizing, passivating deep levels, and edge termination and isochronal annealing of SiC epitaxial films [87, 88, 89, 90, 91] have resulted in a significant increase of the charge collection efficiency, energy resolution, and performance of 4H-SiC epitaxial radiation detectors.

This chapter describes fabrication and performance of radiation detectors based 4H-SiC n-type epilayer. First, radiation detectors were fabricated using low-leakage current and low-defect bearing 4H-SiC n-type epilayer on high-purity 4H-SiC wafers. Detail defect characterization using deep level transient spectroscopy (DLTS) and electrical characterizations using current-voltage and capacitance-voltage measurements were carried out for semi-insulating (SI) high purity n-type 4H-SiC epitaxial layers. A systematic study was conducted to evaluate performance of 4H-SiC n-type epilayer detectors as alpha particle and low energy gamma radiation detectors.

4.2 SiC POLYTYPES AND CRYSTAL GROWTH

Silicon carbide (SiC) crystal lattice is structured from closely packed silicon-carbon bilayers, which can be viewed as a planar sheet of silicon atoms coupled with a planar sheet of carbon atoms. Due to the sequential variation of the stacked bilayers, SiC has many crystal structures such as cubic, hexagonal, and rhombohedral symmetry. These different structures of SiC are known as polytypes. The different layers are usually designated by the letter A, B, and C. To specify the crystal lattice structure of the polytype, alphabetical letters "C" is used for cubic structure, "H" is used for hexagonal structure, and "R" is used for rhombohedral structure [92]. The repetition number of bilayers in the stacking sequence is expressed by an integer number. For example, in 4H-SiC four layers (ABAC) are repeated in the stacking sequence, and it has hexagonal symmetry; hence it is known as 4H polytype. Due to the variation in the stacking sequence, different polytypes have significantly different optical and electrical properties such as band-gap, drift velocity, breakdown electric field strength, and the impurity ionization energies [93, 94, 95]. Among different polytypes, 4H-SiC is usually preferred for electronic devices due to its better charge transport properties, specifically high electron mobility [96, 97, 98]. This polytype has wurtzite structure with 50% cubic and 50% hexagonal lattice sites. Figure 4.1 shows crystal structure of 4H-SiC.

The SiC based electronic and optoelectronic device performances highly depend upon the bulk crystal and epitaxial growth technology. SiC does not show a liquid phase and the only way to grow, synthesize, and purify silicon carbide is by means of gaseous phases. For the growth of electronic-grade silicon carbide, the most common techniques are physical vapor transport (PVT), where a solid pre-synthesized silicon carbide is evaporated at high temperatures and the vapors then crystallize at a colder part of the reactor, and chemical vapor deposition (CVD), where gas-phase silicon and carbon containing precursors react in a reactor and silicon carbide is solidified on a target. Nuclear detectors cannot be fabricated directly on the bulk SiC because of low crystal quality. Therefore, higher crystalline quality SiC epitaxial layers are grown on bulk SiC. The growth of the epilayers are generally more controllable and reproducible than growth of the bulk SiC wafers. There are several growth techniques for SiC epitaxial layers including liquid phase epitaxy (LPE), molecular beam epitaxy (MBE), and chemical vapor deposition (CVD).

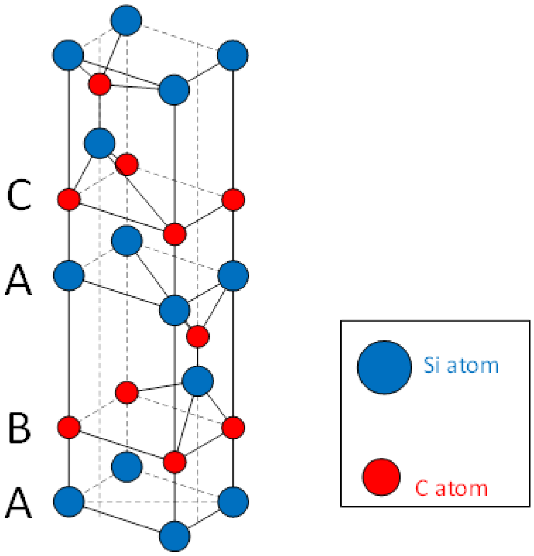

Figure 4.1. Structure of 4H-SiC polytype.

The n-type 4H-SiC and semi-insulating (SI) epitaxial layers were grown on 8 × 8 mm^2 highly doped by nitrogen 4H-SiC (0001) substrates, 4 - 8^o offcut towards $[11\bar{2}0]$ direction. The epitaxial growth was carried out in a hot-wall CVD system. Dichlorosilane (SiH_2Cl_2, DCS) and propane (C_3H_8) were used as the precursors and hydrogen of 6 slm was employed as the carrier gas. The dilution ratio during growth was ~ 1000. The flow rates of dichlorosilane and propane were maintained to obtain C/Si ratio of 1.28 and 1.66 for n-type and SI epi, respectively. Before growth, in-situ hydrogen etching was performed at 1550 °C for 5 – 20 min. The growth temperature and pressure were 1550 °C and 80 - 120 torr, respectively. No intentional dopants were used during growth of semi-insulating epitaxial layer. The thicknesses of the n-type and SI epitaxial layers were ~ 20 - 50 μm and 10 - 50 μm, respectively. The net doping concentration of the n-type epitaxial layer measured using high frequency (100 kHz) capacitance-voltage (C-V) method was found to be 2 - 5×10^{14} cm^{-3}. The annular mercury probe with 0.5 mm diameter contact (MSI electronics, model Hg-402) was used for C-V measurements. The high frequency capacitance of the SI epi was very low (2 - 8 pF) and remained practically constant with applied bias indicating semi-insulating nature of the epitaxial layer. The transmission line method (TLM) measurement performed on the grown epitaxial layers confirmed semi-insulating properties. Figure 4.2 shows a picture of 50 mm n-type 4H-SiC epitaxial layer wafer.

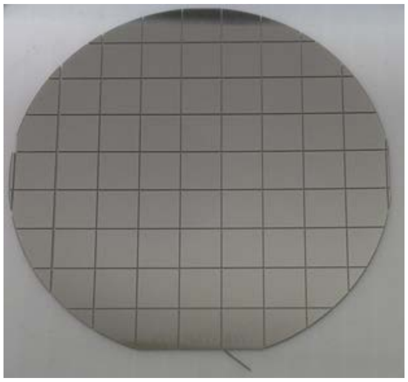

Figure 4.2. Photograph of a 50 mm n-type 4H-SiC epitaxial layer wafer.

4.3 FABRICATION OF 4H-SIC DETECTOR

The performance of nuclear detector greatly depends on the careful fabrication of detector devices, which involve wafer dicing, cleaning, surface polishing, surface passivation, and metal contact deposition. For detector fabrication, 50 μm thick n-type epitaxial layer grown on a 50 mm diameter 4H-SiC (0001) wafer (shown in Figure 4.2) was used. The substrate was highly doped with nitrogen and 8^o off-cut towards the $[11\bar{2}0]$ direction. The net doping concentration of the epitaxial layer measured using high frequency (100 kHz) capacitance - voltage (C-V) method was found to be 2.4×10^{14} cm^{-3}. A micropipe defect density less than 5 cm^{-2} has been calculated using scanning electron microscopy on a sister sample.

The radiation detectors were fabricated on the Si-face of 8 × 8 mm^2 substrates diced from the 50 μm diameter wafer. Ni Schottky contact (3.8 mm diameter circular shape) with an area of ~ 11.34 mm^2 and thickness of ~ 10 nm was deposited on top of the epitaxial layers through the shadow mask using a Quorum model Q150T sputtering unit. Large Ni contact (~ 6 × 6 mm^2) 100 nm in thickness was deposited on the opposite surface (C-face) for the back contact. Standard RCA cleaning procedure of the wafer was carried out prior to the contact deposition. This process starts with the removal of organic contaminants (dust particles, grease, etc.) from the wafer surface by using solvents (trichloroethylene, acetone, and methanol) at a temperature of 70 °C. Any organic residue left by the first step is then processed using sulfuric acid and ammonium hydroxide solutions (with hydrogen peroxide). These solutions are designed to attack the organic impurities by dehydration process and oxidation of the carbon present at the surface of the wafer. Finally, these oxide layers were etched with hydrofluoric acid (HF).

Figure 4.3 shows the cross-sectional schematic of the diced 8 × 8 mm^2 4H-SiC epilayer, 4H-SiC buffer epilayer, and 4H-SiC bulk substrate with circular Ni-deposited on the epilayer face (Si-face) and larger Ni contact on the opposite site (C-face). After fabrication, the detector was then mounted on a printed circuit board (PCB) and wire bonded for proper electrical connection. Figure 4.4 shows an n-type 4H-SiC wafer with Ni deposited on the epilayer Si-face and a photograph of the detector mounted on a PCB and wire bonded for proper electrical connection. The wire-bonding was done using very thin (25 μm) gold wire to ensure less scattering and obscuration of the alpha particles from the wire-bond region. The PCBs were fitted with board-to-board connector pins in order to obtain plug-in modular configuration for stable electrical connections as shown in Figure 4.4 (b).

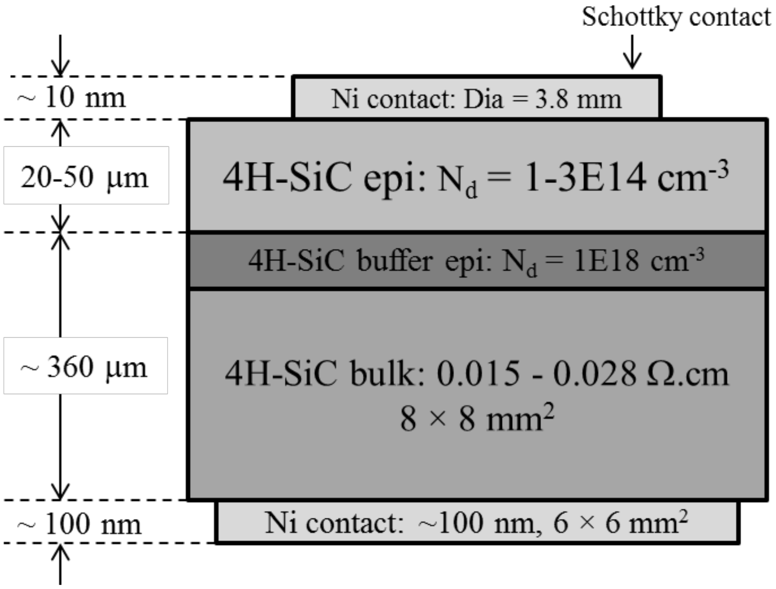

Figure 4.3. Cross-sectional view of a fabricated Schottky barrier detector on n-type 4H-SiC epitaxial layer.

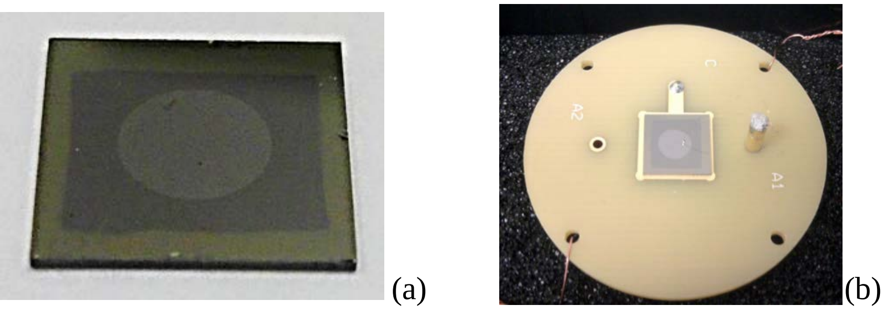

Figure 4.4. (a) Photograph of a center aligned 4H-SiC epitaxial Schottky barrier detector with nickel contact diameter = 3.8 mm. (b) A detector mounted on a PCB and wire bonded for proper electrical connection.

4.4 ELECTRICAL CHARACTERIZATION OF 4H-SIC DETECTOR

4.4.1 Current-Voltage Measurements

Current-voltage (I-V) measurements were carried out on the fabricated detectors using a Keithley 237 source meter to investigate the electrical properties of the metal-semiconductor contact. Figure 4.5 shows the schematic of the setup used to perform the I-V measurements and Figure 4.6 shows the picture of that system. The I-V characterizations were performed at room temperature using forward, as well as reverse voltage bias applied across the 4H-SiC detector. The forward-biased response was used to study the behavior of the Schottky contacts in terms of barrier height and the diode ideality factor using the thermionic emission model [42]. The reverse I-V characteristics give the magnitude of the leakage current under operating conditions.

As per thermionic emission model, the voltage dependent junction current in a Schottky contact can be expressed as:

$$I = I_s(e^{\frac{\beta V}{n}} - 1) \qquad 4.1$$

where I_S is the saturation current, V is the applied voltage, n is the diode ideality factor, $\beta = q/k_BT$, q being the electronic charge, k_B the Boltzmann constant (8.62×10^{-5} eV/K), and T is the absolute temperature (°K). Using logarithm, the Equation 4.1could be written as:

$$log(I) = \frac{\beta V}{n} + log(I_s) \qquad 4.2$$

Therefore, using current measurements at varying applied voltage and then plotting log(I) versus applied voltage bias, the ideality factor 'n' could be measured from the slope and saturation current I_s from the intercept. The saturation current, I_s, is given by:

$$I_s = A^*AT^2\left(e^{-\beta\varphi_B}\right) \qquad 4.3$$

where A^* is the effective Richardson constant (146 $\text{Acm}^{-2}\text{K}^{-2}$ for 4H-SiC), A is the area of the diode, φ_B is the Schottky barrier height.

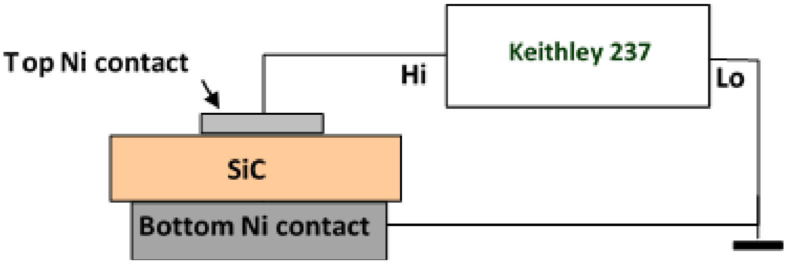

Figure 4.5. Schematic of the electrical circuit diagram for I-V measurements of 4H-SiC detector using Keithley 237.

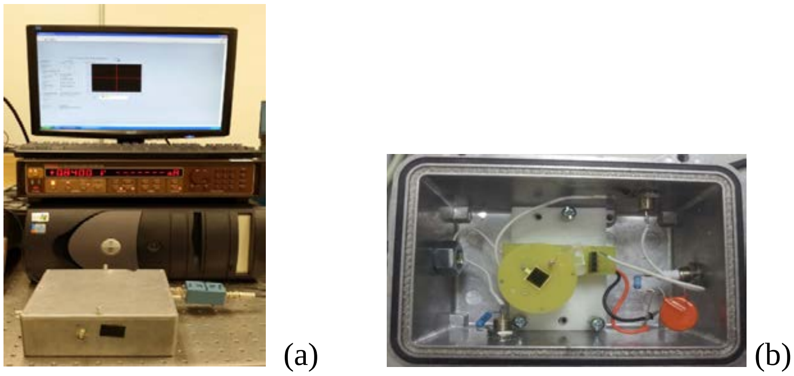

Figure 4.6. (a) Photograph of the experimental setup for the electrical characterization measurements. (b) The detector is mounted inside the aluminum box.

Figure 4.7 shows I-V characteristics of the detector at forward and reverse bias. The room temperature, reverse bias leakage current was found to be ~ 0.78 nA at a bias voltage of −250 V and ~ 0.15 nA at −100 V. By plotting log of observed current, *log(I)*, versus applied voltage bias, the diode ideality factor of 1.4 was measured from the slope as per the Equation 4.2. The intercept of the above plot provided the data for the saturation current, which was used to calculate the barrier height using Equation 4.2. The barrier height for Ni/4H-SiC Schottky contact was found to be 1.38 eV. The barrier height thus calculated depends on the spatial homogeneity of the Schottky barrier height [99]. However, an ideality factor greater than unity as observed from I-V measurements, indicates non-uniformity in the surface barrier height, which in turn indicates the possibility of the presence of traps in the depletion region [100].

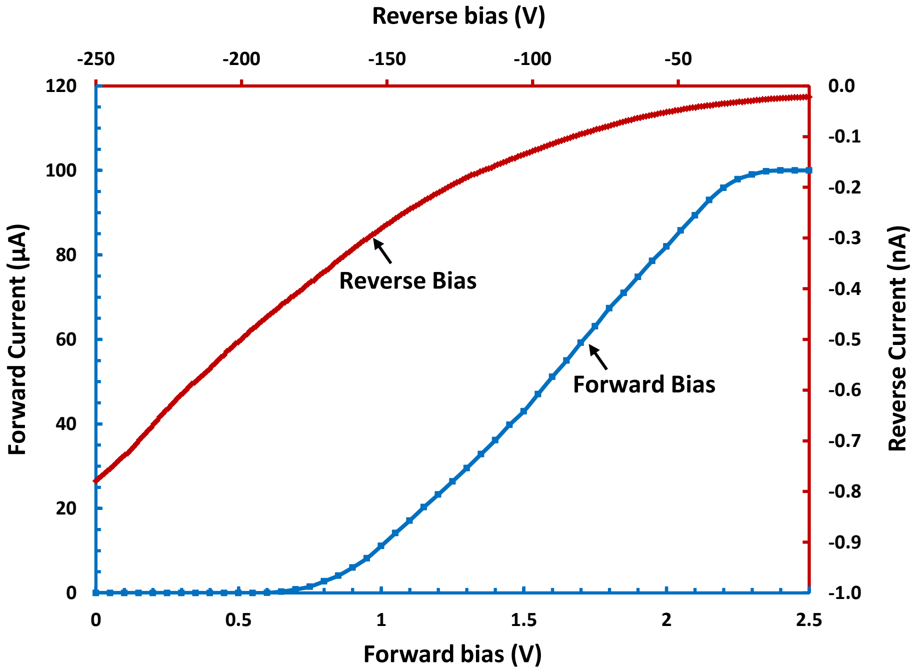

Figure 4.7. Forward and reverse I-V characteristics at 300 K for a Schottky barrier detector fabricated on n-type 4H-SiC epilayer. At reverse bias of ~ -250V: very low leakage current (< 1 nA) was observed; from forward bias, ideality factor is derived to be ~1.4.

4.4.2 Capacitance-Voltage Measurements

Capacitance-voltage (C-V) measurements were carried out using a Keithley 590 CV analyzer at a frequency of 100 kHz (Figure 4.6) at room temperature. The C-V measurements of the Schottky (or p-n) junction relies on the fact that the junction capacitance is a function of depletion region width at the semiconductor junction (Equation 3.11), which in turn depends upon the applied voltage and effective doping concentration (Equation 3.12). These relationships can be expressed as:

$$C = \varepsilon\varepsilon_0 A \Big/ \left(\frac{2\varepsilon\varepsilon_0 \times (V_{bi} - V)}{qN_d}\right)^{1/2} \qquad 4.4$$

where the symbols have their usual meaning as explained in Section 3.6.2. The above equation could be written as below:

$$\frac{1}{C^2} = \frac{2V_{bi}}{q\varepsilon\varepsilon_0 A^2 N_d} + \frac{2V}{q\varepsilon\varepsilon_0 A^2 N_d} \qquad 4.5$$

which is a straight line equation when $1/C^2$ is plotted against applied voltage bias, V. Form the slope of this linear equation doping concentration (N_d) could be determined, and from the intercept of the linear fit built-in voltage (V_{bi}) could be estimated using following equation where A is the area, q is the electronic charge, ε_0 is permittivity of vacuum and ε_{SiC} is the dielectric constant of 4H-SiC.

$$N_d = 2/q\varepsilon_{SiC}\varepsilon_0 A^2 \times slope \qquad 4.6$$

Figure 4.8 shows a $1/C^2$ vs V plot obtained for the n-type 4H-SiC epitaxial Schottky detector at 300 K. A linear fit to the curve gives an effective doping concentration of 2.4×10^{14} cm^{-3} and a built-in potential (V_{bi}) of 1.44 V. The barrier-height (ϕ_B) was also calculated to be 1.52 eV, using the equations given below.

$$\phi_{B(C-V)} = V_{bi} + V_n \qquad 4.7$$

where, V_n is the potential difference between the Fermi level energy and the bottom of the conduction band in the neutral region of the semiconductor and is given by:

$$V_n = kTln\frac{N_C}{N_D} \qquad 4.8$$

where N_C is the effective density of states in the conduction band of 4H-SiC and is taken equal to 1.6×10^{19} cm^{-3} [101].

The barrier height calculated from the C-V measurements is slightly higher than that obtained from the forward I-V characteristics. The value of barrier-height obtained from forward I-V characteristics is dominated by low Schottky barrier-height locations in an inhomogeneous diode. However, C-V characteristic gives an average value of the barrier height for the whole diode [102]. So, the barrier-height thus calculated from C-V characteristics is slightly higher than that determined by I-V characteristics. Hence, the larger value of barrier height calculated from the C-V measurements further confirms the inhomogeneity of the surface barrier height.

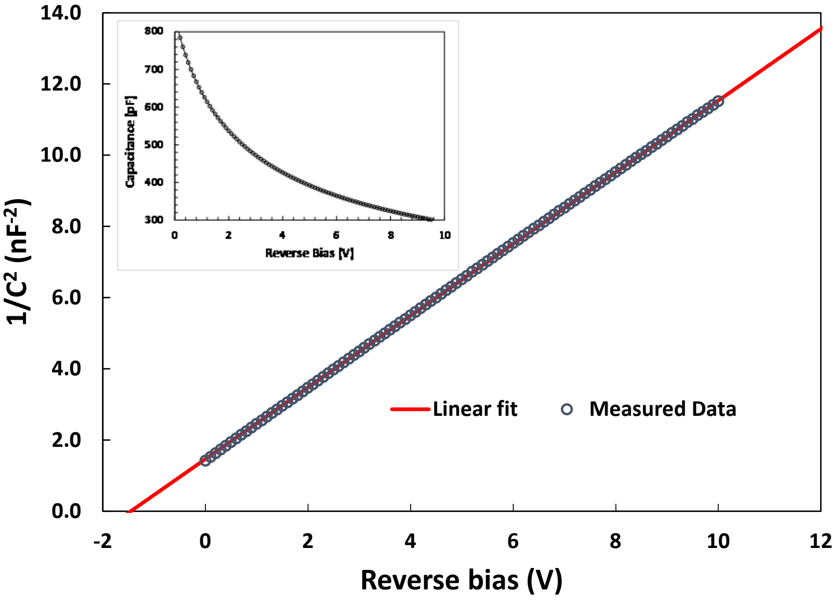

Figure 4.8. Mott-Schottky plot ($1/C^2$ vs. V plot) of n-type 4H-SiC epitaxial Schottky detector at 300 K. Inset shows original C-V characteristic. Doping concentration was measured from the slope of the linear fit and using the formula shown to be 2.4×10^{14} cm^{-3}. A is the area, e is the electronic charge, ε_0 is permittivity of vacuum and ε_{SiC} is the dielectric constant of 4H-SiC.

4.5 DEFECT STUDY BY DEEP LEVEL TRANSIENT SPECTROSCOPY

Intrinsic defects, such as grain boundaries and dislocations, impurity related point defects or complexes have been reported in as-grown SiC epilayers [88, 103]. Many of these defects are electrically active and can lead to increased detector leakage current and poor carrier lifetime and mobility by acting as trap or recombination/generation centers. The electrically active defects may lead to charge loss or detector output pulse with large rise times leading to incomplete charge collection. Therefore, it is very important to identify the electrically active defects in the epilayer and evaluate their role in affecting the ultimate detector performance.

4.5.1 DLTS Setup

Deep level transient spectroscopy (DLTS) is a very sensitive technique for the identification of defect related parameters such as energy level, trap concentration, capture cross-section, and spatial profile in semiconductors [104]. The activation energy gives the exact position of a deep level in the band-gap in respect to conduction and valence band. The trap concentration is defined as the amount of a particular deep level in the band-gap of the semiconductor. This parameter helps to determine the extent of the role defects have on device performance. The capture cross-section provides information about the electron and hole capture rates, from which it can be determined if the deep level defects may act as a trapping, recombination, or generation center.

DLTS measures the change in junction capacitance of the Schottky detector due to the emission of charge carriers from the defects existing in the space charge region. A capacitance-DLTS (C-DLTS) spectrum is generated from the temperature dependent capacitance transients followed by a saturated trap filling pulse applied to a semiconductor junction. The defect concentration, N_t, capture cross cross-sections, $\sigma_{n,}$ and the activation energies, ΔE, are extracted by analyzing the capacitance transients.

In a capacitance DLTS mode, the system relaxes into equilibrium by thermally emitting the trapped charges after the termination of the filling pulse resulting in capacitance transients. The thermally activated emission rate can be expressed as:

$$e_n = (\sigma_n \langle V_{th} \rangle N_C/g) exp(-\Delta E/kT) \qquad 4.9$$

where σ_n is the carrier capture cross section, $\langle V_{th} \rangle$ is the mean thermal velocity, N_C is the effective density of states, g is the degeneracy of the trap level and is considered to be equal to 1 in the present calculations and ΔE the energy separation between the trap level and the carrier band. The emission rate is related to the capacitance transient by the following relationship:

$$C(t) = C_o + \Delta C \exp(-te_n) \qquad 4.10$$

where C_0 is the junction capacitance at steady-state reverse bias voltage, ΔC is the difference in capacitance change measured within the rate window. The trap concentration N_t was calculated using the following expression:

$$N_t = 2\left({}^{\Delta C(0)}\!/_{C} \right) N_d \qquad 4.11$$

where $\Delta C(0)$ is the difference in capacitance change between the two edges of the filling pulse and N_d is doping concentration. The rate windows were defined by an initial delay which is actually a delay set for the emission rate calculations following the termination of the filling pulse. The initial delay is related to the rate window τ as follows:

$$Initial\ delay\ (ms) = {}^{1}\!/_{(4.3 \times \tau)} \tag{4.12}$$

DLTS peaks corresponding to different traps appear as a function of temperature. Signals from different defect levels can be resolved in a single DLTS scan. The peak position in DLTS spectroscopy depends on the rate window. A larger rate window will shift a defect peak to higher temperature and a smaller rate window will shift a defect peak to lower temperatures. The DLTS has the ability to set rate windows, and a series of spectra can be produced by using different rate windows as shown in Figure 4.9.

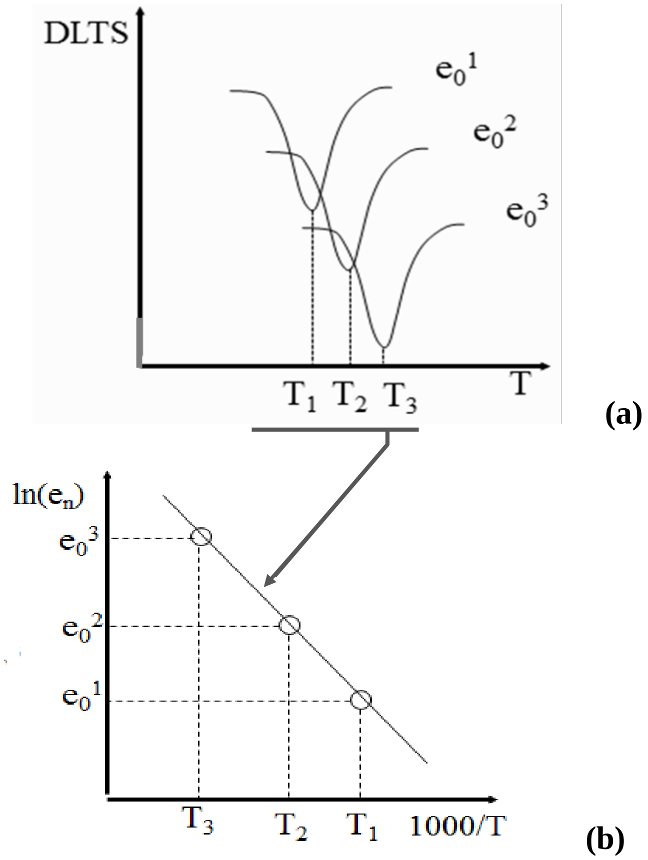

Figure 4.9. (a) The DLTS spectra corresponding to a trap center at various rate windows and (b) the corresponding Arrhenius plots obtained from the spectra.

4.5.2 DLTS Data for 4H-SiC Epitaxial Detector

For defect characterization in 4H-SiC epitaxial Schottky barrier detector, a SULA DDS-12 modular DLTS system was used in a capacitance mode. The DLTS system is comprised of a pulse generator, a capacitance meter, a correlator module, and a PC based data acquisition and analysis software. The block diagram and a photograph of the DLTS system are presented in Figure 4.10 and Figure 4.11, respectively. The correlator module uses a modified double boxcar signal averaging algorithm. It automatically removes DC background from the capacitance signals and measures the capacitance transient in a given rate window. The correlator unit is capable of assigning four simultaneous rate windows in a single thermal scan. For sample temperature variation, the detectors are mounted in a Janis VPF 800 LN_2 cryostat controlled by a Lakeshore LS335 temperature controller. Temperature scans ranging from 80 - 800 K are selected for a single run at a heating rate of 0.05 Ks^{-1}.

The DLTS measurements were carried out in a temperature range of 80 - 850 K with a steady-state reverse bias of -2 V. The pulsing was done to 0 V from the steady-state reverse bias to fill/populate the majority carrier traps present within the steady state depletion width. A pulse width of 1 ms was chosen in order to ensure saturation trap filling. Figure 4.12 shows representative DLTS spectra in the temperature range of 80 to 140 K using a smaller set of initial delays, and 100 to 800 K using a larger set of initial delays respectively. The peaks appeared at different temperatures corresponding to different defect levels. In total, six distinct peaks were observed in the entire temperature scan range of 80 - 800 K and are numbered as Peak #1 to #6. The negative peaks indicate that the detected traps are majority carrier traps (electron traps in this case). The activation energy was calculated from the Arrhenius plots ($T^2/e_n\, vs\ 1000/T$). Figure 4.13 shows the Arrhenius plot for all the peaks obtained from the DLTS scans. The defect parameters were extracted from the DLTS scans using the equations described in and is summarized in Table 4.1.

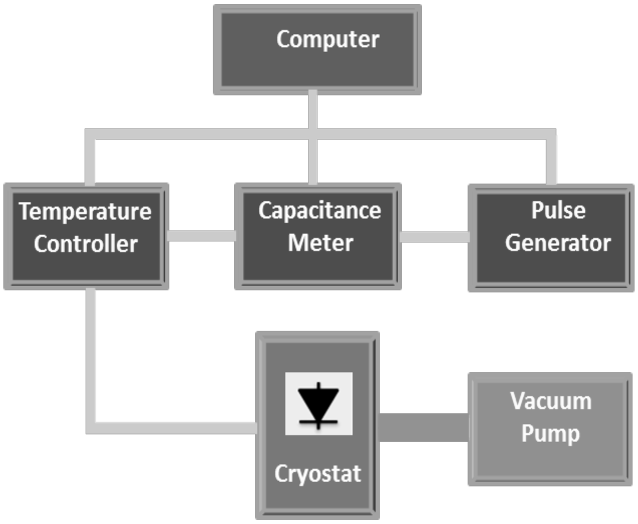

Figure 4.10. Block-Diagram of the SULA DDS-12 DLTS setup.

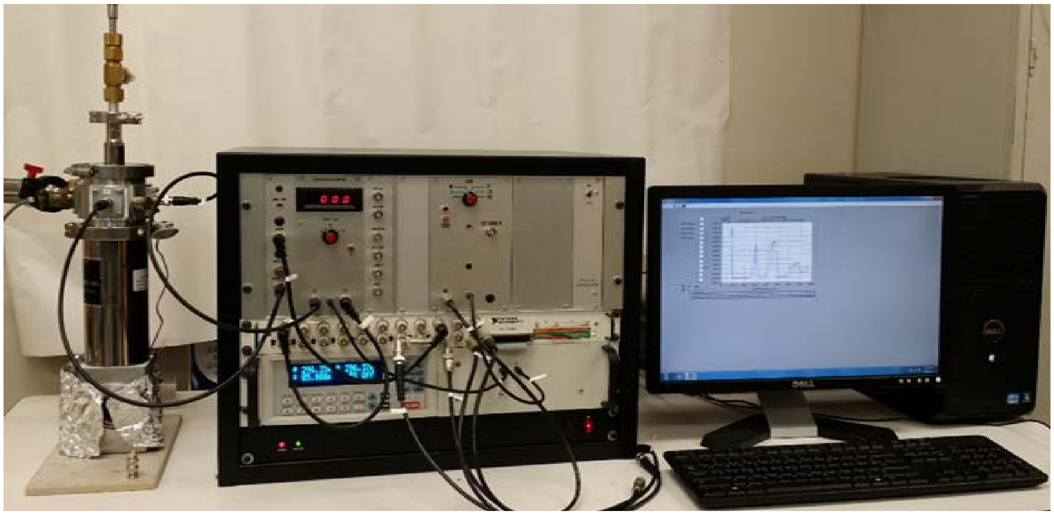

Figure 4.11. Photograph of the SULA DDS-12 DLTS measurement system.

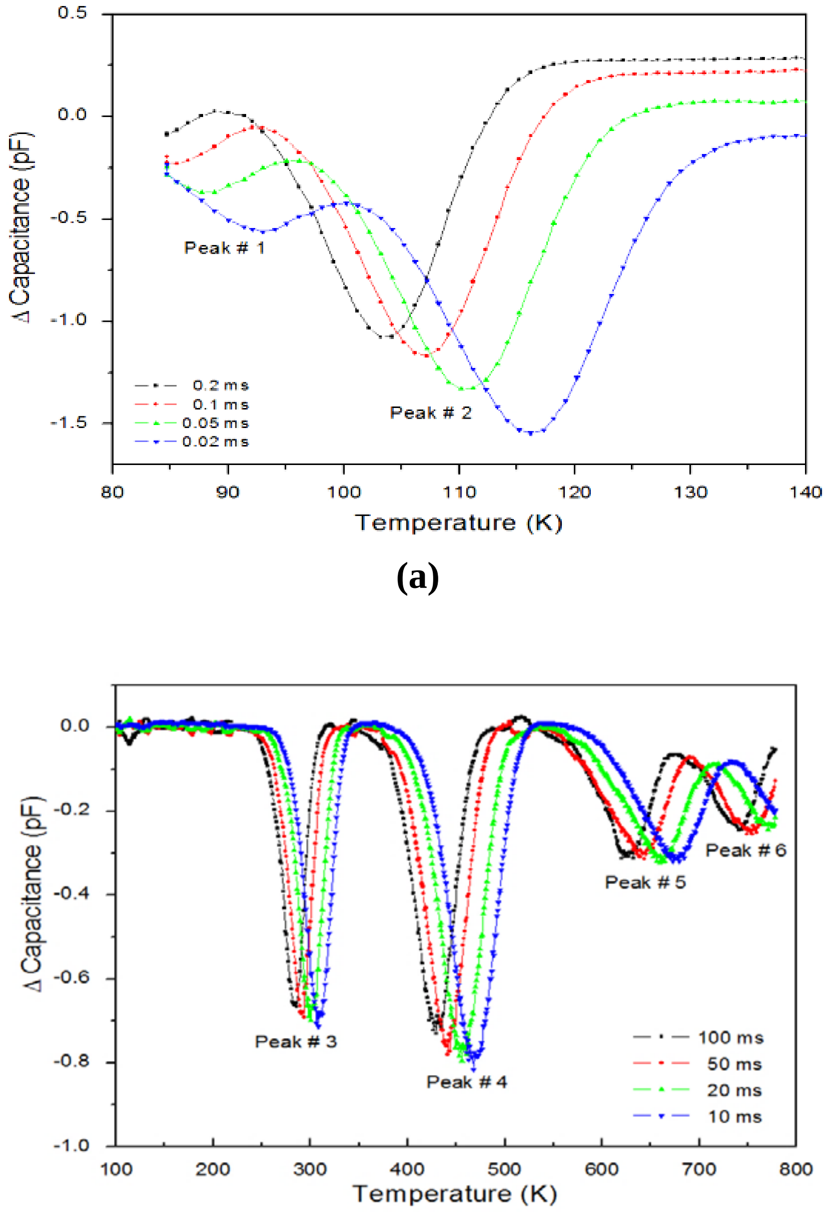

(a)

(b)

Figure 4.12. Representative DLTS spectra obtained using 50 mm n-type Ni/4H-SiC epitaxial detector in the temperature range of: (a) 80 to 140 K using a smaller set of initial delays, and (b) 100 to 800 K using a larger set of initial delays.

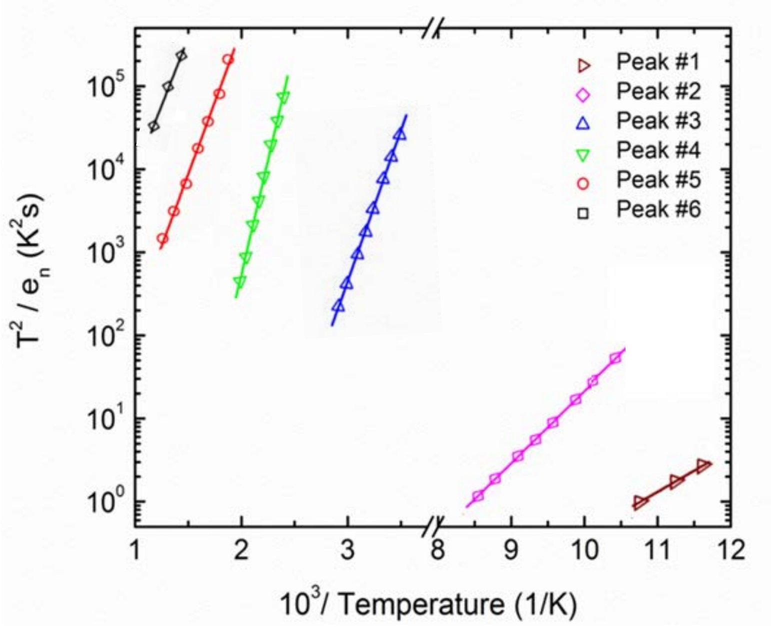

Figure 4.13. Arrhenius plot for all the peaks obtained from the DLTS scans.

Table 4.1. Defect parameters obtained from the DLTS measurements

Peak #	**σ_n cm^2**	**ΔE ev**	**N_t cm^{-3}**	**Possible Trap Identity**	**References**
Peak 1	4.08×10^{-15}	$E_c - 0.11$	1.5×10^{13}	Ti(h)	[105, 106, 107, 108]
Peak 2	2.52×10^{-15}	$E_c - 0.17$	3.4×10^{13}	Ti(c)	[105, 106, 107, 108]
Peak 3	$3.42\ 10^{-15}$	$E_c - 0.68$	1.6×10^{13}	$Z_{1/2}$	[106, 109, 110, 111, 112,113]
Peak 4	3.78×10^{-15}	$E_c - 1.06$	2.2×10^{13}	EH_5	[111, 114,115]
Peak 5	3.17×10^{-17}	$E_c - 1.32$	7.8×10^{12}	Ci1	[114]
Peak 6	1.59×10^{-11}	$E_c - 2.42$	5.4×10^{12}	Unidentified	

Using deep level transient measurements, six different defect centers (DLTS peaks) were detected in a temperature scan range of 80 - 800 K. The trap levels corresponding to Peak #1 and Peak #2 were found to be located at E_c - 0.11 eV and E_c - 0.17 respectively, where E_c is the conduction band minimum. Both these shallow level defects have been identified in the literature as titanium substitutional impurities in the Si sites. Similar defect levels located at E_c - (0.117 ± 0.008) eV and E_c - (0.160 ± 0.010) eV were reported from DLTS studies of Ti^+ implanted 4H-SiC which were attributed to the ionized titanium acceptor Ti^{3+} ($3d^1$) residing at hexagonal and cubic Si lattice, respectively [105, 106]. Other research group also assigned defect level located at E_c - 0.16 eV as Ti electron trap [107], and trap level located at E_c - 0.17 eV as chromium or titanium impurities (acceptor like) in hexagonal position [108].

The trap center related to Peak #3 was found to be located at 0.68 eV below the conduction band edge. Several groups have reported the presence of a similar defect level often designated as $Z_{1/2}$ [109, 110]. However, the exact microscopic structure is still unknown and several theories exist in the literature regarding the probable structure of $Z_{1/2}$ centers. As summarized in [107], $Z_{1/2}$ is most likely related to defect complexes involving equal number of carbon and silicon sites. The possible structures are silicon and carbon vacancy complexes (V_{Si}+V_C), antisite complexes (Si_C+C_{Si}) pairs, or a pair of an antisite and a vacancy of different atoms [107, 109, 111]. On the contrary, other researchers reported that the participation of carbon interstitial with nitrogen form defect levels with similar activation energy [112]. $Z_{1/2}$ center is also reported to be responsible for the reduction of carrier lifetime [106, 113]. The concentration of the $Z_{1/2}$ defects was found to be 1.6×10^{13} cm^{-3} for the fabricated n-type 4H-SiC epitaxial detectors.

The activation energy corresponding to peak #4 was found to be located at 1.06 eV below the conduction band edge. The closest match with the Peak #4 were observed at a defect level located at E_c-1.03 eV which was designated as EH_5 [114] and at a defect level located at E_c-1.07 eV) in 2.5 MeV electron irradiated 4H-SiC [115]. EH_5 defect has been found in ion irradiated 4H-SiC and has been attributed to a carbon cluster [111]. The concentration of the EH_5 defects was found to be 2.2×10^{13} cm^{-3} for the fabricated n-type 4H-SiC epitaxial detectors.

The activation energy of Peak #5 was found to be 1.32 eV. A similar defect was reported and assigned to be defect center Ci1 in a chlorine implanted n-type 4H-SiC epitaxial layer [114]. The Peak #6 was found to have the highest activation energy (2.42 eV) among all the defect centers observed in the DLTS scans and remains unidentified as the corresponding activation energy does not match with any known defect level in 4H SiC that has been reported in the literature.

The trap concentrations corresponding to Peak #1 - #4 were all of the order of 10^{13} cm^{-3} with the Ti impurity (cubic Si site) being the maximum. Peak #5 and #6 were found to be one order of magnitude less in concentration. Prior investigations with 4H-SiC epitaxial layer detectors showed that $Z_{1/2}$ and EH_5 deep-lying defects have major impact in detector performance in terms of leakage current and energy resolution.

4.6 SPECTROSCOPY MEASUREMENTS

The defect characterization along with electrical characterization of the fabricated n-type 4H-SiC epitaxial layer detector provided useful information and a quality control tool in selecting detectors that would be suitable for spectroscopic characterization. Spectroscopic characterization using 0.1 μCi ^{241} Am alpha sources is discussed next.

4.6.1 Pulse Height measurements with ^{241}Am Alpha source

When alpha particles interact with a semiconductor, if the transferred kinetic energy exceeds the electron’s binding energy, ionization occurs and an electron-hole pair is generated which give rise to an electrical signal as generated charge carriers get collected at the respective electrodes under an applied bias. This electrical signal is then read out by the front-end electronics to provide pulse height spectra (PHS) for the incident radiation. Front-end electronics (Figure 2.23) consist of preamplifiers which converts charge signal to a voltage signal, shaping amplifier which filters noise, and multi-channel analyzers (MCA) which converts analog signals into digital information as pulse height spectrum.

The analog radiation detection experiments are conducted using a 0.1 μCi ^{241}Am source which provides low-energy gamma-rays at 59.6 keV or alpha particles at 5.486 MeV. The source and the detector were placed inside an EMI shielded aluminum box which was constantly evacuated using a rotary pump in order to minimize scattering of alpha particle with air molecules. The source used was a broad window (2 mm) source kept at a distance of 1.5 cm from the detector window ensuring that the whole surface of the detector was illuminated. The detector signals were collected using a Cremat CR110 charge sensitive pre-amplifier. The charge pulses were shaped using an Ortec 572 spectroscopy amplifier. The amplified signals were then digitized and binned to obtain pulse-height spectra using a Canberra Multiport II ADC-MCA unit controlled by Genie 2000 interface software. The peaks obtained in various spectra were fitted using peak analyzer function of Origin 8.6. The full width at half maxima (FWHM) of the alpha peak was calculated and the energy resolution of the detector was then determined using Equation 3.17 in Section 3.7.

Figure 4.14 shows a pulse height spectrum obtained using a ^{241}Am alpha source at zero applied bias (V_a + 1.44 V = 0 V). A symmetric and robust peak was obtained which indicates a substantial amount of diffusion of minority carriers. At zero applied bias, because of the negligible width of the depletion region, all the interactions predominantly take place in the neutral region (beyond the depletion region) as the range of 5.48 MeV alpha particles in SiC is ~ 18 μm. So, the charge transfer is dominated by the diffusion of holes. Figure 4.15 shows the alpha pulse height spectrum of the same detector obtained at 100 V applied bias. The percentage resolution was calculated to be 2.7 % (FWHM). Due to good Schottky behavior and low leakage current at high reverse bias voltage (~ 0.15 nA at 100 V as determined in Section 4.4.1), the fabricated detector was found to have high energy resolution.

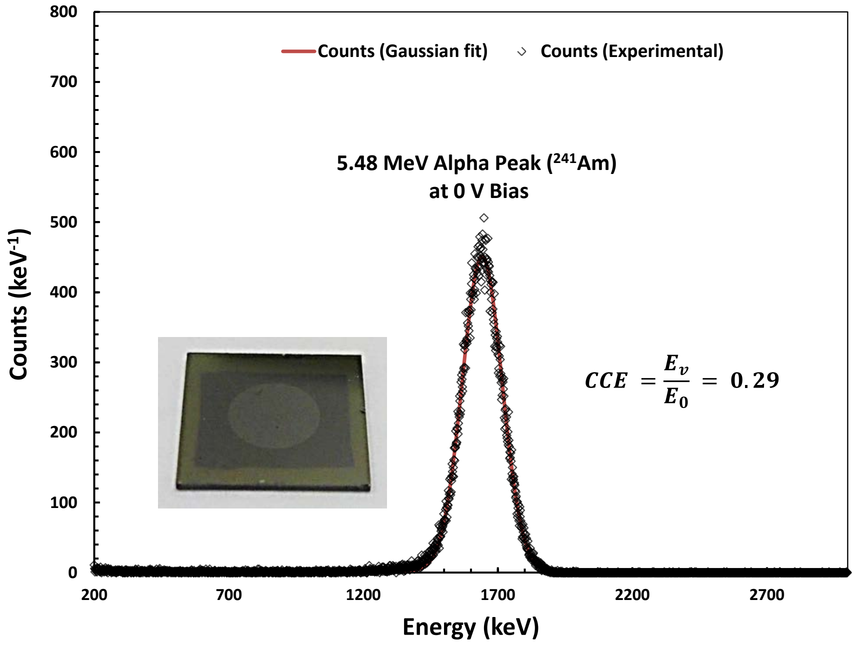

Figure 4.14. Pulse height spectra of ^{241}Am (5.48 MeV) for n-type 4H-SiC epitaxial Schottky detector biased at 0V. At this bias since depletion region width is negligible, all interactions predominantly take place beyond the depletion region and the charge transfer is dominated by the diffusion of minority carriers (holes).

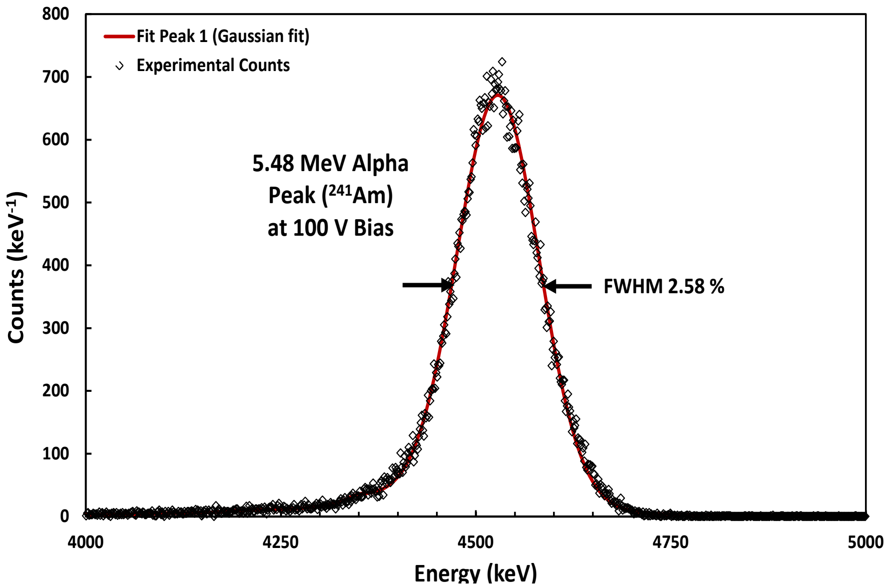

Figure 4.15. Pulse height spectra for 5.48 MeV alpha particles obtained using the same n-type 4H-SiC Schottky detector at an operating voltage of 100 V. The resolution of the peak was determined to be 2.58% (FWHM).

4.6.2 Charge Collection Efficiency with ^{241}Am Alpha source

Performance resolution of a nuclear doctor is a function of collected charge carriers generated by alpha particles traversing through the detector materials. Critical assessment of detector performance when irradiated with nuclear radiation can be performed by evaluating charge collection efficiency (CCE). The charge carrier collection efficiency could be measured using drift-diffusion model as described in the following equation [116].

$$\begin{aligned} CCE_{theory} &= CCE_{drift} + CCE_{diffusion} \\ &= \frac{1}{E_p}\int_0^d \left(\frac{dE}{dx}\right) dx + \frac{1}{E_p}\int_d^{x_r} \left[\left(\frac{dE}{dx}\right) \times \exp\left\{-\frac{x-d}{L_d}\right\}\right] dx \end{aligned} \qquad 4.13$$

where E_p is the energy of the alpha particles, d is the depletion width at the particular bias, $\frac{dE}{dx}$ is the electronic stopping power of the alpha particles calculated using SRIM 2012 [117], x_r is the projected range of the alpha particles with energy E_p, and L_d is the diffusion length of the minority carriers. The model (Equation 4.13) separately determine the contribution of charge carriers generated within the depletion region that drifted to collecting electrode, CCE_{drift}, and the contribution of carriers generated in the neutral region (beyond depletion region) and diffused to the depletion region, $CCE_{diffusion}$,. The overall charge collection efficiency is the sum of these two.

Charge collection efficiencies were measured using the same alpha particle source at different reverse bias voltages. Experimentally, CCE is calculated as the ratio of energy deposited in the detector (E_v) to the actual energy of the alpha particles

(5.48 MeV) emitted by the source (E_0); $CCE = E_v/E_0$. The energy deposited was calculated from the alpha peak position in a calibrated MCA. The charge collection efficiency at zero applied bias (Figure 4.14) was calculated to be 29 %. Such a high value of CCE at zero applied bias implies that the diffusion length of the holes is comparable to the range of the alpha particles. Literature search indicated that even a higher CCE of 50 % at 0 V was reported for 26 μm thick n-type 4H-SiC epilayer detectors for 5.39 MeV alpha particles [115]. The hole diffusion length in their case was reported as 13.2 μm.

Figure 4.16 shows the variation of CCE calculated using 5.48 MeV alpha particles as a function of reverse bias voltage. The CCE (total CCE obtained experimentally) was seen to saturate after an applied reverse voltage of 180 V. The highest CCE achieved was ~90 %. Alpha particles of 5.48 MeV energy have a projected range of 18 μm in SiC. The depletion width in the fabricated detector was calculated to be 16 μm at a reverse bias of 250 V. So the alpha particles did not deposit their full energy within the depletion region which is the active region of the detector. This is believed to be the reason behind not achieving 100 % charge collection efficiency.

To have a better perspective of the variation of CCE with applied bias, drift-diffusion model (Equation 4.13) was used to separately calculate the charge collection efficiency due to drifts of charge carriers in the depletion region and due to diffusion of holes in the neutral region. It can be seen from Figure 4.16 that initially (up to 5 V), the $CCE_{diffusion}$ values were higher than $CCE_{depletion}$ values, which implies that at lower biases the charge transport was dominated by hole diffusion. On the other hand, it can be seen that at higher biases the $CCE_{depletion}$ values almost matches the experimentally obtained CCE values which implies that the charge transfer is almost solely due to carrier drift inside the depletion region.

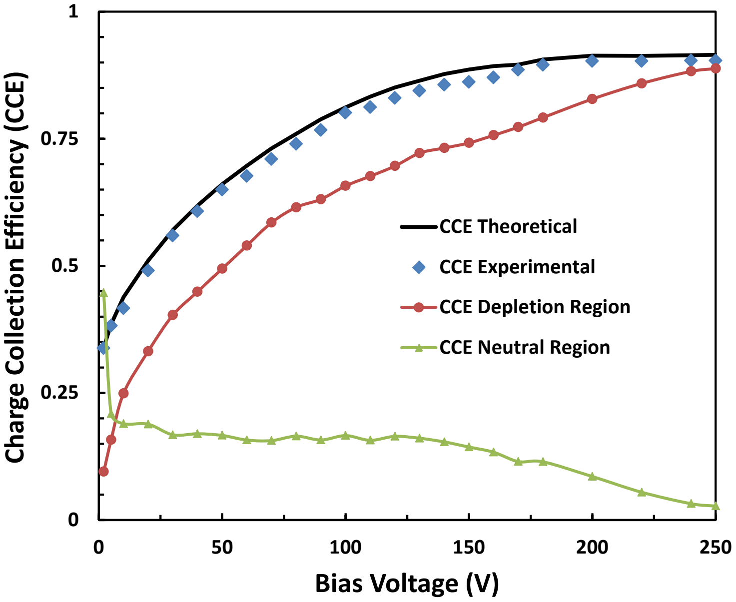

Figure 4.16. Variation of experimentally obtained (♦) and theoretically calculated (solid black line) charge collection efficiency as a function of reverse bias voltage. The theoretically calculated separate contributions to the total CCE from charge drifts in depletion region (●) and from hole diffusion in neutral region (▲) are also shown.

Apart from the CCE, the energy resolution was also monitored as a function of bias voltage. Figure 4.17 shows the variation of detector resolution measured in terms of FWHM as well as percentage resolution, for 5.48 MeV peak, as a function of reverse bias voltage. In order to monitor any variation in the post-detector electronics, pulser spectra were simultaneously recorded during all the data acquisitions using a precision pulser. The pulser-peak FWHM essentially gives the magnitude of noise of the detection system. The much higher FWHM values of alpha peak compared to that of the pulser peak clearly indicates that the detector resolution was not limited by the overall electronic noise of the system. It can be seen from the figure that initially the resolution improved (the lower the value the better the resolution is) with increase in bias voltage, attained a minima at 100 V and then started increasing with increasing bias. Figure 4.15 shows a resolution of 2.7% for the alpha pulse height spectrum was obtained at 100 V.

The initial decrease in the FWHM value is a normal detector behavior and is generally attributed to the increase in the active volume of the detector and reduction in detector capacitance with increase in bias. The reason behind the increase in the FWHM values beyond 100 V was not very apparent. No variation in the pulser-peak FWHM was observed in this region. Thus the effect of increasing leakage current on the detector resolution with applied bias can be ruled out as increase in detector leakage current means increase in parallel noise which would broaden the pulser peak as well. A plausible reason behind the deterioration of resolution with increasing bias could be explained as follows. As the reverse bias increases, the depletion region extends more towards the epilayer-substrate interface. So, the probability of finding threading type dislocation defects increases more and more. Threading dislocations (TDs) are basically dislocations which propagate from the substrate to the epilayer reducing the energy resolution. Inclusion of more and more TDs into the detector active volume due to the increase in depletion width with increase in reverse bias was considered to be a possible reason for the observed higher FWHM values at higher reverse bias voltages.

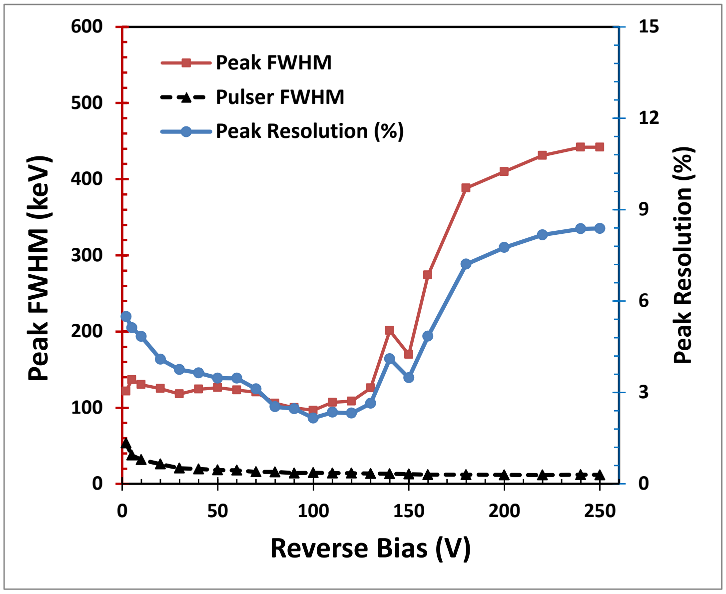

Figure 4.17. Variation of 5.48 MeV alpha peak FWHM (■), pulser peak FWHM (▲) and alpha peak percentage resolution (●) as a function of detector bias voltage.

4.7 CONCLUSION

In conclusion, in this study Schottky barrier detectors in planar configuration have been fabricated on 50 μm n-type 4H-SiC epitaxial layers grown on 360 μm SiC substrates by depositing ~10 nm nickel contact. Current-voltage (I-V), capacitance-voltage (C-V), and alpha ray spectroscopic measurements were carried out to investigate and evaluate the Schottky barrier detector properties. The room temperature I-V measurements revealed a very low leakage current of ~ 0.78 nA at 250 V reverse bias. The barrier height for Ni/4H-SiC Schottky contact was found to be ~1.4 eV by forward I-V measurement and ~1.5 eV by C-V measurements. The diode ideality factor was measured to be of 1.4, which is slightly higher the unity showing the presence of deep levels as traps and recombination centers. Capacitance mode deep level transient spectroscopy (DLTS) revealed the presence of the deep levels along with two shallow level defects related to titanium impurities (Ti(h) and Ti(c)) and an unidentified deep electron trap located at 2.42 eV below the conduction band minimum which is being reported for the first time. The concentration of the lifetime killer $Z_{1/2}$ defects was found to be 1.6× 10^{13} cm^{-3}. The detectors' performances were evaluated for alpha particle detection using a ^{241}Am alpha source. An energy resolution of ~ 2.5 % was obtained with a reverse bias of 100 V for 5.48 MeV alpha particles. The measured charge collection efficiency (CCE) was seen to vary as a function of bias voltage. With increased reverse bias, the detector active volume increases with the increase in depletion layer width accommodating more number threading type dislocations at the epilayer/substrate interface resulting in higher FWHM values as observed experimentally.

CHAPTER 5: CONCLUSION AND FUTURE WORK

5.1 CONCLUSION

Radioactive materials, as it decays, generate different high-frequency electromagnetic radiation such as alpha particles, beta, x-ray, gamma-ray and neutrons. Nuclear detectors could stop these high-energy ionizing radiations, collect and transport the charges generated to an external circuit, and produce an electrical signal which is amplified by readout electronics to measure the energy of nuclear interaction. Thus, nuclear detectors are important tools for accounting of radioactive materials and have widespread applications in nuclear power plants, nuclear waste management, in national security, in medical imaging such as x-ray, mammography, CT scan, and in high energy astronomy for NASA space exploration.

In this dissertation three different types of wide bandgap (WBG) radiation detectors were studied: (1) amorphous selenium (a-Se), (2) cadmium zinc telluride (CZT), and (3) silicon carbide (SiC). All three semiconductors have attractive electrical properties such as wide bandgap (≥ 1.5 eV) facilitating room temperature operation, high resistivity ($\geq 10^{10}$ Ω-cm) contributing to low thermal noise for high-resolution, and high charge carrier mobility-lifetime product offering high charge collection efficiency.

However, these semiconductors have distinct characteristics that set them apart from one another. For example, high Z (atomic numbers of constituent elements, Cd=48, Zn=30, Te=52) and high density of CZT offering high stopping power to absorb high energy x-rays and gamma-rays so CZT could be used for high energy x- and gamma ray spectrometer at room temperature. On the other hand, SiC has low Z value (Si=14, C=6) appropriate for detection of alpha particles and low energy x-ray (<10 keV) regime. Furthermore, high bandgap energy (~3.27 eV at 300 K) of 4H-SiC allows detector operation well above room temperature (~773 K) as required for nuclear fuel processing environment in nuclear power plants. Amorphous Se alloy with enriched boron (^{10}B) has high thermal neutron cross-section (3840 barns) due to boron and high radiation tolerance due to its amorphous structure, making it a favorable candidate for solid-state neutron detectors.

In this study, semiconductors were grown from in-house zone-refined ultra-pure precursor materials using specialized growth furnaces, which were modified, re-coded and optimized to obtain high quality detector materials. Experiments were carried out to optimize elemental composition of these compound semiconductors. Different metal-semiconductor contacts with metals of various work functions and metal-semiconductor-metal (MSM) devices with planar, pixilated, guard-ring and large area thin-film structures have been studied to ensure good charge transport properties and opto-electronic device performances. A series of characterization were carried out including scanning electron microscopy (SEM), x-ray diffraction (XRD), glow discharge mass spectroscopy (GDMS), optical absorption study, thermally stimulated current (TSC), deep-level transient spectroscopy (DLTS), and current-voltage (I-V) measurements. These extensive characterizations provided information on stoichiometry, morphology, purity, bandgap energy, resistivity, leakage current and presence of any performance-limiting electrical defect. Finally, to determine detection specificity, sensitivity and energy resolution, fabricated detector devices were evaluated with radiation sources, such as ^{241}Am (5.5 MeV) for alpha, ^{137}Cs (662 keV) for gamma, and ^{252}Cf for neutron source.

High quality boron (^{10}B) doped a-Se (As, Cl) alloy was synthesized in a specially designed alloying reactor. Alloy films were deposited using thermal evaporation, a low-cost technique which can be scaled up for larger detector production. The films used for detector fabrication had smooth, defect-free amorphous structure as determined by SEM and XRD. The bandgap and resistivity of ^{10}B-doped a-Se (As, Cl) alloy was determined to be 2.21 eV and $\geq 10^{12}$ Ω-cm, respectively, at 300 K. Single layer planer MSM (4″ × 4″ and 300 micron thick) detectors were fabricated on ITO glass and oxidized aluminum substrates. Current-voltage (I-V) characteristics showed very low leakage (~-10 nA at -1000 V); by using Al_2O_3 as blocking layer, leakage current was reduced to pA to a fraction of nA at -1000 V. Nuclear testing with high energy alpha particles (^{241}Am) and neutron (^{252}Cf) sources showed specific signature of thermal neutron detection. The data confirms that ^{10}B-doped a-Se (As, Cl) alloy films can be used to construct high performance compact neutron detectors.

The CZT crystals were grown at a stoichiometry of $Cd_{0.9}Zn_{0.1}Te$ from zone refined ultra-pure precursor materials with 50% excess Te using modified multi-pass vertical furnace. The bandgap energy was determined to be 1.56 eV. The electrical resistivity was estimated to be 6×10^{10} Ω-cm, which is high enough to fabricate a functional CZT radiation detector. The CZT detectors showed very low leakage current at a high bias (below 5 nA at – 1000V) due to their high resistivity, which are beneficial for high resolution detectors. The drift mobility and mobility-lifetime product of electrons were estimated to be 1186 cm^2/V.s and 5.9×10^{-3} cm^2/V, respectively. An energy resolution of 6.2% was obtained for CZT planar detector when irradiated with 60 keV low-energy gamma radiations (^{241}Am). The peaks were sharper and better resolution was observed for the CZT detector with guard ring geometry. An energy radiation of 2.6% was observed for detector with guard-ring structure irradiated with high energy 662 keV gamma radiations using ^{137}Cs source.

Schottky barrier detectors in planar configuration have been fabricated on 50 μm n-type 4H-SiC epitaxial layers grown on 360 μm SiC substrates by depositing ~10 nm nickel contact. Current-voltage (I-V), capacitance-voltage (C-V), and alpha ray spectroscopic measurements were carried out to evaluate the Schottky barrier detector properties. Room temperature I-V measurement revealed a very low leakage current of ~ 0.78 nA at 250 V reverse bias. The barrier height for Ni/4H-SiC Schottky contact was found to be ~1.4 eV and the diode ideality factor was measured to be 1.4, which is slightly higher than unity showing the presence of deep levels as traps and recombination centers. Capacitance mode deep level transient spectroscopy (DLTS) revealed the presence of the deep levels along with two shallow level defects related to titanium impurities (Ti(h) and Ti(c)) and an unidentified deep electron trap located at 2.42 eV below the conduction band minimum which is being reported for the first time. The concentration of the lifetime killer $Z_{1/2}$ defects was found to be 1.6×10^{13} cm^{-3}. The detectors' performances were evaluated for alpha particle detection using a ^{241}Am alpha source. An energy resolution of ~ 2.58 % was obtained with a reverse bias of 100 V for 5.48 MeV alpha particles. The measured charge collection efficiency (CCE) was seen to vary as a function of bias voltage. With increased reverse bias, the detector active volume increases with the increase in depletion layer width accommodating more number threading type dislocations at the epilayer/substrate interface resulting in higher FWHM values as observed experimentally.

5.2 FUTURE WORK

5.2.1 Recommended for Amorphous Selenium Detectors

Future recommended work for a-Se detectors:

- We have investigated enriched boron (B-10) doped a-Se detectors for thermal neutron detection. It has been learnt that better performance may be achieved with ^{6}Li doped a-Se alloy detector and the reasons for the better performance with ^{6}Li devices are multiple, including: (1) ^{6}Li reaction products have longer ranges (tritium - 32 μm, ^{4}He - 7 μm) than ^{10}B reaction products (α - 4.2 μm, ^{7}Li - 2.1 μm); ^{6}Li as factor of ~4 lower thermal neutron cross section, but ~7 times longer range of the reaction products in Se. In principle it could outperform ^{10}B provided similar concentrations can be achieved and depletion region for ^{10}B case cannot be extended to benefit from full detection of the reaction products. (2) The energies for ^{6}Li reaction products are much higher than that of ^{10}B, thereby, allowing for easier discrimination of background radiations. So, it would interesting to investigate ^{6}Li-doped a-Se (As, Cl) bulk alloy detectors for thermal neutron detectors in our future studies. We'll plan to carry out comparative study with two dopants (Li and B) with similar concentrations and select the best performing detector for further development.
- Different contact structures were studied to reduce the leakage current of a-Se devices by controlling carrier transport inside the devices for better detection signals. We have used Al/Al_2O_3 layers as an electron blocking layer in the

device. The high resistivity of ~10^{12} Ω-cm was observed with Al/Al_2O_3 electron blocking layers and the detectors showed a higher signal to noise ratio by comparing counts between no source and with ^{241}Am source. We haven't tested an impact on the leakage current and the energy resolution of a hole-blocking layer such as Sb_2S_3/Au layer and we'll test and evaluate a-Se detectors with and without this hole blocking layer.

- We have standardized deep level transient spectroscopy (DLTS) measurements on 4H-SiC alpha, low energy x-ray, and gamma-ray detectors. This DLTS measurements in capacitance (C-DLTS) and current mode (I-DLTS) will be highly useful to evaluate, characterize, and to optimize the performance of the fabricated a-Se detectors. Some of the fabricated a-Se detectors showed structural defects and induced crystallization (resulting to low resistivity) at the interface and within the bulk. This was mainly due to the strain induced during the slow deposition and cooling of the deposited a-Se films and non-uniform temperature distribution. These shallow and deep lying defects due to inclusions/precipitates, imperfections, point defects, and localized polycrystallinity (grain boundaries) will be evaluated through DLTS measurements.

5.2.2 Recommended for CZT Detectors

Future recommended work for CZT detectors:

- Future efforts on CZT detectors will be concentrated to increase production yield of large volume larger diameter detector grade CZT crystal ingots with increased resistivity and enhanced charge transport properties such as $\mu\tau$ products specifically $\mu\tau_e$ for single charge carrier devices of Frisch grid detectors.

- In CZT the electron mobility is much higher the hole mobility, so a polarization effect is much more pronounced even at a high bias voltage. In order to compensate for poor hole transport properties, specialized detector geometries, such as a co planar, multiple small pixel, and Frisch grid detector structure, can be applied to CZT. For this dissertation, only the planar and guard-ring detector structures were studied. For future effort it would be interesting to study multiple pixel, co-planar or Frisch grid detector structures and compare performance evaluation to the planar detector in order to achieve highest efficiency gamma ray detectors.
- Deep-level transient spectroscopy (DLTS) can be applied to the solvent-grown CZT crystals for further defect analysis. DLTS is a very sensitive technique for determining defects present in the space-charge region of a semiconductor material using voltage pulses. By using this spectroscopy technique, further information about the deep-level defects can be determined, which may assist future endeavors in reducing defects in the solvent-grown CZT crystals.

5.2.3 Recommended for SiC Detectors

Future recommended work for SiC detectors:

- A future research will be undertaken to focus on electronic noise analysis of the front-end readout electronics in terms of equivalent noise charge (ENC) to study the effect of various noise components that contribute to the total electronic noise in the detector and the detection system. We will carry out research on lowering detector capacitance without reducing the detector active area by increasing the detector active thickness, i.e. by using a thicker epitaxial layer. An electronic noise analysis of the detection system will reveal the possibility of achieving better energy resolution by lowering the detector capacitance. This will reveal the white series noise due to the total input capacitance which may have substantial effect on detector performance.

- The development of passivation and edge termination by depositing thin SiO_2 and Si_3N_4 films on 4H-SiC epilayer will be highly interesting for improving radiation detector's performance. In our preliminary studies we have shown that the edge termination method is very effective for improving the detectors' leakage current resulting the energy resolutions compared with that of a conventional detector fabricated from the same parent wafer. This work will be carried out in our future research. We will also continue to investigate radiation detection performance in terms of alpha spectroscopy measurements prior and subsequent to SiO_2 and Si_3N_4 passivation and edge termination. Continuation of our studies on deep level transient spectroscopy (DLTS) will reveal changes in life-time killing deep level defects of detectors with and without passivation and edge termination which could be correlated to the observed changes in radiation detection performance.
- To observe the impact of deep lying point and/or extended defects in the active region (in the width of the depletion region), Schottky barrier radiation detectors will be fabricated on <20 μm thick 4H-SiC epilayers and will be evaluated for radiation detection performance. The energy resolution for 5.486 MeV alpha particles will be measured with charge collection efficiency. We'll also investigate the nature and type of crystallographic defects through defect delineating KOH etching and the results will be analyzed and correlated.

REFERENCES

[1] B. Milbrath, A. Peurrung, M. Bliss, and W. Weber, "Radiation detector materials: An overview," *Journal of Materials Research*, vol. 23, pp. 2561-2581, 2008.

[2] A. Owens and A. Peacock, "Compound semiconductor radiation detectors," *Nuclear Instruments and Methods in Physics Research A*, vol. 531, pp. 18-37, 2004.

[3] G. F. Knoll, Radiation Detection and Measurement, 3rd ed., New York: John Wiley & Sons, Inc., 2000.

[4] P. N. Luke, R. H. Pehl, and F. A. Dilmanian, IEEE *Trans. Nucl. Sci.*, vol. 41, pp. 976-978, 1994.

[5] S. E. Pfanstiel, K. J. Hofstetter, T. A. DeVol, J. Radioanal. Nucl. Chem., vol. 223, pp. 89-98, 1997.

[6] W.R. Willing, Nuclear Instruments and Methods , vol. 96, pp. 615-?, 1971.

[7] K. Hukk etal., IEEE Trans. Nucl. Sci.,, vol. 30, pp. 402-?, 1983.

[8] S. D. Sordo, L. Abbene, E. Caroli, A. M. Mancini, A. Zappetteni, and P. Ubertini, "Progress in the Development of CdTe and CdZnTe Semiconductor Radiation Detectors for Astrophysical and Medical Applications," *Sensors*, vol. 9, pp. 3491-3526, 2009.

[9] T. Schlesinger, J. Toney, H. Yoon, E. Lee, B. Brunett, L. Franks, and R. James, "Cadmium zinc telluride and its use as a nuclear radiation detector material," *Materials Sci. Eng.*, vol. 32, pp. 103-189, 2001.

[10] A. E. Bolotnikov, K. Ackley, G. S. Camarda, C. Chercher, Y. Cui, G. De Geronimo, J. Fried, D. Hodges, A. Hossain, W. Lee, G. Mahler, M. Maritato, M. Petryk, U. Roy, C. Salwen, E. Vernon, G. Yang, and R. B. James, “An array of virtual Frisch-grid CdZnTe detectors and a front-end application-specific integrated circuit for large-area position-sensitive gamma-ray cameras,” Rev. Sci. Instrum vol. 86, pp. 073114-1-5, 2015.

[11] S. O. Kasap, C. Haugen, M. Nesdoly and J. A. Rowlands, "Properties of a-Se for use in flat panel X-ray image detectors," *J. Non-Crystalline Solids*, vol. 1163, pp. 266-269, 2000.

[12] F. Nava, G. Bertuccio, A. Cavallini and E. Vittone, "Silicon carbide and its use as a radiation detector material," *Measurement Science and Technology*, vol. 19, pp. 102001-1-25, 2008.

[13] T. E. Schlesinger and R. B. James, Eds., Semiconductors for Room Temperature Nuclear Detector Applications, San Diego: Academic Press Inc., 1995.

[14] R. M. Krishna, S. K. Chaudhuri, K. J. Zavalla, and K. C. Mandal, "Characterization of $Cd_{0.9}Zn_{0.1}Te$ based virtual Frisch grid detectors for high energy gamma ray detection," *Nucl. Instrum. Methods Phys. Res. A,* vol. 701, pp. 208-213, 2013.

[15] R. M. Krishna, T. C. Hayes, P. G. Muzykov, and K. C. Mandal, "Low Temperature Crystal Growth and Characterization of $Cd_{0.9}Zn_{0.1}Te$ for Radiation Detection Applications," *MRS Proc.*, vol. 1341, pp. 39-44, 2011.

[16] M. Hoheisel and L. Batz, "Requirements on amorphous semiconductors for medical x-ray detectors," *J. Non-Crystalline Solids,* vol. 266-269, pp. 1152-1157, 2000.

[17] O. Bubon, G. DeCrescenzo, J. A. Rowlands, and A. Reznik, "Amorphous selenium (a-Se) avalanche photosensor with metal electrodes," *J.Non-Crystalline Solids,* vol. 358, p. 2431–2433, 2012.

[18] V. Radeka, N. A. Schaknowski, G. C. Smith and B. Yu, "High Performance Imaging Neutron Detectors," *Nucl. Instrum. Meth.,* vol. A419, pp. 642-647, 1998.

[19] S. Kasap, C. Haugen, M. Nesdoly and J. Rowlands, "Properties of a-Se for use in flat panel X-ray image detectors," *J. Non-Crystalline Solids*, vol. 1163, pp. 266-269, 2000.

[20] C. Oner, K. V. Nguyen, R. O. Pak, M. A. Mannan, and K. C. Mandal, “Investigation of thermally evaporated high resistive B-doped amorphous selenium alloy films and metal contact studies,” *SPIE Proc.*, vol. 9593, pp. 95931I-1-195931I-11, 2015.

[21] S. H. Majid and R. E. Johanson, "Studies on excess noise in stabilized amorphous selenium used in X-ray photodetectors," *J. Non-Crystalline Solids,* vol. 354, pp. 2763-2766, 2008.

[22] S. Abbaszadeh, N. Allec, S. Ghanbarzadeh, U. Shafique, and K. S. Karim, "Investigation of Hole-Blocking Contacts for High-Conversion-Gain Amorphous Selenium Detectors for X-Ray Imaging," *IEEE Trans. Electron Devices*, vol. 59, pp. 2403-?, 2012.

[23] C. Allen, G. Belev, R. Johanson, and S. Kasap, "Relaxation of the electrical properties of vacuum-deposited a-$Se_{1-x}As_x$ photoconductive films: Charge-carrier lifetimes and drift mobilities," *J. Vac. Sci. Technol. A*, vol. 28, p. 1145-1152, 2010.

[24] S. Kasap, K. Koughia, B. Fogal, G. Belev, and R. Johanson, "The influence of deposition conditions and alloying on the electronic properties of amorphous selenium," *Fizika i Tekhnika Poluprovodnikov,* vol. 37, pp. 816-821, 2003.

[25] A. R. Powell and L. B. Rowland, "SiC materials - Progress, status, and potential roadblocks," *Proceedings of the IEEE,* vol. 90, pp. 942-955, 2002.

[26] P. G. Neudeck and J. A. Powell, "Performance limiting micropipe defects in silicon carbide wafers," *IEEE Electron Devices Lett.,* vol. 15, pp. 63-65, 1994.

[27] S. V. Rendakova, I. P. Nikitina, A. S. Tregubova, and V. A. Dmitriev, "Micropipes and dislocation density reduction in 6H-SiC and 4H-SiC structure grown by liquid phase epitaxy," *J. Electron. Mater*., vol. 27, pp. 292-295, 1998.

[28] J. J. Sumakeris, J. R. Jenny, and A. R. Powell, "Bulk crystal growth, epitaxy, and defect reduction in silicon carbide materials for microwave and power devices," *MRS Bulletin*, vol. 30, , pp. 280-286, 2005.

[29] J. A. Rowlands and S. O. Kasap, "Amorphous semiconductors usher-in-digital x-ray imaging," *Phys. Today,* vol. 50, pp. 24-30, 1997.

[30] S. O. Kasap, in The Handbook of Imaging Materials, 2nd edition, ed. A. Diamond, Marcel Dekker, New York, 1998.

[31] S. O. Kasap, J. B. Frey, G. Belev, O. Tousignant, H. Mani, J. Greenspan, L. Laperriere, O. Bubon, A. Reznik, G. DeCrescenzo, K. S. Karim, and J. A. Rowlands, "Amorphous and polycrystalline photoconductors for direct conversion flat panel x-ray image sensors," *Sensors,* vol. 11, pp. 5112-?, 2011.

[32] S. O. Kasap, J. B. Frey, G. Belev, O. Tousignant, H. Mani, L. Laperriere, A. Reznik, and J. A. Rowlands, "Amorphous selenium and its alloys from early xeroradiography to high resolution X-ray image detectors and ultrasensitive imaging tubes," *phys. status solidi b,* vol. 246, pp. 1794-?, 2009.

[33] O. Tousignant, Y. Demers, L. Laperriere, and S. Marcovici, "A-Se flat panel detectors for medical applications," *Proc. SAS IEEE,* pp. 1-5, 2007.

[34] K. Tanaka and K. Shimakawa, *Amorphous Chalcogenide Semiconductors and Related Materials,* Springer, New York, 2011.

[35] M. Z. Kabir and S. –A. Imam, "Transient and steady-state dark current mechanisms in amorphous selenium avalanche radiation detectors," *Appl. Phys. Lett.*, vol. 102, pp. 153515, 2013.

[36] K. C. Mandal, A. Mehta, S. K. Chaudhuri, Y. Cui, M. Groza, and A. Burger, “Characterization of amorphous selenium alloy detectors for x-rays and high-energy nuclear radiation detection,” *SPIE Proc*. vol. 8852, pp. 88521O-1-88521O-7, 2013.

[37] W. R. Wilcox, Zone Refining, *Kirk-Othmer Encyclopedia of Chemical Technology,* John Wiley & Sons, 2001.

[38] *Zone Refining*, McGraw-Hill Science & Technology Encyclopedia, The McGraw-Hill Companies, Inc., 2005.

[39] C. Oner, K. V. Nguyen, R. O. Pak, M. A. Mannan, and K. C. Mandal, “Investigation of thermally evaporated high resistive B-doped amorphous selenium alloy films and metal contact studies,” *SPIE Proc*., vol. 9593, 95931I-1-195931I-11, 2015.

[40] B. Hafner, "Energy Dispersive Spectroscopy on the SEM: A Primer," Characterization Facility, University of Minnesota—Twin Cities,http://www.charfac.umn.edu/instruments/eds_on_sem_primer.pdf.

[41] A. K. Bandyopadhyay, "Pressure-induced phase transformations in amorphous selenium by x-ray diffraction and Raman spectroscopy," *Phys. Rev. B,* vol. 54, pp. 12049-??, 1996.

[42] N. Mott, *Electronic Processes in Non-crystalline Materials*, Oxford: Clarendon Press, 1979.

[43] S. M. Sze and K. K. Ng, "Metal-Semiconductor Contacts," in *Physics of Semiconductor devices*, Hoboken, New Jersey, John Wiley & Sons, Inc., 2007, pp. 134-190.

[44] R. Dahal, K. C Huang, J. Cliton, N. LiCausi, J.-Q. Lu, Y. Danon, I. Bhat, *Appl. Phys. Lett.*, vol. 100 pp. 243507-1-4, 2012.

[45] K. C. Mandal, S. H. Kang, M. Choi, A. Kargar, M. J. Harrison, D. S. McGregor, A. E. Bolotnikov, G. A. Carini, G. C. Camarda, and R. B. James, *IEEE Trans. Nucl. Sci*., vol. 54, pp. 802-806, 2007.

[46] K. C. Mandal, S. H. Kang, M. Choi, J. Bello, L. Zheng, H. Zhang, M. Groza, U. N. Roy, A. Burger, G. E. Jellison, D. E. Holcomb, G. W. Wright, J. A. Williams, *J. Electron. Mater*., vol. 35, pp. 1251-1256, 2006.

[47] S. D. Sordo, L. Abbene, E. Caroli, A. M. Mancini, A. Zappetteni, and P. Ubertini, "Progress in the Development of CdTe and CdZnTe Semiconductor Radiation Detectors for Astrophysical and Medical Applications," *Sensors*, vol. 9, pp. 3491-3526, 2009.

[48] R. O. Pak, K. V. Nguyen, C. Oner, T. Chowdhury, and K. C. Mandal, “Characterization of $Cd_{0.9}Zn_{0.1}Te$ Single Crystals for Radiation Detectors,” *IEEE Conf. Record*, R3A-39, 7 pages, 2015.

[49] R. O. Pak and K. C. Mandal, "Defect Levels in Nuclear Detector Grade $Cd_{0.9}Zn_{0.1}Te$ Crystals," *ECS J. Solid State Sci. Technol.*, vol. 5, pp. P3037-P3040, 2016.

[50] R. O. Pak, K. V. Nguyen, C. Oner, M. A. Mannan, and K. C. Mandal, “Defect characterization of $Cd_{0.9}Zn_{0.1}Te$ crystals using electron beam induced current (EBIC) imaging and thermally stimulated current (TSC) measurements,” *SPIE Proc*., vol. 9593, pp. 95931J-1-195931J-8, 2015.

[51] K. C. Mandal, R. M. Krishna, R. O. Pak, and M. A. Mannan, “Characterization of high-resistivity CdTe and $Cd_{0.9}Zn_{0.1}Te$ crystals grown by Bridgman method for radiation detector applications,” *SPIE Proc.*, vol. 9213, pp. 92131L-1-92131L-9, 2014.

[52] S. K. Chaudhuri, R. O. Pak, K. Nguyen, L. Matei, V. Buliga, M. Groza, A. Burger, and K. C. Mandal, “Large Area $Cd_{0.9}Zn_{0.1}Te$ Pixelated Detector: Fabrication and Characterization,” *IEEE Trans. Nucl. Sci.*, vol. 61, pp. 793-798, 2014.

[53] G. Dhanaraj, K. Byrappa, V. Prasad, and M. Dudley, Eds., *Springer Handbook of Crystal Growth*, New York: Springer, 2010.

[54] M. J. Harrison, A. P. Graebner, W. J. McNeil, and D. S. McGregor, "Carbon coating of fused silica ampoules," *J. Crystal Growth*, vol. 290, pp. 597-601, 2006.

[55] R. M. Krishna, T. C. Hayes, P. G. Muzykov, and K. C. Mandal, "Low Temperature Crystal Growth and Characterization of $Cd_{0.9}Zn_{0.1}Te$ for Radiation Detection Applications," *MRS Proc.*, vol. 1341, pp. 39-44, 2011.

[56] R. M. Krishna, “Crystal Growth, Characterization and Fabrication of CdZnTe-based Nuclear Detectors,” Ph.D. Dissertation, University of South Carolina, 2013.

[57] École Polytechnique de Montréal, Fact database," 2010. [Online]. Available: http://www.crct.polymtl.ca/fact/documentation/.

[58] U. Roy, A. Gueorguiev, S. Weiller, and J. Stein, "Growth of spectroscopic grade $Cd_{0.9}Zn_{0.1}Te$:In by THM technique," *J. Crystal Growth*, vol. 312, pp. 33-36, 2009.

[59] H. Chen, S. A. Awadalla, F. Harris, P. Lu, R. Redden, G. Bindley, A. Copete, J. Hong, J. Grindlay, M. Amman, J. S. Lee, P. Luke, I. Kuvvetli, and C. Budtz-Jorgensen, "Spectral Response of THM Grown CdZnTe Crystals," *IEEE Trans. Nucl. Sci.*, vol. 55, pp. 1567-1572, 2008.

[60] G. Cohen-Taguria, M. Levinshteina, A. Ruzinb, and I. Goldfarb, "Real-space identification of the CZT(1 1 0) surface atomic structure by scanning tunneling microscopy," *Surface Science*, vol. 602, pp. 712-723, 2008.

[61] A. Tanaka, Y. Masa, S. Seto, and T. Kawasaki, “Zinc and selenium co-doped CdTe substrates lattice matched to HgCdTe,” *J. Crystal Growth*, vol. 94, pp. 166-170, 1989

[62] A. Burger, H. Chen, K. Chattopadhyay, D. Shi, S. Morgan, W. Collins, and R. James, "Characterization of metal contacts on and surfaces of cadmium zinc telluride," *Nucl. Instrum. Meth. Phys. Res. A*, vol. 428, pp. 8-13, 1999.

[63] Z. -Q. Fang, B. Claflin, D. C. Look, L. Polenta, and W. C. Mitchel, "Thermally stimulated current spectroscopy of high-purity semi-insulating 4H-SiC substrates," *J.Electron. Mater.*, vol. 34, , pp. 336-340, 2005.

[64] M. Pavlovic, M. Jaksic, H. Zorc, and Z. Medunic, “Identification of deep trap levels from thermally stimulated current spectra of semi-insulating CdZnTe detector material,” *J. Appl. Phys.*, vol. 104, pp. 023525-1-6, 2008.

[65] K. C. Mandal, P. G. Muzykov, R. Krishna, T. Hayes, and T. S. Sudarshan, “Thermally stimulated current and high temperature resistivity measurements of 4H semi-insulating silicon carbide,” *Solid State Commun*., vol. 151, pp. 532-535, 2011.

[66] R. Gul, A. Bolotnikov, H. K. Kim, R. Rodriguez, K. Keeter, Z. Li, G. Gu, and R. B. James, “Point defects in CdZnTe crystals grown by different techniques,” *J. Electron. Mater.*, vol. 40, pp. 274-279, 2011.

[67] R. Guo, W. Jie, N. Wang, G. Zha, Y. Xu, T. Wang, and X. Fu, “Influence of deep level defects on carrier lifetime in CdZnTe:In,” *J. Appl. Phys.*, vol. 117, pp. 094502-1-5, 2015.

[68] R. Nan, W. Jie, G. Zha, B. Wang, and H. Yu, “Thermally stimulated current spectroscopy applied on defect characterization in semi-insulating $Cd_{0.9}Zn_{0.1}Te$,” *J. Cryst. Growth*, vol. 361, pp. 25-29, 2012.

[69] S.-H. Wei and S. B. Zhang, “Chemical trends of defect formation and doping limit in II-VI semiconductors: The case of CdTe,” *Phys. Rev. B*, vol. 66, pp. 155211-1-10, 2002.

[70] A. Zerrai, K. Cherkaoui, G. Marrakchi, G. Bremond, P. Fougeres, M. Hage-Ali, J. M. Koebel, and P. Siffert, “Influence of deep levels on CdZnTe nuclear detectors,” *J. Cryst. Growth*, vol. 197, pp. 646-649, 1999.

[71] R. Soundararajan, K. G. Lynn, S. Awadallah, C. Szeles, and S.-H. Wei, “Study of defect levels in CdTe using thermoelectric effect spectroscopy,” *J. Electron. Mater.*, vol. 35, pp. 1333-1340, 2006.

[72] M.-H. Du, H. Takenaka, and D. J. Singh, “Native defects and oxygen and hydrogen-related defect complexes in CdTe: Density functional calculations,” *J. Appl. Phys.*, vol. 104, pp. 093521-1-10, 2008.

[73] Castaldini, A. Cavallini, B. Fraboni, P. Fernandez, and J. Piqueras, “Deep energy levels in CdTe and CdZnTe” *J. Appl. Phys.*, vol. 83, pp. 2121-2126,1998.

[74] C. Donolato, "On the theory of SEM charge-collection imaging of localized defects in semiconductors," *Optik*, vol. 52, pp. 19-36, 1978.

[75] C. Parish, D. Batchelor, C. Progl, and P. Russell, "Tutorial: Electron Beam-Induced Current in the Scanning Electron Microscope," *Microscopy and Analysis*, pp. 11-13, 2007.

[76] Z. He, "Review of the Shockley–Ramo theorem and its application in semiconductor gamma-ray detectors," *Nucl. Instrum. Meth.Phys. Res., A*, vol. 463, pp. 250-267, 2001.

[77] J. C. Erickson, H. W. Yao, R. B. James, H. Hermon, and M. Greaves, "Time of Flight Experimental Studies of CdZnTe Radiation Detectors," *J. Electron. Mater.*, vol. 29, pp. 699-703, 2000.

[78] K. Hecht, "Zum Mechanismus des lichtelektrischen Prim¨arstroms in isolierenden Kristallen," *Z. Physik*, vol. 77, pp. 235-245, 1932.

[79] K. C. Mandal, R. M. Krishna, P. G. Muzykov, S. Das, and T. S. Sudarshan, “Characterization of Semi-Insulating 4H Silicon Carbide for Radiation Detectors,” *IEEE Trans. Nuclear Sci.*, vol. 58, pp. 1992-1999, 2011.

[80] K. C. Mandal, R. M. Krishna, P. G. Muzykov, and T. C. Hayes, “Fabrication and characterization of high barrier $Cd_{0.9}Zn_{0.1}Te$ Schottky Diodes for high resolution nuclear radiation detectors,” *IEEE Trans. Nuclear Sci.*, vol. 59, pp. 1504-1509, 2012.

[81] R. O. Pak and K. C. Mandal, "Defect Levels in Nuclear Detector Grade $Cd_{0.9}Zn_{0.1}Te$ Crystals," *ECS J. Solid State Sci., Technol.*, vol. 5, pp. P3037-P3040, 2016.

[82] F. H. Ruddy, J. G. Seidel, H. Chen, A. R. Dulloo, and S. Ryu, “High-resolution alpha-particle spectrometry using 4H silicon carbide semiconductor detectors,” *IEEE Trans. Nucl. Sci.*, vol. 53, pp. 1713-1718, 2006.

[83] F. H. Ruddy, A. R. Dulloo, J. G. Seidel, M. K. Das, S. Ryu, and A. K. Agarwal, “The fast neutron response of 4H silicon carbide radiation detectors,” *IEEE Trans. Nucl. Sci.*, vol. 53, pp. 1666-1670, 2006.

[84] K. C. Mandal, S. K. Chaudhuri, K. V. Nguyen, and M. A. Mannan “Correlation of Deep Levels with Detector Performance in 4H-SiC Epitaxial Schottky Barrier Alpha Detectors,” *IEEE Trans. Nucl. Sci.*, vol. 61, pp. 2338-2344, 2014.

[85] K. C. Mandal, P. G. Muzykov, S. K. Chaudhuri, and J. Russell Terry, “Low energy x-ray and γ-ray detectors fabricated on n-type 4H-SiC epitaxial layer,” *IEEE Trans. Nucl. Sci.*, vol. 60, pp. 2888-2893, 2013.

[86] M. Rogalla, K. Runge, and A. Söldner-Rembold, “Particle detectors based on semi-insulating silicon carbide,” *Nuclear Phys. B*, vol. 78, pp. 516-520, 1999.

[87] M. A. Mannan, K. V. Nguyen, R. O. Pak, C. Oner, and K C. Mandal, “Deep Levels in n-Type 4H-Silicon Carbide Epitaxial Layers Investigated by Deep Level Transient Spectroscopy and Isochronal Annealing Studies,” *IEEE Trans. Nucl. Sci.*, vol. 63, pp. 1083-1090, 2016.

[88] M. A. Mannan, K. V. Nguyen, R. O. Pak, C. Oner, and K. C. Mandal, “Surface passivation and isochronal annealing studies on n-type 4H-SiC epitaxial layer,” *SPIE Proc.*, vol. 9593, pp. 95931H-1-195931H-11, 2015.

[89] K. V. Nguyen and K. C. Mandal, “Ru-induced Deep Levels in Ru/4H-SiC Epilayer Schottky Diodes by Deep Level Transient Spectroscopy,” *ECS J. Solid State Sci. Technol.*, vol. 5, pp. P3078-P3081, 2016.

[90] P. Samanta and K. C. Mandal, “Simulation of temperature dependent dielectric breakdown in n^+-polySi/SiO_2/n-6H-SiC structures during Poole-Frenkel stress at positive gate bias,” *J. Appl. Phys.*, vol. 120, pp. 064505-1-10, 2016

[91] K. V. Nguyen, M. A. Mannan, and K. C. Mandal, “Improved n-type 4H-SiC Epitaxial Radiation Detectors by Edge Termination,” *IEEE Trans.Nucl. Sci.*, vol. 62, pp. 3199-3206, 2015.

[92] L. S. Ramsdell, "Studies on silicon carbide," *American Mineralogist*, vol. 32, pp. 64-82, 1947.

[93] T. Kinoshita, K. M. Itoh, J. Muto, M. Schadt, G. Pensl, and K. Takeda, "Calculation of the Anisotropy of the Hall Mobility in N-type 4H- and 6H-SiC," *Materials Sci. Forum,* vol. 264–268, pp. 295-298, 1998.

[94] W. J. Choyke, H. Matsunami, and G. Pensi, Silicon Carbide: A Review of Fundamental Questions and Applications to Current Device Technology, Berlin: Wiley-VCH, 1997.

[95] G. L. Harris, Properties of SiC, London: INSPEC, 1995.

[96] B. Ellis and T. S. Moss, "The Conduction bands in 6H and 15R silicon carbide, Hall effect and infrared Faraday rotation measurements," *Proc. Royal Soc. London*, London, 1967.

[97] G. A. Lomakina, "Silicon carbide Proceeding," in *3rd International Conference on Silicon Carbide*, Miami, 1973.

[98] S. Karmann, W. Suttrop, A. Schoner, M. Schadt, C. Haberstroh, F. Engeibrecht, R. Helbig, G. Penal, R. A. Stein, and S. Leibenzeder, "Chemical vapor deposition and characterization of undoped and nitrogen-doped single crystalline 6H-SiC," *J. Appl. Phys.*, vol. 72, pp. 5437-5442, 1992.

[99] R.T. Tung, “Electron transport at metal-semiconductor interfaces: general theory,” *Phys. Rev. B*, vol. 45, pp.13509-13523, 1992.

[100] P. G. Muzykov, R. M. Krishna, and K. C. Mandal," Temperature dependence of current conduction in semi-insulating 4H-SiC epitaxial layer," *Appl. Phys. Lett.*, vol. 100, pp. 032101-1-4, 2012.

[101] M. Jang, Y. Kim, J. Shin, S. Lee, “Characterization of erbium-silicided Schottky diode junction.” *IEEE Electron Devices Lett.*, vol. 26, pp.354-356, 2005.

[102] Ioffe Physical-Technical Institute, (2016, Aug. 12) "Band Structure and Carrier Concentration," *NSM Archive - Physical Properties of Semiconductors* [Online]. Available: http://www.ioffe.rssi.ru/SVA/NSM/Semicond/SiC/bandstr.html

[103] K. V. Nguyen, R. O. Pak, C. Oner, M. A. Mannan, and K. C. Mandal, “High-barrier Schottky contact on n-type 4H-SiC epitaxial layer and studies of defect levels by deep level transient spectroscopy (DLTS),” *SPIE Proc.*, vol. 9593, pp. 95930I-1-195930I-8, 2015.

[104] D. V. Lang, "Deep-level transient spectroscopy: A new method to characterize traps in semiconductors," *J. Appl. Phys.*, vol. 45, pp. 3023-3032, 1974.

[105] T. Dalibor and G. Pensl, “Electrical properties of the titanium acceptor in silicon carbide” *Phys. Rev. B*, vol. 55, pp. 13618-13624, 1997.

[106] L. Gelczuk, M. Da browska-Szata, M. Sochacki, and J. Szmidt, “Characterization of deep electron traps in 4H-SiC Junction Barrier Schottky rectifiers,” *Solid-State Electron.*, vol. 94, pp. 56-60, 2014.

[107] J. Zhang, L. Storasta, J. P. Bergman, N. T. Son, and E. Janzén, “Electrically active defects in n-type 4H–silicon carbide grown in a vertical hot-wall reactor,” *J. Appl. Phys*., vol. 93, pp 4708-4714, 2003.

[108] A. Castaldini, A. Cavallini, L. Polenta, F. Nava, C. Canali, and C. Lanzieri, “Deep levels in silicon carbide Schottky diodes.” *Appl. Surf. Sci*., vol. 187, pp. 248-252, 2002.

[109] L. Storasta, J. P. Bergman, E. Janzen, A. Henry, and J. Lu, J. “Deep levels created by low energy electron irradiation in 4H-SiC,” *J. Appl. Phys*., vol. 96, pp. 4909-4916, 2004.

[110] N. Iwamoto, B. C. Johnson, N. Hoshino, M. Ito, H. Tsuchida, K. Kojima, and T. Ohshima, “Defect-induced performance degradation of 4H-SiC Schottky barrier diode particle detectors,” *J. Appl. Phys*., vol. 113, pp. 143714-1-5, 2013.

[111] C. G. Hemmingson, N. T. Son, O. Kordina, J. P. Bergman, E. Janzen, J. L. Lindstrom, S. Savage, and N. Nordell, “Deep level defects in electron-irradiated 4H SiC epitaxial layers,” *J. Appl. Phys*., vol. 81, pp. 6155-6159, 1997.

[112] T. A. G. Eberlein, C. J. Fall, R. Jones, P. R. Briddon, and S. Öberg, “Alphabet luminescence lines in 4H−SiC,” *Phys. Rev. B*, vol. 65, pp. 184108-1-4, 2002.

[113] T. Kimoto, K. Danno, and J. Suda, “Lifetime-killing defects in 4H-SiC epilayers and lifetime control by low-energy electron irradiation,” *phys. status solidi B*, vol. 245, pp. 1327-1336, 2008.

[114] G. Alfieri and T. Kimoto, “Capacitance spectroscopy study of deep levels in Cl-implanted 4H-SiC,” *J. Appl. Phys*., vol. 112, pp. 63717-1-4, 2012.

[115] A. M. Ivanov, E. V. Kalinina, A. O. Konstantinova, G. A. Onushkin, N. B. Strokan, G. F. Kholuyanov, and A. Hallén, “High-resolution short range ion detectors based on 4H-SiC films ,” *Tech. Phys. Lett*., vol. 30, pp. 575-577, 2004.

[116] M. B. H. Breese, "A theory of ion beam induced charge collection," *J. Appl. Phys.*, vol. 74, pp. 3789-3799, 1993.

[117] J. F. Ziegler, J. Biersack and U. Littmark, *The Stopping and Range of Ions in Matter*, New York: Pergamon Press, 1985.